UNIVERSITY OF CALIFORNIA
RIVERSIDE

Estimating Pollutant Concentration Maps at Multiple Spatial and Temporal Scales for Exposure Studies

A Dissertation submitted in partial satisfaction
of the requirements for the degree of

Doctor of Philosophy

in

Mechanical Engineering

by

Si Tan

March 2015

Dissertation Committee:

Dr. Akula Venkatram, Chairperson
Dr. Marko Princevac
Dr. Heejung Jung

The Dissertation of Si Tan is approved:

_____

_____

_____

Committee Chairperson

University of California, Riverside

ACKNOWLEDGEMENTS

First and foremost, I would like to show my deepest gratitude to my advisor, Dr. Akula Venkatram, for his constant support and encouragement. I would not have come this far without his guidance and inspiration.

I would like to thank my committee members, Dr. Marko Princevac and Dr. Heejung Jung, for providing valuable feedback to my dissertation.

I am also grateful to my former colleagues, Dr. Wenjun Qian, Dr. Qiguo Jing, Dr. Sam Pournazeri and my current colleagues, Mr. Nico Schulte, Mr. Faraz Enayati Ahangar, and Mr. Morteza Amini. Without their help, I would not have accomplish this work.

I would also like to thank the California Energy Commission (CEC), the University California Transportation Center (UCTC), and the California Air Resources Board (CARB) for funding my research projects.

Last but not least, I would like to thank my parents for their encouragement, understanding, care, and love.

The text of this dissertation, in part, is a reprint of the material as it appears in Environmental Modelling and Software (2014) 52, 19-37.

DEDICATION

To my dearest mom and dad,

Chunyun Deng and Dunyong Tan

ABSTRACT OF THE DISSERTATION

Estimating Pollutant Concentration Maps at Multiple Spatial and Temporal Scales for Exposure Studies

by

Si Tan

Doctor of Philosophy, Graduate Program in Mechanical Engineering
University of California, Riverside, March 2015
Dr. Akula Venkatram, Chairperson

Chronic exposure to high concentrations of pollutants such as NO_2 and ultrafine particles is associated with negative health effects. Studies of exposure to these pollutants require estimates of concentrations at temporal and spatial scales relevant to exposure calculations. We have developed and applied methods to construct these concentration "maps" by using a combination of measurements and modeled results. To estimate concentration patterns at the urban scale of tens of kilometers we have formulated a Lagrangian model to estimate concentrations of NO_x, NO_2, and O_3 over a domain extending over hundreds of kilometers. The model is evaluated with data collected at 21 regional monitoring stations in the San Joaquin Valley Air Basin during 2005. The model provides adequate descriptions of the spatial and temporal variation of concentrations of NO_2, and NO_x. We then use "residual" Kriging to combine the results from the dispersion model with observed concentrations to produce realistic concentration maps.

To estimate concentration patterns at scales of tens of meters in urban areas we developed a dispersion model that accounts for the effects of local building morphology on dispersion. The data used to evaluate the model was collected in field studies conducted in Los Angeles, California. The studies measured ultrafine particle concentrations and associated micrometeorology at several locations with different building morphologies. Surface concentrations in urban areas are primarily controlled by vertical dispersion, which depends on the street aspect ratio, defined as the ratio of the equivalent building height to the street width, and the vertical turbulent velocity σ_w. The presence of buildings increases the concentrations due to local traffic emissions relative to open areas. Since routine measurements of micrometeorological variables are usually not available in urban areas, we have developed models that allow us to estimate urban surface variables using values measured at an upwind rural location. Results from the urban street scale dispersion model can be combined with measurements from urban monitors to generate concentration maps with spatial resolution of meters and time resolution of minutes.

TABLE OF CONTENTS

LIST OF FIGURES

LIST OF TABLES

1 MOTIVATION, OBJECTIVES, AND APPROACH

1.1 Problem Statement

Advances in technology have significantly improved our quality of life, but they have been accompanied by emissions of air pollutants such as nitrogen oxide and volatile hydrocarbons from motor vehicles, factories, and power plants. Although the implementation of air quality regulations and the resulting emission controls has reduced the air quality impact of these emissions, their ambient concentrations are still at high enough levels in several urban areas to raise health concerns. Furthermore, emissions of ultrafine particles (aerodynamic diameters less than 100 nm) from vehicles have been implicated in adverse health effects, such as respiratory and cardiovascular diseases, in people living close to roadways (Miller et al., 2007; Pope and Dockery, 2006). These health effects are primarily caused by chronic exposure to pollutants.

A crucial step in determining the link between health effects and air pollution is to accurately assess exposure (USEPA, 1992). Exposure assessment requires estimates of the relevant pollutant concentrations, the population exposed to these concentrations, and the frequency and duration of contact of the population with the pollutant. This requires estimating the spatial and temporal patterns of pollutant concentrations over the populated region of interest. This thesis focuses on this aspect of exposure, with emphasis on the application of dispersion models to construct

temporal and spatial distributions of concentrations.

1.2 Background

Early epidemiological studies (Dockery et al., 1993; Pope et al., 2002), focused on examining concentration differences across different cities, and exposure assessments were often made using concentration measurements made at central monitoring stations, which are sparse and cannot accurately represent spatial distributions of concentrations. Studies (Fischer et al., 2000; Jerrett et al., 2005; Lebret et al., 2000) have shown that there are large spatial variations of pollution levels within cities. Thus, high spatial resolution concentration maps are needed to more accurately assess exposure.

To estimate concentrations at sites where no monitoring data is available we can interpolate the observations at several monitoring sites. One of the most popular techniques for interpolating concentrations fields is a geostatistical technique called Kriging (Jerrett et al., 2005). The popularity of Kriging is related to the advantages it enjoys over other interpolation techniques. First, it interpolates observations using weights that do not depend upon data values. Therefore, these weights can be calculated once and applied to several sets of data. Second, Kriging provides an estimate of the interpolation error. The third advantage of Kriging is that it is an 'exact' interpolator, which means that the estimate at any observational point is the observation itself. Kriging assumes that a variable can be expressed as the sum of a

deterministic component (trend) and a fluctuating component. In general, the underlying trend is assumed to be constant, and the statistics of the stochastic component are taken to be invariant with location and direction (Venkatram, 1988). The assumption of constant underlying trend is clearly incorrect when applied to concentration fields, which vary both spatially and temporally in response to emissions and meteorology. I will show in this thesis that we can use a physically based model to estimate the trend in the data, which then justifies the assumption of isotropy and homogeneity of the residual between the trend and the observed concentration (Venkatram, 1988). Other methods such as Inverse Distance Weighting (*IDW*), which assumes the weights are functions of the separation distance only, and bi-cubic spline have also been applied to produce reasonable estimates at the un-sampled sites (Neupane et al., 2010), but both spline and *IDW* do not provide estimation errors.

Land Use Regression (*LUR*) models are statistical models that have gained popularity in estimating intra-urban concentration variability due to the increasing availability of geographic information and software that allows manipulation of large data sets (Hoek et al., 2008). A *LUR* model assumes that observed concentration is a linear combination of a set of predictor variables such as population density, land use, physical geography such as elevation and climate, and traffic related variables at the site at which the concentration is measured. This model is then fitted to the observed

concentrations using statistical techniques. The resulting statistical model is then used to estimate concentrations at locations where concentration measurements are not available.

The predictor variables in *LUR* models can also include meteorological indicators, such as wind speeds and wind directions (Hoek et al., 2008). *LUR* model was first implemented in the *Smaller Area Variations In Air quality and Health* (*SAVIAH*) study, which aims to identify indicators that can be used to assess the risk of respiratory diseases due to air pollution in children (Briggs et al., 1997). Numerous studies (Briggs et al., 1997; Kanaroglou et al., 2005; Ross et al., 2006; Smith et al., 2006, and etc) have demonstrated that *LUR* can adequately predict annual average concentrations of NO_x, NO_2, and particulate matter.

LUR models have several limitations. First, they are essentially empirical models that cannot be justifiably transferred from one site to another; recalibration is necessary due to different meteorology, topography, emissions, and background concentrations at different sites. Second, *LUR* models are not based on governing physical processes, which limits their application to studying components of the total concentrations that are related to specific sources; most *LUR* models are only designed to be applied to estimate total concentrations. Without the inclusion of physical processes, *LUR* models also cannot capture the large spatial and temporal variation of concentrations due to short-term variation of both meteorology and

emissions (Hoek et al., 2008). Wilton et al (2010) have developed a hybrid *LUR* model, where they incorporated the results from the dispersion model CALINE3 into *LUR* to account for the effect of varying meteorology and emissions. The output from the dispersion model CALINE3 is simply include as a predictor variable in the *LUR* model. The hybrid LUR showed improvements over the traditional *LUR* models, but its performance is still limited by the number of available observations that can be used to calibrate the model.

The third limitation of *LUR* models is that the impact of some priority pollutants cannot be separated, so that independent health effects of each pollutant cannot be verified. Last but not least, some of the predictors used in *LUR* models, such as population density, could introduce confounding; population density could be associated with socio-economic status, which could also introduce health risks to certain diseases (Hoek et al., 2008).

In this thesis, we show that dispersion models, in combination with statistical interpolation methods, can be used to overcome some of the shortcomings of purely empirical models. Dispersion models directly relate concentrations to emissions and meteorology through the mass conservation equation. Concentrations in urban areas are associated with emissions from a large number of sources, such as vehicles and power generators, distributed over the urban area. An approach that allows us to account for all the emission sources is to use separate dispersion models for different

spatial scales so that sources at different distances from the area of interest are treated with different levels of source aggregation. The concentration at a receptor has three main components: a regional contribution computed from a long-range transport model with grid spacing of the order of tens of kilometers (*regional scale*), an urban "background" contribution from sources aggregated over kilometer-sized grids (*urban scale*), and a local contribution from models that estimate concentrations at meters from a receptor (*local/street scale*). This approach was pioneered by Brandt et al. (2001a, 2001b, 2001c, 2001d, 2001e, 2003) in developing an integrated operational air pollution forecast system called *THOR*, which has three dispersion models (*DEOM*-the Danish Eularian Operational Model, *UBM*-Urban Background Model, and *OSPM*-Operational Street Pollution Model) built into it and is capable of estimating concentrations at scales ranging from the European scale to street scale.

Dispersion models incorporate the governing processes, and in principle, can provide better concentration estimates than *LUR* models. However, uncertainties in model formulation and model inputs are unavoidable in describing the complex system that governs air quality. Thus, there are always relatively large deviations between model estimates and corresponding observations. These discrepancies can be reduced by using semi-empirical models in which several of the processes are parameterized: they are represented by parameters whose values are adjusted to reduce the deviations between model estimates and observations. For example, the

complex processes that control deposition of pollutants to the ground are represented by a single deposition velocity. While such parameterizations obscure the underlying physics, they can provide us insightful information and are often used to develop useful dispersion models. Venkatram et al (1990) have applied a semi-empirical model to understand the observations of acid deposition. The parameter used to represent oxidant concentrations demonstrated the importance of oxidation limitation in wet deposition of sulfur; assuming a limitless supply of oxidant concentrations results in overestimation of the average observed sulfur concentrations in the rain. The need for oxidant limitation might have implications on the efficacy of sulfur emission controls on wet deposition (Venkatram et al., 1990). Another example of a semi-empirical model is the Simplified Ozone Modeling System. It uses a simplified chemical scheme, which simulates ozone photochemistry using only 7 'pseudo' reactions that are semi-empirically determined from chamber experiments (Azzi, 1992). The highly parameterized chemistry scheme significantly reduces the computational time while producing results that are comparable to the more complete Carbon Bond IV (*CB-IV*) chemistry scheme (Venkatram et al., 1994). This approach of using semi-empirical models is particularly useful in our application in which the primary objective is to construct high temporal and spatial resolution concentration maps that can be used for exposure studies.

As indicated earlier, the approach in this thesis is to develop and use dispersion

models to provide the information required to interpolate between observations. The type of model described here is semi-empirical, which has two features that blunt the criticism often directed at dispersion models (Jerrett et al., 2005): 1) it uses a small number of readily available model inputs, and 2) its structure allows fitting of model estimates to observations to reduce the uncertainty in model estimates.

The need for a dispersion model at urban street scales is especially important because *LUR* models have struggled with including variables that account for street canyon effects (Eeftens et al., 2013). This thesis describes the development of a model that accounts for the effects of building morphology in a physically realistic framework. Future research, which I have not conducted, will use the results from the model to construct concentration patterns within a neighborhood of streets.

1.3 Motivation and Objectives

My research is motivated by the need to improve methods to construct concentration maps at urban and street scales using dispersion models to fill in the gaps between observations. This objective was achieved through field studies and modeling at two scales:

I: Urban/Regional Scale

(1) Formulated and evaluated a semi-empirical dispersion model that can efficiently estimate concentrations at urban scales at high temporal and spatial resolution.

(2) *Applied a method to combine observations with dispersion models to construct concentration patterns over regions in Los Angeles and the San Joaquin Valley*

II: Street Scale

(1) *Conducted field studies to make measurements of concentrations of ultrafine particles and associated micrometeorology at several locations in Los Angeles*

(2) *Used the data from field studies to develop and evaluate a street scale dispersion model that is suitable for urban areas.*

(3) *Developed and evaluated models that estimate urban micrometeorology using more readily available upwind rural values*

1.4 Structure of the Dissertation

Chapter 2 describes methods to combine observations with dispersion models to construct concentration patterns at the urban scale, and a long-range transport model that can be used to estimate pollutant concentrations at urban/regional scale. Chapter 3 describes the field studies and the resulting model applicable to the street scale. Chapter 4 provides the major conclusions resulting from my research.

2 CONSTRUCTING CONCENTRATION MAPS AT URBAN/REGIONAL SCALE

2.1 Introduction

As mentioned in the introduction, accurate exposure assessment requires high temporal and spatial resolution concentration maps. Interpolation of observations does not capture the large variability of pollutant concentrations in between the monitoring sites due to the sparse monitoring network. Dispersion models are great candidates for estimating the 'in-between' concentrations since they can account for the high spatial and temporal variability of pollutant concentrations due to varying emission and micrometeorological conditions. Moreover, semi-empirical dispersion models are parameterized, so they can be easily adjusted to fit observations, and they often require very limit number of readily available inputs.

Due to uncertainties in model formulation and inputs such as emission and meteorology, model estimates will always deviate from observed concentrations; tuning the parameters might not be sufficient. We further reduce the discrepancies between model estimates and observations using Kriging interpolation, which will be discussed in more details in section 2.3. The resulting concentration maps generated by combing model estimates and observations will be discussed in section 2.4

To compute concentrations at the urban scale, studies have shown that comprehensive models such as *CMAQ* (*Community Multi-scale Air Quality Model*;

Byun and Schere, 2006)) could provide reasonable estimates. Constructing high spatial and temporal resolution concentration maps requires simulation of concentration at a very large number of grid points over a long period of time, so comprehensive models can become computationally cumbersome. Thus, it is important for the model to be computationally efficient. The simple Urban Background Model (*UBM*, Berkowicz, 2000) is typical of the modeling response to the need for urban scale dispersion models with small computational demands. *UBM* achieves computational efficiency through two simplifications: a straight-line steady dispersion model, and ozone chemistry based on photo-stationarity, which neglects the role of hydrocarbons. In the next section we will describe such a model. The required efficiency is achieved by separating transport and chemistry and using a highly parameterized chemistry scheme to replace the more complex models, such as Carbon Bond-IV.

2.2 The Lagrangian Background Model

We focus on a model that is intermediate between comprehensive photochemical models and the simple *UBM*. This model estimates urban "background" concentrations of NO_x, NO_2, and O_3, averaged over a scale of a few kilometers to tens of kilometers. The lower limit on the grid size is determined by the assumption that the concentration is well mixed through the depth of the mixed layer, and the upper limit depends on the validity of using surface winds to represent

transport in the atmosphere. The model treats unsteady meteorological conditions with trajectories that reflect space and time varying surface winds, and it reduces the computational requirements of photochemical models by separating transport and chemistry using a method described in Venkatram et al. (1998). The model is evaluated by comparing model estimates of relevant species with data from measurements made in the San Joaquin Valley *(SJVAB)* air basins in California,

2.2.1 Model Formulation

The model described here is similar to the Lagrangian model used in Europe to estimate long-range transport of sulfur (Eliassen and Saltbones, 1983). It estimates the concentration of a pollutant by tracing the history of the air parcel associated with the concentration at the receptor of concern at a specified time. Back trajectories are calculated in 1-hour time steps using the hourly averaged wind speed (at 10 m above the ground level), and wind direction from the meteorological station closest to the receptor using the following equations,

$$x_{i-1} = x_i - U_i \cos(270 - \theta_i) \quad \textbf{(2-1)}$$

$$y_{i-1} = y_i - U_i \sin(270 - \theta_i) \quad \textbf{(2-2)}$$

where x_i and y_i are the location of the air parcel, U_i is the wind speed, and θ_i is the wind direction at time step *i.* Each trajectory is extended backwards in time for 24 hours, which assumes that sources beyond this travel time make a negligible contribution to concentrations at the receptor. This assumption was evaluated using

sensitivity studies, which are described in section 2.2.4. A sample 24hr back-trajectory calculated for a site located in the *SJVAB* in central California, is shown in Figure 2-1. As shown, the air parcels mainly travel along the valley from northwest to southeast.

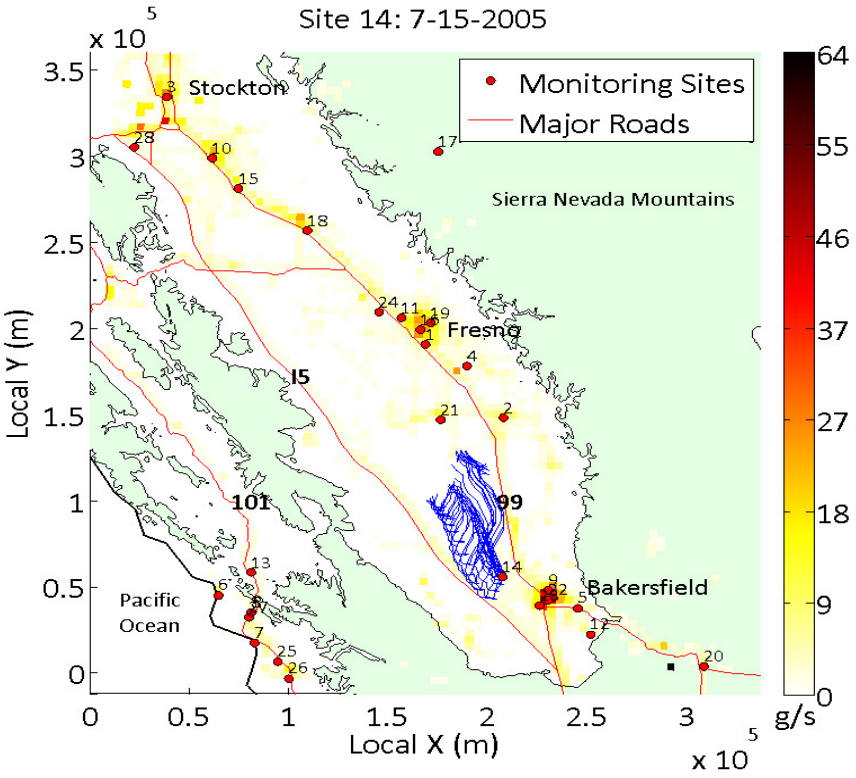

Figure 2-1: Sample calculated 24hr back-trajectory

To facilitate the use of the model, meteorological inputs are taken directly from the surface input files used by *AERMOD* (Cimorelli et al., 2005) which are generated by the *AERMOD* meteorological preprocessor (*AERMET*). In a single layer model, the choice of the height of the wind used to compute trajectories is arbitrary; the choice of the 10 m wind is justified a posteriori through comparison of model estimates with observations.

The air parcel has horizontal dimensions of the grid square used to represent emissions of NO_x and *VOC* (Volatile Organic Compounds) over the domain. The height of the air parcel corresponds to the local mixed layer height. In order to account for horizontal dispersion, we examined the approach used in *UBM* (Berkowicz, 2000), in which the concentration at a receptor is taken to be the average of the concentrations corresponding to slightly different wind directions ($\Delta\phi = 3° - 5°$) centered on the average wind direction. We found that perturbing the back trajectories using this approach made little difference to the results. Consequently, this approach was dropped to improve computational efficiency.

Emissions are injected every hour into the box at the grids traced by the back trajectory, and then mixed through the volume of the box (Figure 2-2).The concentrations are stepped from the $(i - 1)^{th}$ to the i^{th} time step through

$$C_i = C_{i-1} min\left(\frac{z_{i-1}}{z_i}, 1\right) + \frac{\Delta m_i}{z_i} \qquad \textbf{(2-3)}$$

where C_i is the concentration of the species at time i, Δm_i is the mass of pollutant injected into the air parcel, and z_i is the mixed layer height. The term within the parenthesis on the right hand side of the equation ensures that the concentration does not increase when the mixed layer decreases during a time step. The loss of mass when the mixed layer height decreases ensures that the near surface concentration is affected primarily by material that is less than 24 hours old. The mixed layer heights used in this model are generated through *AERMET*, which calculates the height of the

convective boundary layer (*CBL*) through a simple one-dimensional energy balance model (Carson, 1973). The height of the stable boundary layer (*SBL*) is based on the formulation described in Venkatram (1980).

Currently the model does not account for dry deposition, although this process can be readily incorporated into Equation (2-3). The mass of pollutant injected per unit surface area of the air parcel is $\Delta m_i = q_i(\vec{r},\tau)\Delta t$, where $q_i(\vec{r},\tau)$ is the emission density at the location of the parcel, $\vec{r}$, injected at a time from the initiation of the trajectory, τ , and Δt is the time step of the trajectory calculation.

The incremental concentration during the last hour of the air parcel's path is computed with a steady state dispersion model (Venkatram and Cimorelli, 2007) that accounts for incomplete vertical mixing,

$$\Delta C_i = \sqrt{\frac{2}{\pi}}\frac{q}{\sigma_w}\ln\left(1+\frac{\sigma_w \Delta t}{h}\right) \qquad \textbf{(2-4)}$$

where q is the emission rate per unit area, σ_w is the standard deviation of the vertical velocity fluctuations, and h is the initial vertical spread of surface emissions which is taken to be 1 m.

The equation is modified if the pollutant is well mixed through the boundary layer during the last time step before the parcel reaches the receptor.

$$\Delta C_i = \sqrt{\frac{2}{\pi}}\frac{q}{\sigma_w} ln\left(\sqrt{\frac{2}{\pi}}\frac{z_i}{h}\right) + \frac{q(R-R_m)}{U z_i} \qquad \textbf{(2-5)}$$

where U is the wind speed, R_m is the critical radius that determines whether the

pollutants are well mixed vertically within the box, and R is half of the grid size. If R is less than R_m, equation (2-5) is used, and if R is greater than R_m, equation (2-4) is used. The critical radius is given by,

$$R_m = \frac{U}{\sigma_w}\left(\sqrt{\frac{2}{\pi}}z_i - h\right) \qquad \textbf{(2-6)}$$

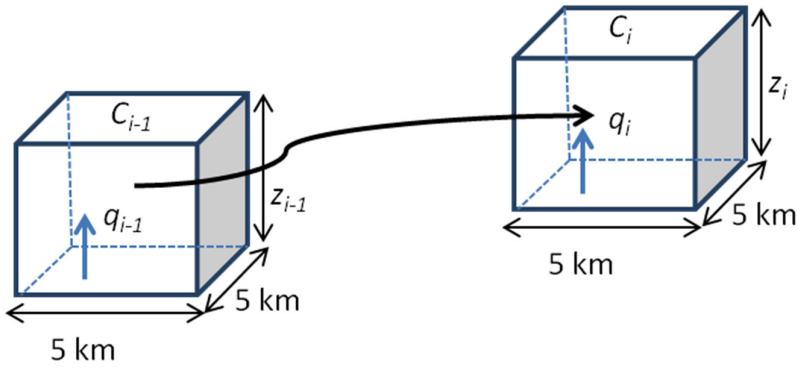

Figure 2-2: *LBM* model schematic (Adapted from Jing, 2011)

Once the concentrations of the primary pollutants are estimated, the model calculates the effective age of each species in the box (Venkatram et al., 1998, 1994). The effective age of a molecule is the time taken for the molecule to travel from source to receptor. We can build upon this simple idea to formulate a conservation equation for species age that accounts for complex flows and emissions in an Eulerian grid model. This equation allows the calculation of age in addition to concentration of a species at every receptor.

In this simple Lagrangian model the formulation for the species age, A_i, reduces to

$$A_i = A_{i-1}\left(1 - \frac{\Delta m_i}{m_i}\right) + \Delta t\left(1 - \frac{1}{2}\frac{\Delta m_i}{m_i}\right) \quad \textbf{(2-7)}$$

In the absence of fresh emissions, that is $\Delta m_i=0$ we obtain the expected result: $A_i=A_{i-1}+\Delta t$. Note that fresh emissions always decrease the effective age of the species within the box. Then, the chemical transformation of these species is estimated by reacting them with other species in the box with initial concentrations corresponding to those in the absence of chemistry. The time period for chemical calculations is specified by the end time corresponding to the time of interest and a start time that is the end time minus the species age. The chemical calculation is performed over the maximum of the ages of the species in the air parcel. In the subsequent discussion, we refer to the proposed ***L***agrangian ***B***ackground ***M***odel as *LBM*.

The chemistry, which accounts for the variation of photolysis rates with time of day, uses the Generic Reaction Set (*GRS*) chemical scheme proposed by Azzi et al (1992). This scheme approximates the reactions leading to the formation of ozone using seven reactions among seven species:

$$ROC + h\nu \rightarrow RP + ROC \quad \text{(R1)}$$

$$RP + NO \longrightarrow NO2 \quad \text{(R2)}$$

$$NO_2 + h\nu \rightarrow NO + O_3 \quad \text{(R3)}$$

$$NO + O_3 \rightarrow NO_2 \quad \text{(R4)}$$

$$RP + RP \rightarrow RP \quad \text{(R5)}$$

$$RP + NO_2 \rightarrow SGN \quad \text{(R6)}$$

$$RP + NO_2 \rightarrow SNGN \quad \text{(R7)}$$

where

ROC = reactive organic compounds

RP = radical pool

SGN = stable gaseous nitrogen product

SNGN = stable non-gaseous nitrogen product

The reactions and the corresponding reaction rates are:

R1. Radical production from photo-oxidation of ROC

$k_1 = 0.0067\, k_3\, f(T)$ where $f(T) = \exp\left(-1000\gamma\left[\frac{1}{T} - \frac{1}{316}\right]\right), \gamma = 4.7$

R2. Oxidation of nitric oxide by radicals

$k_2 = 3.58\times10^6 / T \;\; ppm^{-1}\, min^{-1}$

R3. Photolysis of nitrogen dioxide to nitric oxide

$k_3 = \exp\left(-\frac{0.575}{sin(\theta)}\right)$ where θ is the sun elevation angle.

R4. Nitric oxide-ozone titration reaction

$k_4 = 9.24 \times 10^5\, T^{-1} \exp\left(-\frac{1450}{T}\right)$

R5. Radical pool sink through recombination to stable products

$k_5 = 10200 \;\; ppm^{-1}\, min^{-1}$

R6. Sink for nitrogen dioxide to stable gaseous nitrates

$k_6 = 120 \ ppm^{-1} \ min^{-1}$

R7. Sink for nitrogen dioxide to stable non-gaseous nitrates

$k_7 = 120 \ ppm^{-1} \ min^{-1}$

Reactions R3 and R4 represent chemically exact mechanisms, while the rest approximate reactions of generic chemical counterparts. Reaction R1 is a semi-empirical representation of all the processes that lead to radical production from *VOCs* through photo-oxidation. Notice that *ROC* is conserved in the reaction; thus, *ROC* becomes a surrogate for the products of the initial oxidation of the emitted *VOCs*. Reaction R2 represents the conversion of *NO* to NO_2 by radicals. Notice that, unlike the reactions in the actual mechanism, it leads to the termination of generic radicals, *RP*. Reaction R5 represents another sink for the radical pool. Reactions R6 and R7 lead to the formation of organic and inorganic nitrates. The rates of these "pseudo" reactions have been determined empirically by fitting the ozone obtained from the *GRS* to smog chamber data. Reaction R1 is the most important reaction in the semi-empirical *GRS*. The rate of this reaction has been calibrated against the rate at which radicals are produced by the different types of *VOCs*. The reactivity coefficient, 0.0067, in R1 was derived by (Johnson, 1984) for a mixture of *VOCs* dominated by automobile emissions, and is incorporated by Hurley et al (2003) in an Eulerian air pollution model. Venkatram et al. (1994) used a slightly different

approach by converting *VOC* emissions to equivalent *ROC* by calibrating the *GRS* mechanism with a more complete chemical mechanism.

The current version of *LBM* does not simulate aerosol chemistry or other pollutants such as Persistent Organic Pollutants (*POPs*) or Heavy Metals, which are simulated by more complex models such as *CMAQ* (Matthias et al., 2008) and *CIT airshed* (Dabdub et al., 2008). As demonstrated earlier (Venkatram et al., 1998), *GRS* can be extended to include reactions to generate hydrogen peroxide, sulfuric and nitric acids, organic nitrates, and secondary organic aerosols.

LBM requires concentrations of NO_x, *VOC,* and O_3 at the boundaries of the domain where the back trajectory is terminated. Currently, their values are specified, but they could be derived from a larger scale model. A simple schematic of the *LBM* structure is shown in Figure 2-3. The next section evaluates the performance of the simplified chemistry in *LBM* by comparing two versions of *LBM*: one with *GRS* and the other with the more complete Carbon Bond IV chemistry.

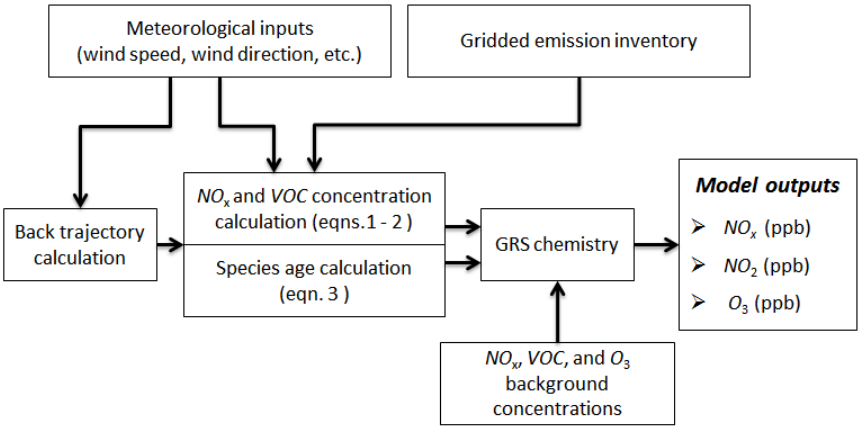

Figure 2-3. Schematic of the Lagrangian background model (*LBM*) structure.

2.2.1 GRS versus CB-IV

Pournazeri et al. (2014) has compared the results from the *LBM* that incorporates the *GRS* chemistry scheme with those from the *LBM* that incorporates the more complete Carbon Bond Model IV (*CBM IV*) mechanism. In the *CBM IV* chemistry module, the volatile organic compounds (*VOC*) are taken to be a mixture typical of ambient measurements made in Los Angeles: the *VOC* is distributed among eight surrogate species and one inert species. In these simulations, background ozone is taken to be 20 ppb.

Comparisons of the two models were done on the monthly averaged NO_x and O_3 concentrations at the 21 receptors located in the South Coast Air Basin (*SoCAB*) in southern California. The top two panels of Figure 2-4 indicate that estimates of NO_x and O_3 concentrations obtained from *GRS* and *CBM IV* follow the 1:1 line, except at small concentrations, where *CBM IV* predicts higher concentrations than *GRS*. The

maximum bias between the estimates from *GRS* and *CBM IV* is 7%. The bottom panels of Figure 2-4 show that the models predict similar diurnal variations of hourly NO_x while O_3 estimates based on *GRS* are slightly lower than those from *CBM IV* (Pournazeri et al., 2014).

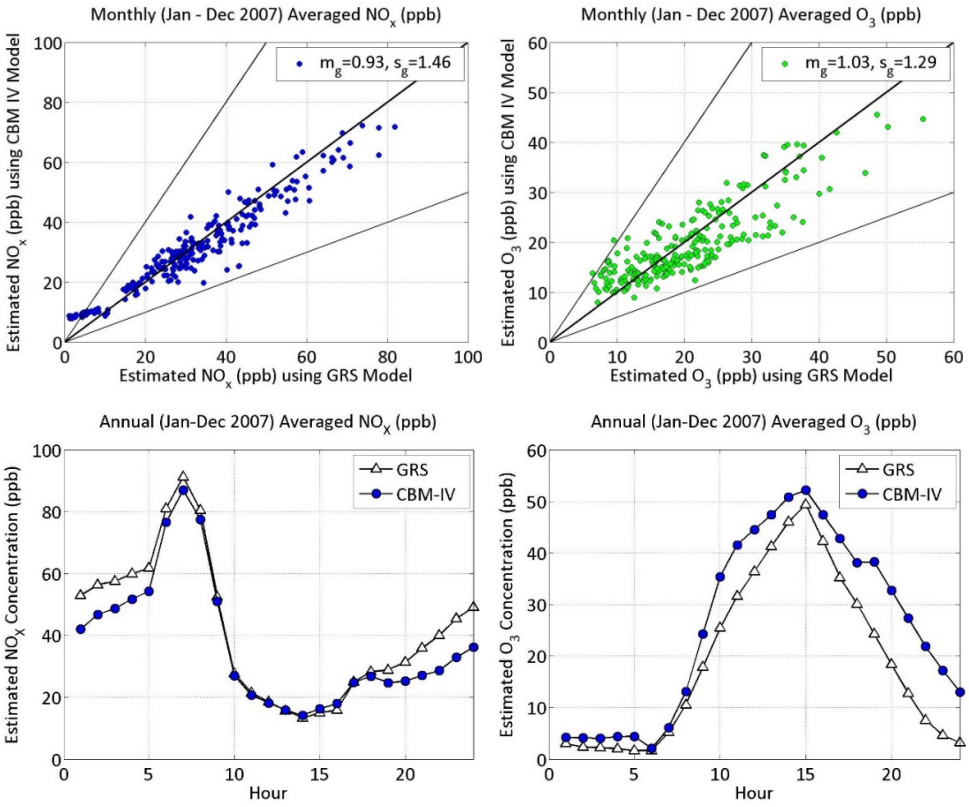

Figure 2-4: Comparison of NO_x and O_3 estimates based on *GRS* and *CBM IV* at stations in the *SoCAB*. Upper Panels: the monthly averaged NO_x and O_3 concentrations. Lower panels: daily variations of NO_x and O_3 concentrations at the San Bernardino monitoring station from January to December 2007. (Adapted from Pournazri el al, 2014).

2.2.2 LBM versus UBM

It was mentioned in the introduction that the *Urban Background Model (UBM)* is an urban dispersion model that requires minimal computational demand. Pournazeri et

al (2014) has compared the performance of *LBM* to that of *UBM*, and demonstrated that *UBM* overestimates NO_x and NO_2 concentrations while it provides relatively unbiased estimates of the O_3 concentrations, with m_g close to unity (~0.78) as shown in Figure 2-5. On the other hand, *LBM* provides unbiased estimates of concentrations: all the NO_x and NO_2 estimates are within a factor of two of the observations with a 4 - 13% bias. O_3 concentrations from both models show similar comparisons with observations.

Urban Background Model (*UBM*) | *Lagrangian Background Model* (*LBM*)

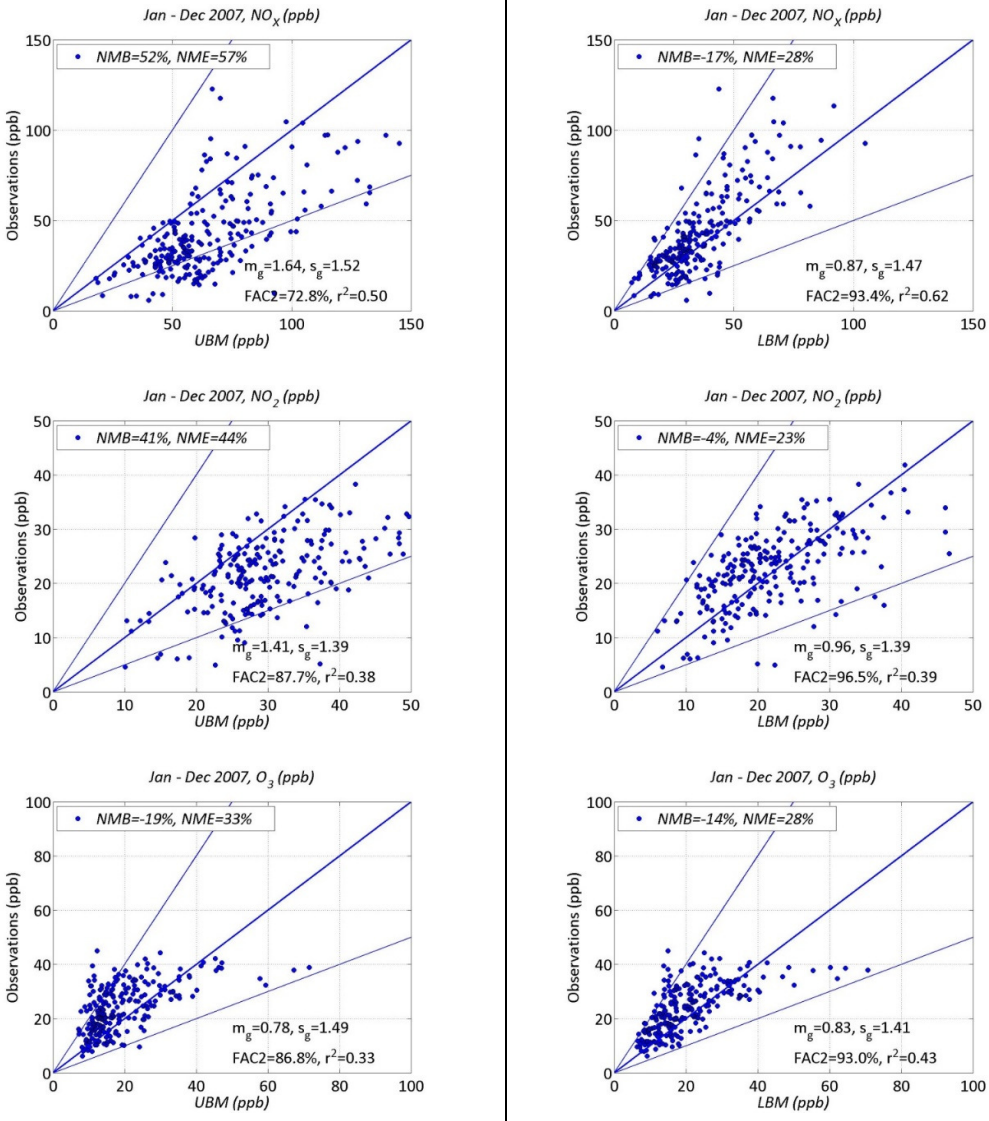

Figure 2-5: Comparison of modeled and measured monthly averaged NO_x, NO_2, and O_3 concentrations at 21 sites in the *SoCAB* from January to December 2007. Left panels: *UBM*. Right panels: *LBM*. (Figure adapted from Pournazeri et al, 2014)

2.2.3 Evaluation of LBM using San Joaquin Valley data

To measure the model performance, we use the geometric mean (m_g) and the geometric standard deviation (s_g) of the ratios of the observed to model estimates because they can be readily interpreted (Venkatram, 2008). They are defined as:

$$m_g = exp(\langle \varepsilon_m \rangle) \tag{2-8}$$

$$s_g = exp\big(\sigma(\varepsilon_m)\big) \tag{2-9}$$

where $\langle\ \rangle$ and σ represent mean and standard deviation respectively, and ε_m is the residuals between the logarithms of model estimates and observations,

$$\varepsilon_m = ln\big(C_p\big) - ln(C_o) \tag{2-10}$$

where C_o and C_p are observed values and corresponding model estimates respectively. The geometric mean is a measure of bias of the model. A geometric mean, m_g, greater than one indicates overestimation, while an m_g of smaller than one indicates underestimation. The geometric standard deviation, s_g, is a measure of the uncertainty in the model estimations, and s_g^2 is approximately the 95% confidence interval for the ratio, C_p/C_o.

The *LBM* model has been previously evaluated with data collected in the South Coast Air Basin (*SoCAB*). Jing (2011) has compared the *LBM* model estimates with observation data collected at the 21 monitoring stations in *SoCAB* in 2005, and concluded that the model provides adequate description of both the annual average

concentrations and the annual averaged 1-hr concentrations. Figure 2-6 shows the annual average NO_2 and NO_x concentrations at the 21 monitoring stations. The model shows no bias in estimating the annual average NO_2 concentrations, and it only underestimates the annual average NO_x concentrations by 19%. The r^2 of the annual averaged NO_2 and NO_x are 0.36 and 0.5 respectively. More importantly, more than 95% of the estimated NO_2 and NO_x concentrations are within a factor of two of the corresponding observed concentrations (Jing, 2011)

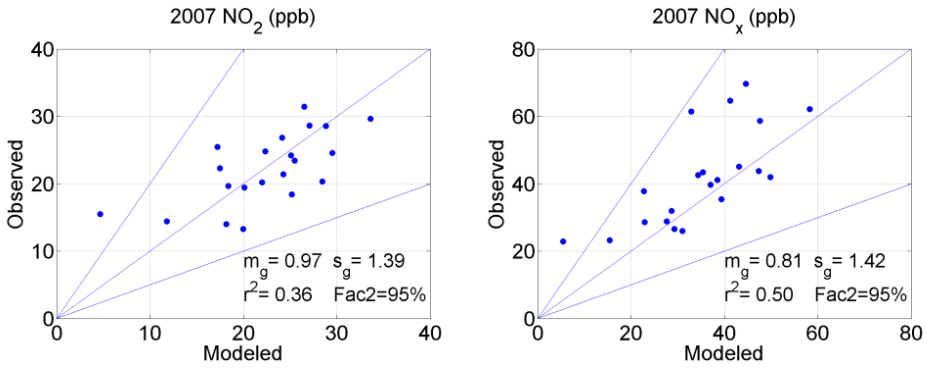

Figure 2-6 Comparison of modeled and measured annually averaged NO_2 and NO_x concentrations at 21 sites in the *SoCAB* (Adapted from Jing, 2011)

With the positive results obtained in evaluating the *LBM* model with the *SoCAB* data, we further evaluated the *LBM* with monitoring data collected in the San Joaquin Valley Air Basin (*SJVAB*). The *SJVAB* is one of the 15 air basins located in California, USA. The *SJVAB* has an area of approximately 60,900 square kilometers and is surrounded by the Coastal Range Mountains to the west, the Sierra Nevada Mountains to the east, the Transverse Range Mountains to the south, and the Sacramento Valley to the north. These mountain ranges give the Valley a bowl-shaped topography that

retains air pollutants generated by the activities of the Valley's three million residents and their two million vehicles. The presence of two major highways, CA 99 and Interstate 5, adds high vehicular emissions to the existing NO_x emissions in the valley. The San Joaquin Valley does not meet the 2008 8-hour averaged ozone national ambient air quality standards (NAAQS) of 75 ppb (Jin et al., 2011). The California Air Resources Board (*CARB*) has proposed a new state implementation (SIP) plan to attain the 1997 80 ppb 8-hour averaged ozone NAAQS in the San Joaquin Valley by June 15, 2024 (CARB, 2007).

Several studies have been conducted to examine the formation of ozone and particulate matter in the *SJVAB* (See Table 2-2 for relevant studies). Here we describe the results from the application of *LBM* to the *SJVAB* for the year 2005. The emission inventory, provided by Samuelsen et al. (2010), consists of an 80×89 grid of 4 × 4 km squares (Figure 2-7). Since the total NO_x emission in this inventory was slightly different from that reported by *CARB* as the official inventory for the year of 2005, we scaled this inventory to match the 594.6 tons per day of total NO_x emission in the SJVAB as reported by *CARB* (http://www.arb.ca.gov/ei/emissiondata.htm). High emissions occur primarily along major roads such as Interstate 5 and Highway 99, and at large cities such as Fresno and Bakersfield. The background ozone concentration is taken to be 30 ppb, and the *VOC* concentration is assumed to be a multiple of the NO_x concentration:

$$[VOC] = [NO_x] \times Ratio + [VOC]_{Background} \quad \textbf{(2-11)}$$

where the ratio is taken to be 6. This ratio is consistent with measurments of VOC/NOx ratios measured in the Los Angeles basin (Fujita et al., 2003). We then add a background *VOC* concentration of 40 ppbC for the simulation of NO_x, NO_2, and O_3 in the *SJVAB*. This value is consistent with the minimum daily averaged concentrations of non-methane hydrocarbons (*NMHC*) in the *SJVAB* reported by the Air Quality and Meteorological Information System (*AQMIS*) of the *CARB* for the year, 2005 (http://www.arb.ca.gov/aqmis2/aqmis2.php).

There are 28 ambient monitoring sites in the San Joaquin Valley study domain as shown in Figure 2-7. The red dots indicate the location of the 28 sites and the numbers are the corresponding site numbers. We simulated the concentrations at the 21 monitoring sites that are located in the valley. The 2005 hourly NO_2, NO_x, and O_3 data at the 21 sites were obtained from the *CARB* website (CARB, 2012). Sites 9 and 11 were excluded from this evaluation study because the concentrations were overestimated by a large amount and the evaluation at these two sites is not representative of the model performance. The reason for this overestimation might be due to the uncertainties in the gridded emission inventory. Both sites 9 and 11 are located in the suburbs of Fresno and Bakersfield and might have much lower emissions than that indicated by the gridded emission inventory. Wind speeds and directions measured at 11 meteorological stations in the *SJVAB* were used to compute

back trajectories. The *GRS* mechanism was used to model the chemical processes.

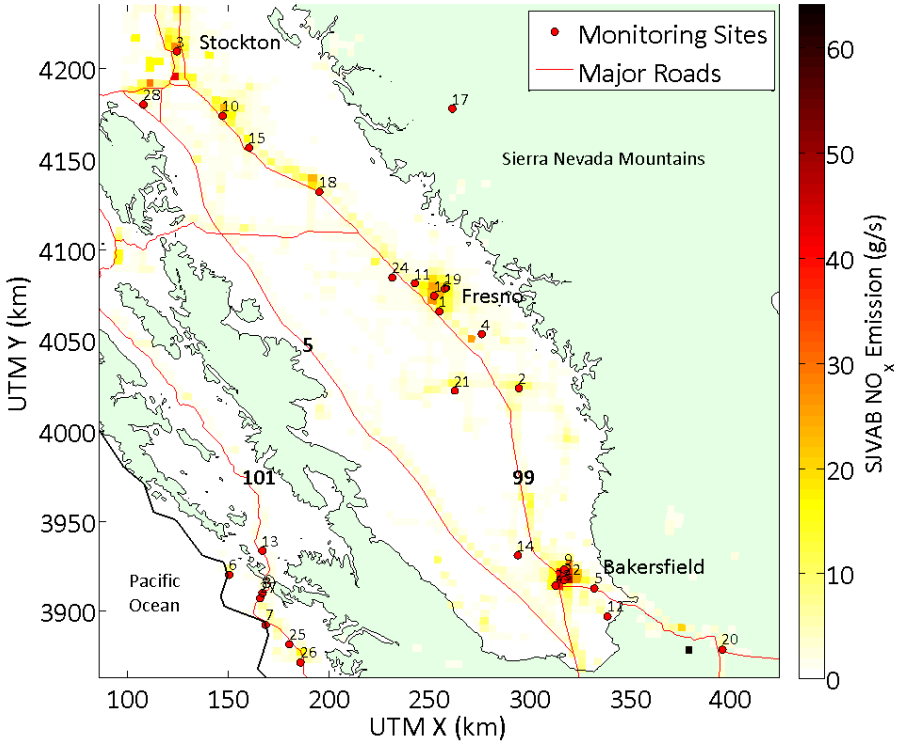

Figure 2-7: Daily average *NOx* emission in the San Joaquin Valley in 2005. Red dots indicate monitoring site locations, and the numbers are the corresponding site numbers. Note: Emissions from Highway 101 are excluded in the simulations.

Model performance is described in terms of the geometric mean and standard deviation, m_g and s_g, of the ratio of the estimated to the observed concentrations (Venkatram, 2008), the fraction of the model estimates within a factor of two of the corresponding observations, FAC2, and the correlation coefficient, r^2. The values of normalized mean bias (*NMB*) and normalized mean error (*NME*) are also provided so that the results may be compared with the evaluation studies found in the literature.

The formulas used to compute *NMB* and *NME* are,

$$NMB[\%] = \frac{\sum(C_{pi} - C_{oi})}{\sum C_{oi}} \times 100 \quad \textbf{(2-12)}$$

$$NME[\%] = \frac{\sum|C_{pi} - C_{oi}|}{\sum C_{oi}} \times 100 \quad \textbf{(2-13)}$$

where C_{pi} is the 'ith' predicted concentration and C_{oi} is the corresponding observed concentration.

Figure 2-8 shows model performance in describing annual average 1-hr NO_x, NO_2, and O_3 concentrations of 19 monitoring sites in the San Joaquin Valley. More than 85% of the modeled NO_x and 90 % of the NO_2 concentrations are within a factor of two of the corresponding observed concentrations. The predicted annually averaged 1-hr O_3 concentrations for all 19 monitoring sites are within a factor of two of observations.

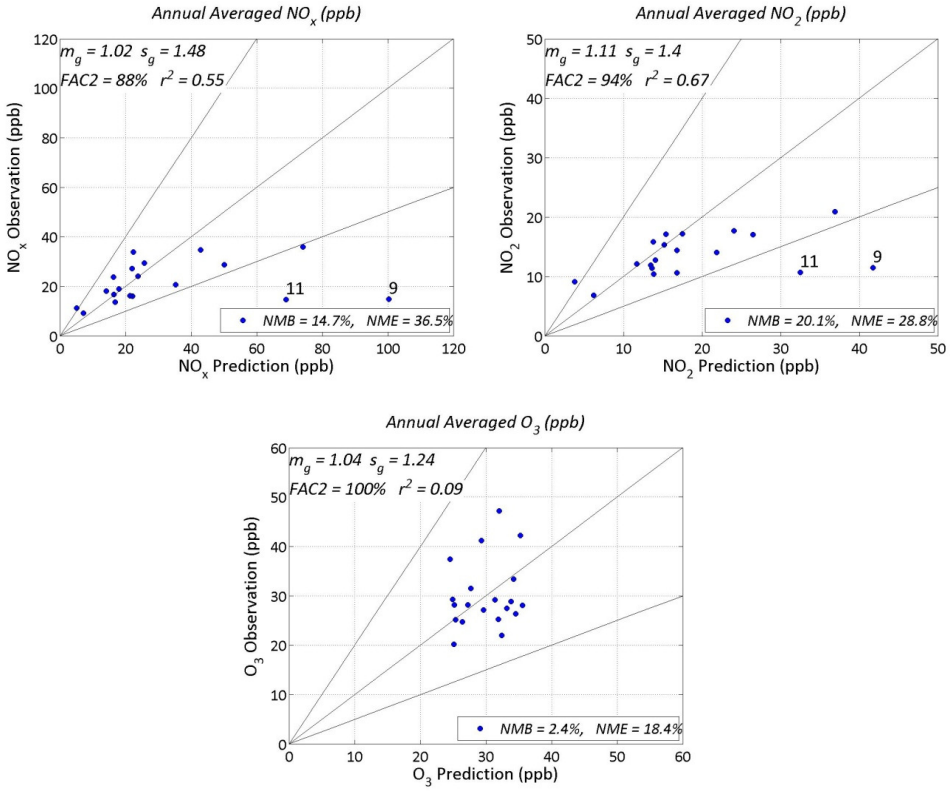

Figure 2-8: Annual average concentration of the 19 monitoring sites in the SJVAB. Upper left panel: *NOx*. Upper right panel: *NO2*. Lower panel: *O3*. Note: Statistics shown are calculated excluding site 9 and 11.

Figure 2-8 shows that *LBM* provides a good description of the spatial variation of NO_x and NO_2 at regional scales; the correlation coefficients (r^2) are 0.55 and 0.67, respectively. Figure 2-8 also indicates that the observed annual averaged O_3 in the *SJVAB* varies over a narrow range (20 - 30 ppb), except for stations 12, 17, and 20 (the relative standard deviation of the observed O_3 concentrations is about 12%). This suggests that the annual averaged O_3 is mostly driven by the background O_3, and that the high ozone events are relatively infrequent. With m_g close to unity (=1.02, 1.11, and 1.04 for NO_x, NO_2 and O_3, respectively), the model shows little or no bias in

estimating the annual average NO_x, NO_2 and O_3 concentrations.

We next examine the performance of *LBM* in the San Joaquin Valley in more detail at two of the 19 monitoring sites: Site 5, which is located near Bakersfield, and Site 14, which is located in Shafter, a town 26 kilometers northwest of Bakersfield. Figure 2-9 compares the modeled daily averaged NO_x, NO_2, and O_3 concentrations to the corresponding observed concentrations at these two sites. The left panels of the figure show that the model provides an adequate description of the daily average NO_x, NO_2, and O_3 concentrations at Bakersfield, while it slightly underestimates and overestimates the NO_x and NO_2 concentrations in Shafter, respectively. More than 80% of the modeled NO_x and NO_2 concentrations are within a factor of two of the corresponding observed concentrations. Even though the correlation (r^2) between the modeled and observed daily average NO_x and NO_2 ranges from 0.25 to 0.4, the modeled daily average O_3 concentration correlates well with the observed O_3 concentration as seen in the lower panels of Figure 2-9 (r^2 is 0.58 and 0.79 at site 5 and 14, respectively).

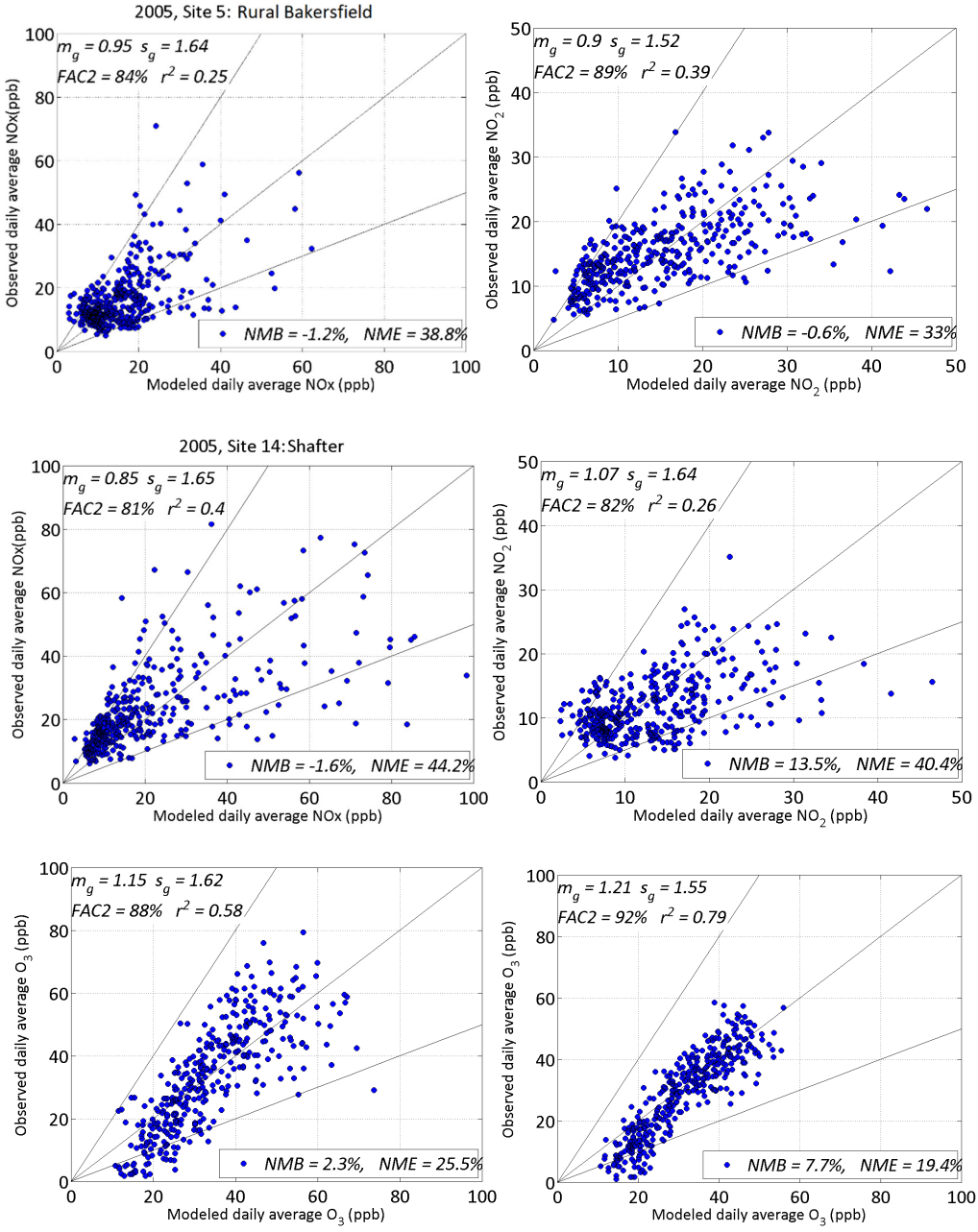

Figure 2-9: Comparison of modeled daily-average concentrations with the corresponding observed concentrations. Upper Panels: *NO_x*, Middle Panels: *NO_2*, and Lower Panels: *O_3*. Left panels correspond to Site 5, and right panels correspond to Site 14.

Figure 2-10 compares the modeled daily maximum NO_x, NO_2, and O_3 concentrations to the observed concentrations at sites 5 (Bakersfield) and site 14 (Shafter) for the whole year of 2005. We see that the model performs reasonably well at site 5 while at site 14 it slightly under/overestimates NO_x and NO_2 concentrations, respectively. At both sites 5 and 14, about 90% of the modeled daily maximum O_3 concentrations are within a factor of two of the corresponding observed concentrations. Statistics of the model performance show that the scatter (s_g^2) of the predicted daily maximum O_3 is less than 2.3 (s_g^2 = 2.28 at site 5), and the bias (m_g) is 20% and 11% at site 5 and 14, respectively. The correlation of observed and predicted daily maximum O_3 is relatively high at site 14 (r^2 = 0.61) while it is 0.25 at site 5.

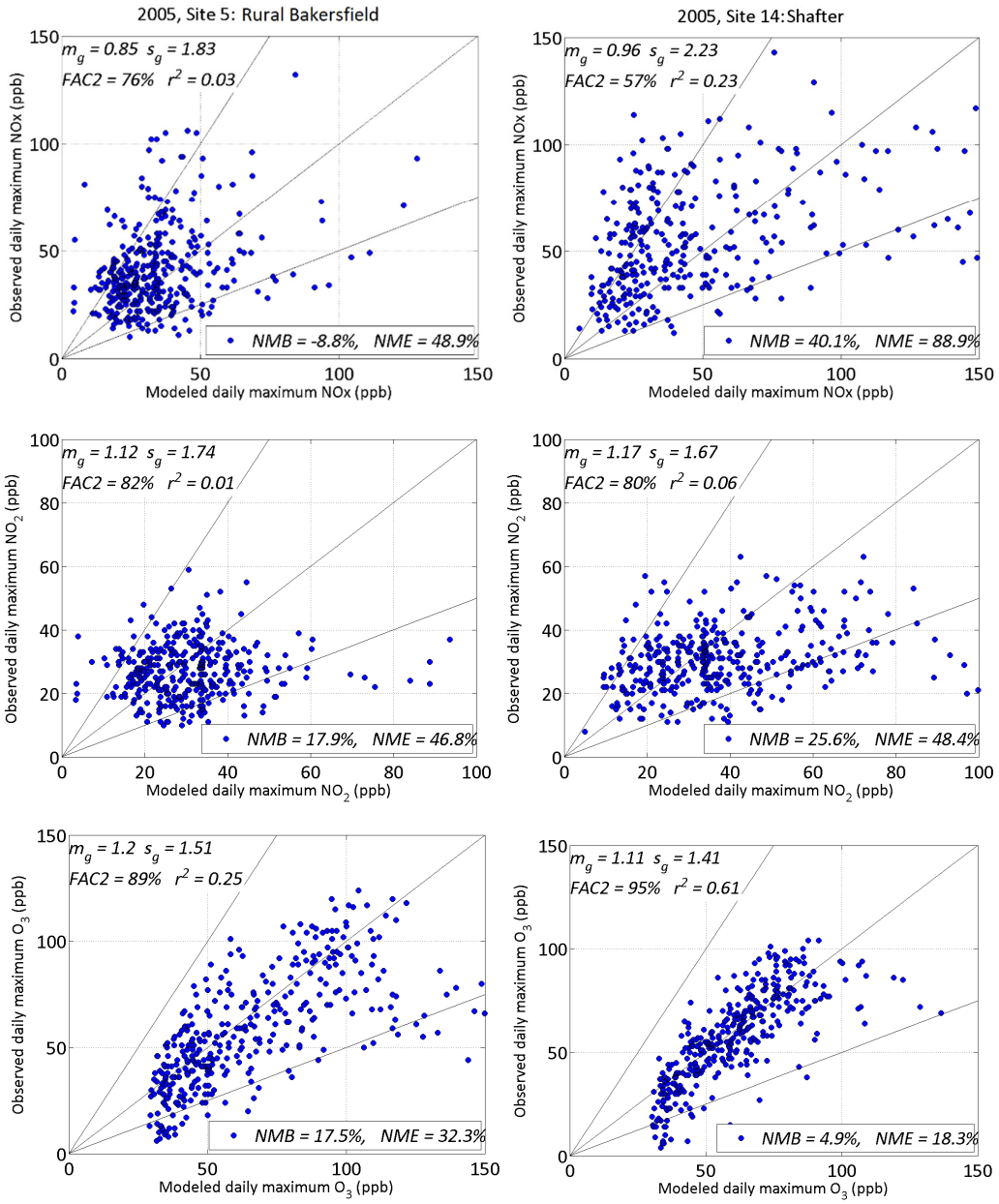

Figure 2-10: Comparison of modeled daily maximum concentrations with the observed concentrations for sites 5 and 14 from January – December 2005. Upper Panels: *NO_x*, Middle Panels: *NO_2*, and Lower Panels: *O_3*. Left panels correspond to Site 5, and right panels correspond to Site 14

The ability of *LBM* in reproducing the seasonal variations of NO_2, NO_x and O_3 concentrations is depicted in Figure 2-11.

Table 2-1 provides performance measures of *LBM* in describing the daily average and maximum NO_2 and O_3 concentrations at two sites in the *SJVAB*.

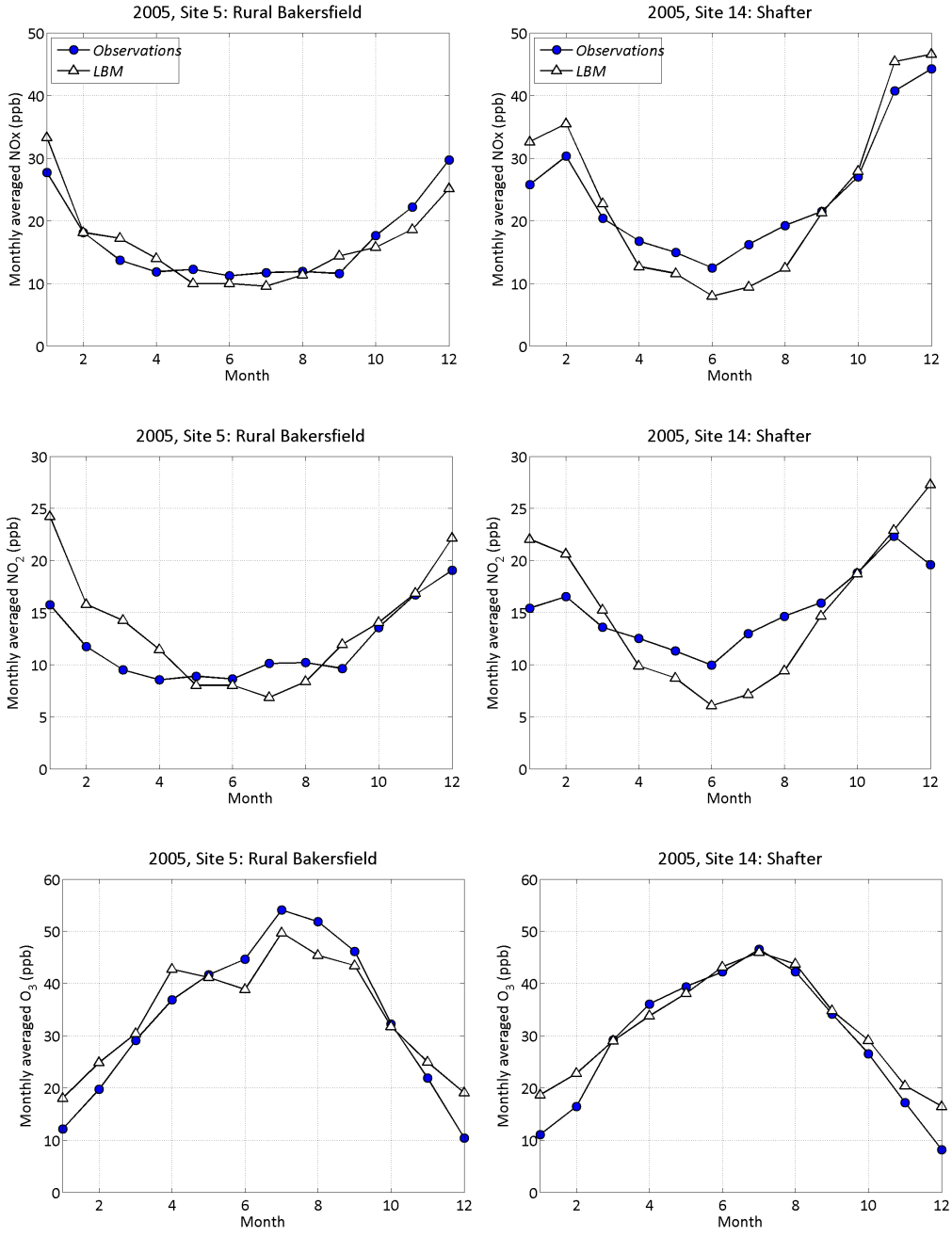

Figure 2-11: Modeled monthly averaged concentration compared with corresponding observed concentration for each month of the year at site 5 and 14. Upper Panels: *NO_x*, Middle Panels: *NO_2*, and Lower Panels: *O_3*. Left panels correspond to Site 5, and right panels correspond to Site 14.

Table 2-1: Statistical performance measures of the *LBM* model for calendar year 2005 at two sites (Bakersfield and Shafter) in *SJVAB*.

Species		*NMB* [a] *(%)*		*NME* [b] *(%)*		r^2	
		Bakersfield	***Shafter***	***Bakersfield***	***Shafter***	***Bakersfield***	***Shafter***
NO_2	***Daily Max***	*17.9*	*25.6*	*46.8*	*48.4*	*0.01*	*0.06*
	Daily Average	*13.5*	*-0.6*	*40.4*	*33*	*0.26*	*0.39*
O_3	***Daily Max***	*17.5*	*4.9*	*32.3*	*18.3*	*0.25*	*0.61*
	Daily Average	*2.3*	*7.7*	*25.5*	*19.4*	*0.58*	*0.79*

a: Normalized Mean Bias

b: Normalized Mean Error

In order to compare the performance of *LBM* to comprehensive models such as *CMAQ*, we analyzed two O_3 episodes in site 5 (July 10 – 14, 2005) and site 14 (June 11 – 15, 2005) as shown in Figure 2-12, and evaluated the performance of the model for these two episodes. Results from this evaluation were compared to those from Vijayaraghavan et al. (2006), presented in Table 2-2. This comparison revealed that the performance of *LBM* in predicting the daily maximum O_3 is comparable to that of the comprehensive regional photochemistry models such as *CMAQ*. The *NMB* values for daily maximum O_3 from Vijayaraghavan et al. (2006) are between 3.9% and 61.1%, while the *NMB* of *LBM* are 9% and 8% for site 14 and 5, respectively. Similarly, the *NME* values from *LBM* are in the range of 8% to 9%, while *CMAQ* shows values of 15% to 60% (Vijayaraghavan et al., 2006).

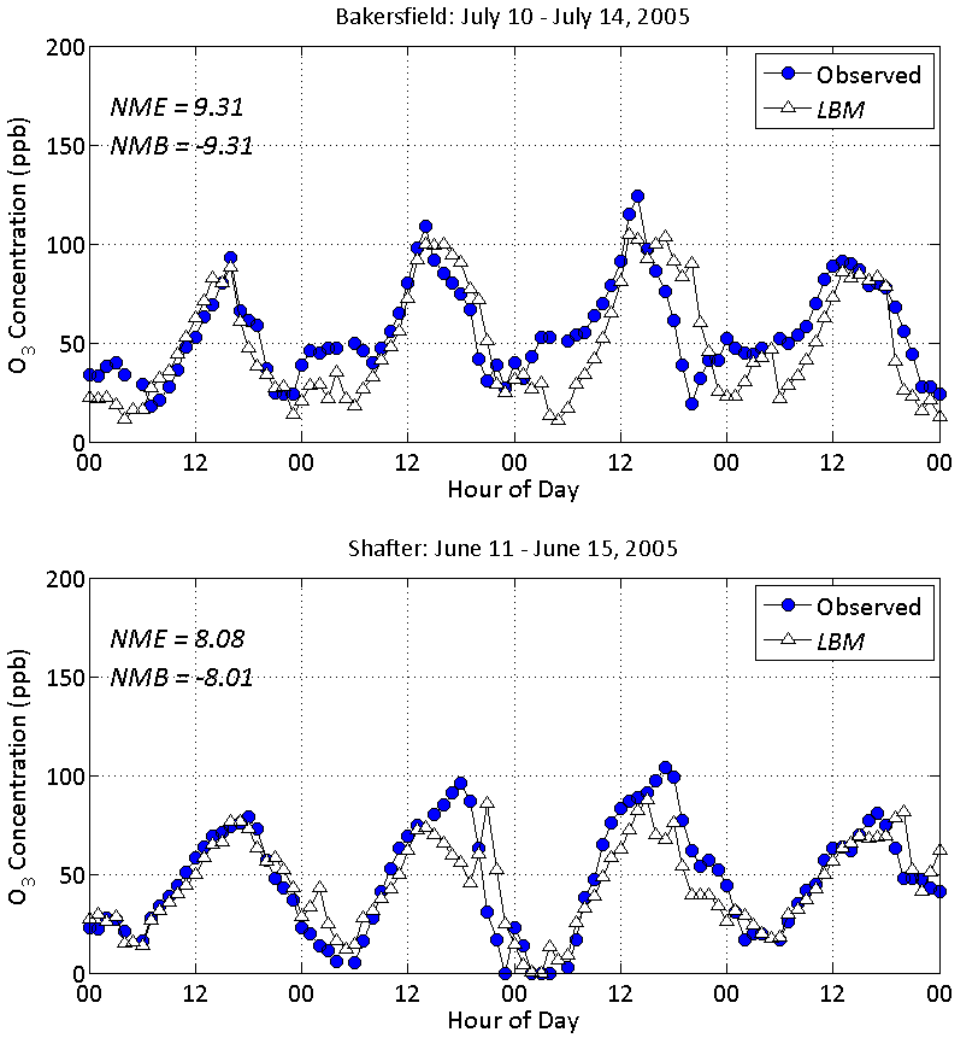

Figure 2-12 O_3 episodes during July 10th to 14th, 2005 in Bakersfield in the *SJVAB* (top panel) and June 11th to 15th, 2005 in Shafter in the *SJVAB* (bottom panel). The *NMB* and *NME* values are calculated based on the daily maximum O_3 concentrations.

Figure 2-13 shows that the modeled daily variations averaged over a year correlate well with the corresponding observed variations. At site 5, the modeled NO_x concentrations clearly show a diurnal variation with the maximum occurring during rush hours, which differs slightly from the observed variations. At site 14, the model slightly overestimates NO_x concentration from midnight to 5am. The lower panels of

Figure 2-13 show that the model can estimate the daytime O_3 concentration well, but it slightly overestimates during nighttime. Although emissions are relatively low during nighttime, the high nighttime NO_x concentrations are related to the choice of the boundary layer height, the estimation of which is highly uncertain (Pournazeri et al., 2012). The *LBM* program is implemented in MatLab, and the one year simulation of hourly concentrations at 28 receptors in the *SJVAB* took approximately 145 minutes to run on a machine with a 4 core Intel i7-920 2.67 GHz processor and 6 GB of ram.

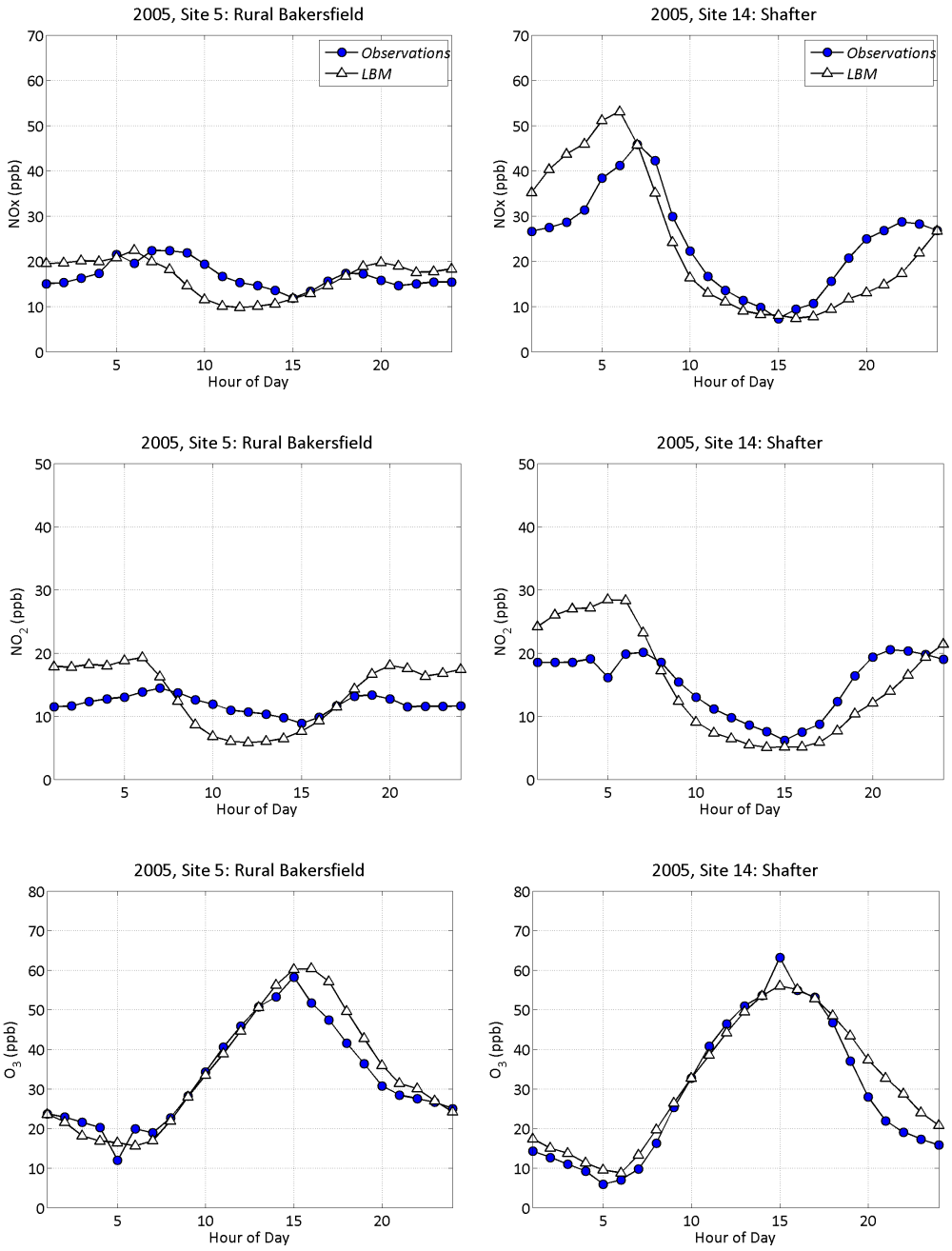

Figure 2-13: Modeled annual averaged daily variation of NO_x, NO_2 and O_3 concentration compared with corresponding observations. Upper Panels: NO_x, Middle Panels: NO_2, and Lower Panels: O_3. Left panels correspond to Site 5, and right panels correspond to Site 14.

How do the performance measures of *LBM* compare with those of more comprehensive models such as *CMAQ*? Table 2-2 compares the performance of *LBM* with those of comprehensive models. Eder and Yu (2006) compared a full year of concentrations from *CMAQ* simulations to data from four nationwide monitoring networks (*IMPROVE, STN,CASTNET, and ARIS-AQS*) in the United States. *CMAQ*'s performance at estimating criteria pollutants and particulate matter (*PM*) concentrations varies significantly. Estimates of 1-hr and 8-hr peak O_3 concentrations compare well with data, with correlation coefficients, r^2, of 0.46 and 0.47 respectively. However, *CMAQ* does not show comparable performance in estimating nitrate (NO_3^-) concentrations with r^2 ranging from 0.13 to 0.38. *CMAQ* (Smyth et al., 2006) captures the spatial and temporal distribution of O_3 concentrations measured during the *Pacific 2001* experiment (Li, 2004). Liu et al (2010) applied *CMAQ* to study the formation and seasonal variations of major pollutants such as SO_2, NO_2, and PM_{10} in China during January, April, July, and October of 2008. The predicted surface NO_2 concentrations were significantly smaller than the corresponding observed concentrations for all four months, and the mixing ratios of the maximum O_3 concentration in January and July are over-predicted. Vijayaraghavan et al. (2006) evaluated *CMAQ*'s performance against an episode from the Central California Ozone Study (CCOS) in July and August 2000. This study found that *CMAQ* underestimates 1-hr O_3 concentrations. Zhang et al. (2009) conducted a comprehensive study to

evaluate *CMAQ*'s ability to reproduce the long-term variation of pollutants such as O_3. The study compared results from a *CMAQ* simulation of a full year to both ground-based and satellite measurements; the normalized mean bias ranges from 11% to 0.1% for the annual maximum 1-hr O_3 mixing ratio (Zhang et al., 2009).

The California Institute of Technology (*CIT*) Airshed model is another comprehensive air quality model that is widely used (Carreras-Sospedra et al., 2010; Cohan et al., 2008; Ensberg and Dabdub, 2010) for regional air quality studies in Southern California. McNair et al. (1996) evaluated the *CIT Airshed* model against the Southern California Air Quality Study (SCAQS; (Taylor and Lawson, 2014) database and concluded that the *CIT Airshed* model is able to predict the diurnal variation of the reactive species and the transport of the relatively non-reactive species.

A comparison between the values listed in Table 2-2 shows that the performance of *LBM* is comparable to that of complex models such as *CMAQ* and *CIT Airshed*. The *NMB* is less than 45% and the *NME* is within 25 – 50%.

Table 2-2 Statistical Parameter of various air quality models

Study	Region/Database	Species	Model	Data Type	Simulation Period	NMB [a] (%)	NME [b] (%)	r^2
Eder and Yu (2006)	IMPROVE, STN, CASTNET, ARIS-AQS	O_3	CMAQ[1]	Daily Maximum of 1-hr average	April–Sep, 2001	4.0	18.3	0.46
Liu et al (2010)	Eastern China	NO_2	CMAQ[2]	Monthly average of daily average	Jan, Apr, Jul, and Oct 2008	-6.5~-32.0 [d]	47.1~66.6 [d]	0.09~0.36[d]
Liu et al (2010)	Eastern China	O_3	CMAQ[2]	Daily maximum of 1-hr average	Jan, Apr, Jul, and Oct 2008	1.1~12.0 [d]	16.9~36.6 [d]	0.5~0.7
McNair et al (1996)	Southern California, US	NO_2	CIT Airshed[3]	1-hr Average	June 25th, 1987	--	69 [c]	0.1
McNair et al (1996)	Southern California, US	NO_2	CIT Airshed[3]	1-hr Average	August 28th , 1987	--	44 [c]	0.52
McNair et al (1996)	Southern California, US	O_3	CIT Airshed[3]	1-hr Average	June 25th 1987	--	38 [c]	0.83
McNair et al (1996)	Southern California, US	O_3	CIT Airshed[3]	1-hr Average	August 25th 1987	--	29 [c]	0.82
Smyth et al (2006)	Vancouver, Canada	O_3	CMAQ[4]	Daily maximum of 1-hr average	August 9th -20th 2001	-2.2	24.3	--
Vijayaraghavan et al (2006)	Central California, US	O_3	CMAQ[5]	1-hr Average	Jul 30th -Aug 1st 2000	-3.9~-61.1 [e]	15.5~61.1 [f]	--
Zhang et al (2009)	IMPROVE, STN, CASTNET, ARIS-AQS, SEARCH, NADP	O3	CMAQ[1]	Daily maximum of 1-hr average	2001	0.1~ -11.6	19.8~20.5	--

a: Normalized Mean Bias

b: Normalized Mean Error

c: Normalized Gross Error

d: Based on surface concentrations using 36 km horizontal grid spacing

e: Normalized Bias

f: Normalized Erro

AIRS-AQS*:Aerometric Information Retrieval System-Air Quality Subsystem. Contains 1161 sites located primarily in cities and towns in the U.S.*

CASTNET: *Clean Air Status and Trends Network. Contains 83 sites located primarily in remote/rural areas in the U.S.*

IMPROVE*: Interagency Monitoring of Protected Visual Environments. Contains 134 sites located primarily in remote areas in the western U.S.*

NADP: *National Acid Deposition Program. Contains 250 sites nationwide in the U.S.*

SEARCH: *Southeastern Aerosol Research and Characterization. Contains 8 sites located in the urban/suburban areas in the southeastern U.S.*

STN*: Speciated Trends Network. Contains 139 sites in urban areas in the U.S*

2.2.4 Sensitivity Studies

The comparison of model estimates with observations shows that the *LBM*, despite its simplicity, can adequately predict concentrations of NO_2 and ozone (O_3), which leads us to ask what elements of the model are the most important for producing these estimates. To answer this question we performed sensitivity studies of the effect on the concentration estimates of various parameters such as: the emission distribution, wind speed, wind direction, boundary layer height, species age, and back-trajectory tracing time. These variables were modified within the model, and the resulting annual average NO_x, NO_2, and O_3 concentrations were compared with the observed concentrations. The corresponding geometric mean (m_g) and geometric standard deviation (s_g) are shown in Table 2-3. The sensitivity test cases included in the table are: (1) the wind speed is doubled, (2) 90° is added to the wind direction, (3) the emissions are made spatially uniform, (4) the boundary layer height is set to a constant for each 24-hour period, (5) the species age is doubled, (6) the back-trajectory tracing time is increased to 48 hours and (7) 72 hours, and (8) the back-trajectory tracing time is increased to 48 hours, and the boundary layer height is set to a constant. We also compared the diurnal variations of the concentrations of cases 3, 4, 5, 6, and 8, and the plots are shown in Figure 2-14, Figure 2-15, and Figure 2-16.

We also formulated a simple model where the concentration is calculated as:

$$C = \frac{QT}{z_i} \quad \textbf{(2-14)}$$

where T = 3600s, and Q and z_i are the emission rate and boundary layer height within the local grid square. The results of equation (2-14) are shown in Table 2-3 as Case 9.

Table 2-3: Comparison of m_g and s_g for the different cases of the sensitivity study

Case Number	Type of Sensitivity Study	m_g			s_g		
		NO_x	NO_2	O_3	NO_x	NO_2	O_3
0	Base Model (Original Met)	1.02	1.11	1.04	1.48	1.4	1.24
1	Wind Speed × 2	0.82	0.94	0.98	1.38	1.29	1.22
2	Wind Direction + 90°	0.85	0.97	1.04	1.44	1.36	1.2
3	Uniform Emission	0.42	0.53	0.84	3.86	4.79	3.08
4	Constant BL Height	1.18	1.37	1.2	1.4	1.36	1.26
5	Species Age × 2	1.02	1.27	1.66	1.48	1.55	1.42
6	48-hr Trajectory	1.07	1.27	1.41	1.47	1.48	1.39
7	72-hr Trajectory	1.08	1.29	1.61	1.47	1.5	1.49
8	48-hr + Constant BL Height	1.68	2.01	1.78	1.41	1.37	1.48
9	Simple Model ($C = QT/z_i$)	2.37	--	--	3.02	--	--

Cases 1 (*Wind Speed× 2)* and Case 2 (*Wind Direction +90°)* do not significantly change the model estimates relative to the unmodified *LBM*. This is likely because the modified trajectory still passes through grid squares with emissions that are similar to those of the unmodified trajectory. The model sensitivity to wind speed and direction must depend on the emission distribution because the function of the trajectories is to select the grid squares from which emissions contribute to the predicted concentrations. If the emission distribution within the San Joaquin Valley were less homogeneous, then the model would likely be more sensitive to the wind speed and direction. This study also validates our choice of the surface winds, rather than the upper air winds, for calculating the trajectories in the *SJVAB* and *SoCAB* because the model estimates are not very sensitive to the wind speed in these domains.

Making the emissions within the San Joaquin Valley spatially uniform (right panels of Figure 2-15) causes the model to underestimate NO_x, NO_2, and O_3 concentrations significantly, which indicates that the emission distribution is a key element of the model. Figure 2-15 shows that the model does not predict the peak in NO_x, which occurs around 7 a.m. when the emissions are made uniform. The peak in concentration occurs due to the large emissions that occur in Bakersfield, Fresno, and Stockton during rush hour and are then transported to the surrounding sites. When the emissions are made uniform, the large emissions are no longer associated with these geographic locations, so the model underestimates concentrations at the surrounding

sites.

The modeled boundary layer height has a significant effect on the predicted concentrations. We found that replacing the boundary layer height with the 24-hour average value causes the model to underestimate concentrations during the day and overestimate them during the night, as shown in the left panels of Figure 2-15. This shows that the boundary layer height formulation is important for predicting the daily concentration variation.

Figure 2-14 shows the model results when the species age is doubled (Case 5). As shown, doubling the species age resulted in an increase in the O_3 m_g from 1.04 to 1.66, and the model cannot predict the correct O_3 diurnal variation (peak during noon). The m_g of NO_2 also increased from1.11 to 1.27 as a result of doubling the species age. Also, the model predicted NO_2 shows an unrealistically large peak during the night. This shows that our formulation of species age is useful for predicting the chemical processes separately from the transport.

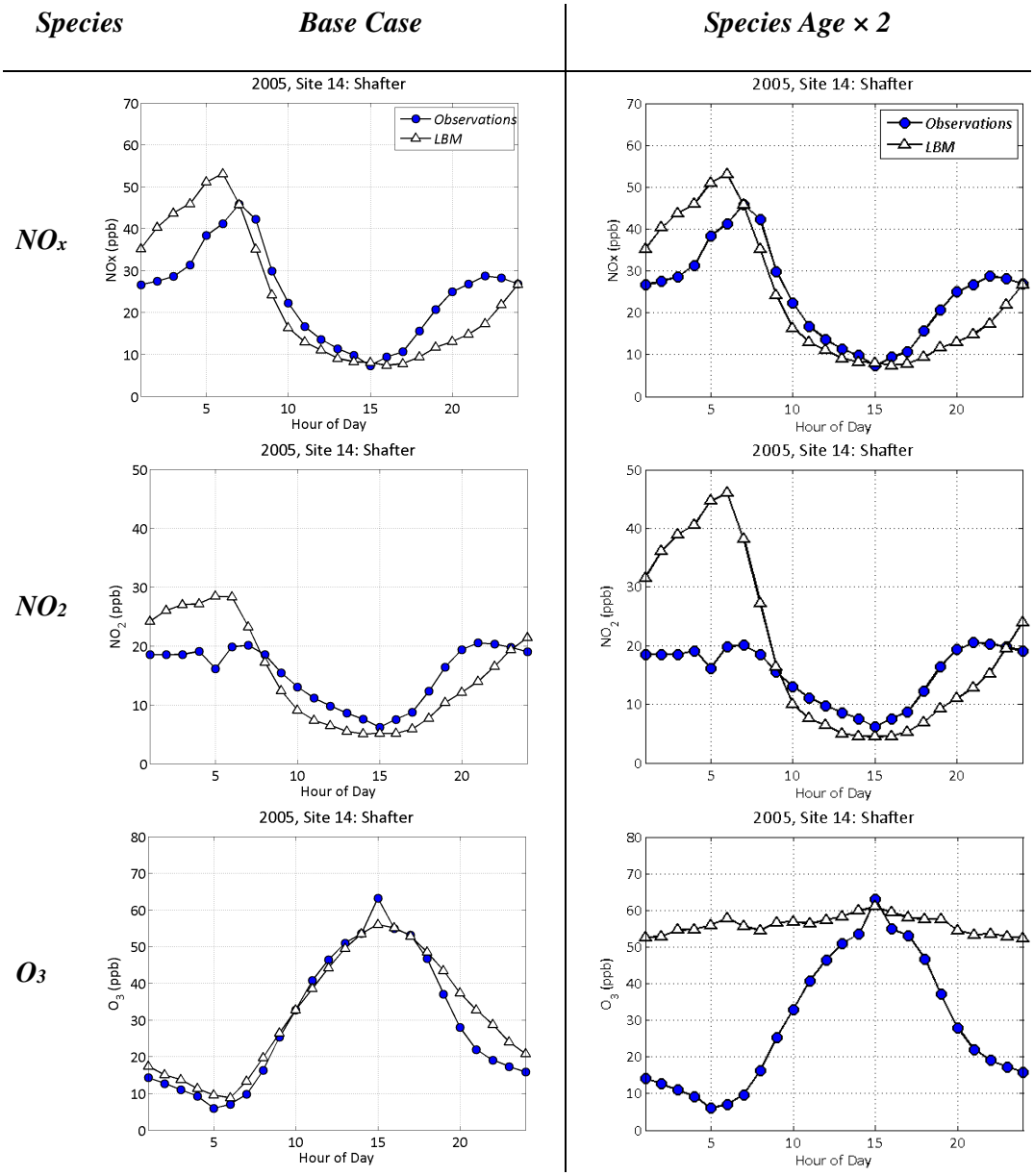

Figure 2-14: Hourly concentration variation for the base case with no changes to the *LBM* (left panels) and the case when the species age is doubled (right panels)

Species	*Constant Boundary Layer Height*	*Uniform Emission within the Valley Region*
NOx	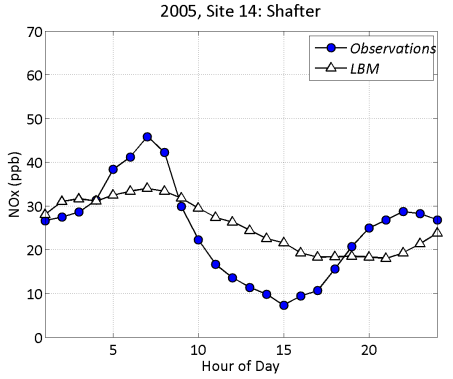	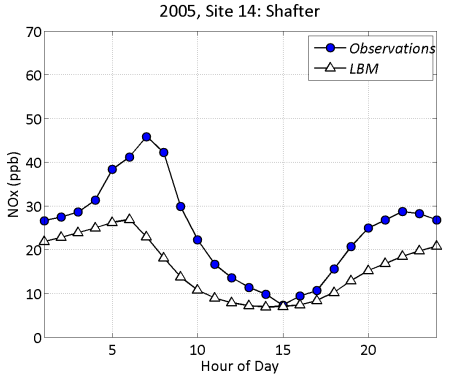
NO2	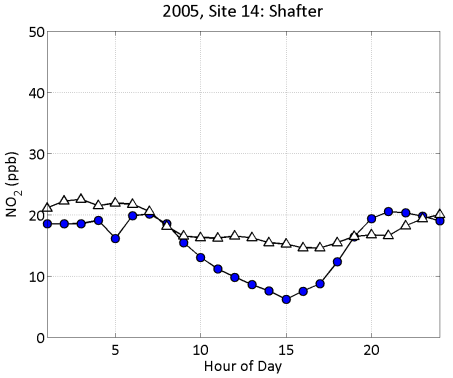	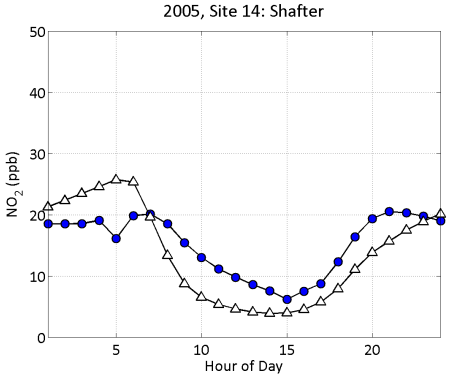
O3	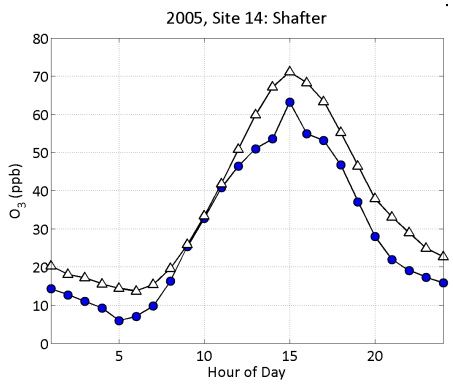	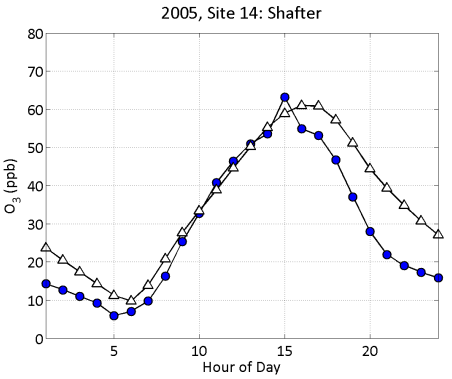

Figure 2-15: Hourly concentration variation for the constant boundary layer height case (left) and the uniform emission distribution case (right)

In this formulation of the *LBM*, trajectories were traced back over a 24-hour time period, but the choice of this time scale could alter concentration predictions. When the time period was increased from 24 hours to 48 hours and 72 hours, the predicted

NO_x concentrations did not change significantly, but the model overestimated the O_3 and NO_2 concentrations at night. The NO_x is unchanged because of the boundary layer height variation over a 24-hour period; when the boundary layer collapses at dusk, the pollutant mass above the nighttime boundary layer height is lost, which reduces the total mass that the model accumulates over a 24-hour period and limits the concentration increase over time periods greater than 24 hours. This can also be seen in the model sensitivity in Case 8, where the boundary layer height was set to a constant over each 24-hour day and the back trajectory was calculated over 48 hours. The model overestimated NO_x by about 70 percent in this case because the boundary layer height did not decrease at the beginning of each night, so the model could accumulate a larger pollutant mass.

Figure 2-16 shows the hourly concentration variation for Case 6 (*48-Hr Trajectory*) and Case 8 (*48-Hr Trajectory + Constant BL Height*). The effect of increasing the back-trajectory time on NO_2 and O_3 is similar to that of increasing the species age (as shown in the right half of Figure 2-14 and the left half of Figure 2-16). This gives credence to the boundary layer height formulation used in the *LBM*, since it naturally limits the concentration from upwind sources in the same manner as could be expected to occur in nature.

Species	*48-Hr Trajectory*	*48-Hr Trajectory + Constant BL Height*
NO_x	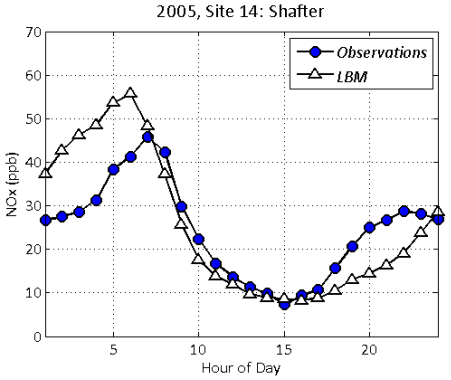	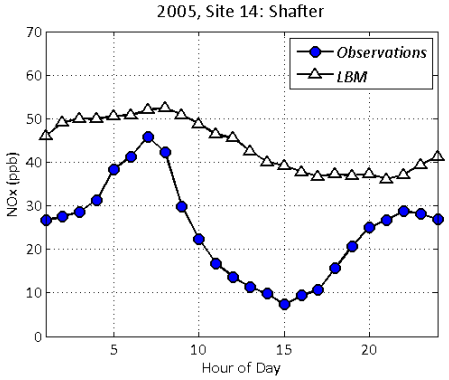
NO_2	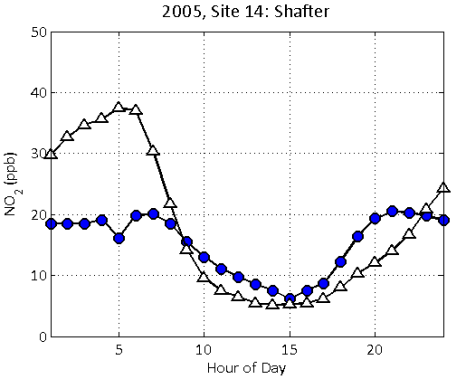	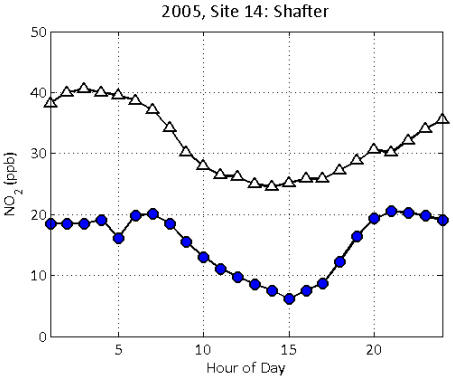
O_3	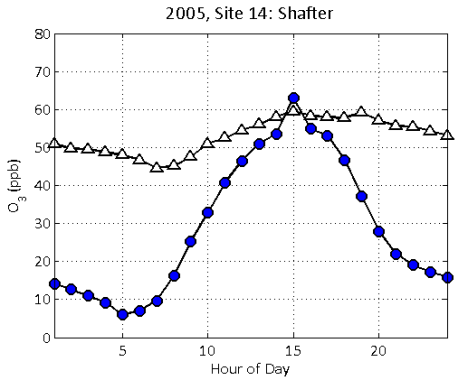	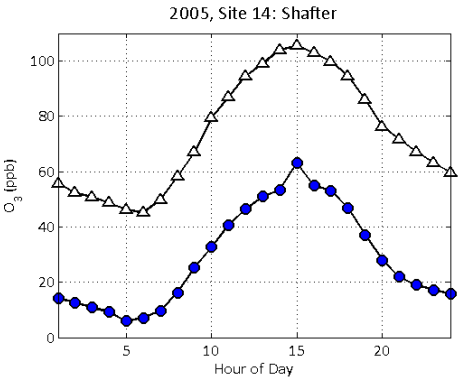

Figure 2-16 Hourly concentration variation for the 48-hour back trajectory case (left panels) and the 48-hour back trajectory and constant boundary layer height case (right panels).

The simple model described by equation (2-14) overestimates NO_x by more than a factor of 2. This is because the emission rate in equation (2-14) is the local emission rate, which is larger than the average emission rate the back trajectory would have

encountered as it passed through the domain. This shows that the emissions from upwind locations must be taken into account when calculating concentrations, which justifies our use of the Lagrangian trajectory model.

2.3 Combining Model Estimates and Observations using Kriging

In this section, we describe how to combine model estimates and observations using Kriging interpolation. Geo-statistical interpolation techniques such as Kriging are commonly used to interpolate observations made at irregularly spaced locations, such as air quality monitoring sites. A detailed derivation of Kriging interpolation can be found in (Venkatram, 1988). Kriging is used to estimate the concentration, Z_o, at location x_o, where there are no available observations, using observations $Z(x_j)$ at locations x_j. Similar to other interpolation techniques, Kriging assumes that variable Z can be represented as the sum of a deterministic component (trend) $m(x)$ and a local fluctuation component ε(x), as shown in Equation (2-15).

$$Z(x) = m(x) + \varepsilon(x) \quad \textbf{(2-15)}$$

where m is the mean and ε is the local fluctuating component that varies from realization to realization. In simple Kriging, the deterministic component or mean, $m(x)$, is assume to be constant across the field.

Kriging assumes that $\hat{Z}_o$, the estimate of Z_o, can be expressed as a linear combination of the observations,

$$\hat{Z}_o = \sum_{j=1}^{N} \lambda_j Z_j \tag{2-16}$$

where λ_j are the weights assigned to the observation points Z_j. The weights can be calculated using the following set of equations.

$$\sum_{i=1}^{N} \lambda_i \gamma_{ij} + \mu = \gamma_{io} \tag{2-17}$$

$$\sum \lambda_i - 1 = 0 \tag{2-18}$$

where γ_{ij} is the semi-variogram, also an ensemble-averaged quantity.

$$\gamma_{ij} = \langle \left(Z_i - Z_j\right)^2 \rangle /2 \tag{2-19}$$

Calculating the ensemble-averaged semi-variogram is not possible using observations, since it requires numerous sets of observations with the same *m(x).* However, we can formulate a model for γ_{ij} using the available observations, with the assumption that γ_{ij} is only a function of the separation distance (X_i-X_j). Common functions for variograms are shown in Figure 2-17.

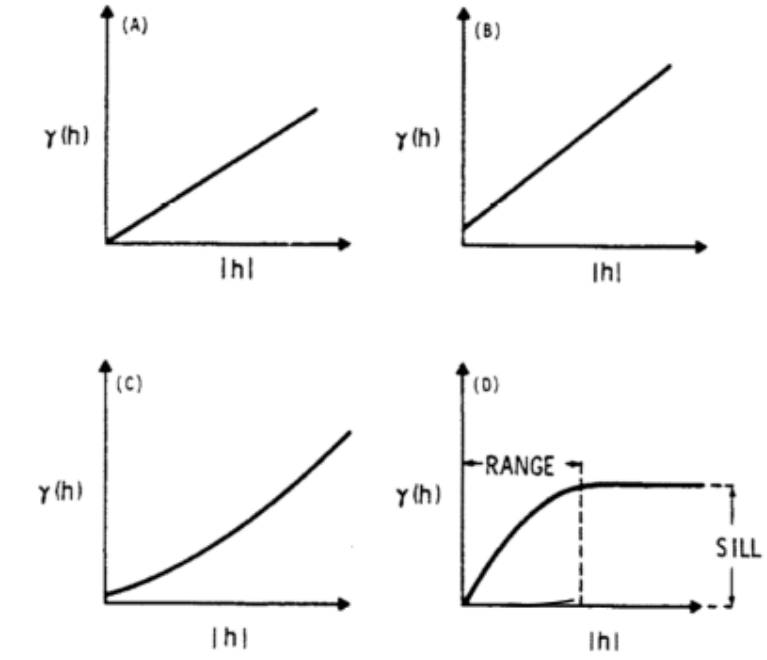

(A) Linear: $\gamma(h) = a \cdot |h|$

(B) Linear with nugget: $\gamma(h) = a \cdot |h| + b$, for $|h| > 0$, (b is the "nugget effect")
$= 0$ for $|h| = 0$

(C) Power function with nugget: $\gamma(h) = a \cdot |h|^k + b$, for $|h| > 0$, $(1 < k < 2)$
$= 0$ for $|h| = 0$

(D) Spherical: $\gamma(h) = C \cdot \left[\frac{3}{2}\frac{|h|}{a} - \frac{1}{2}\left(\frac{|h|}{a}\right)^3\right]$, for $0 \leq |h| < a$
$= C$, for $|h| \geq a$
(C is the "sill," a is the "range")

Figure 2-17 Common functions for semi-variogram (adapted from Barnes, 1980)

Since the assumption of constant trend used in simple Kriging is not likely to be true for concentration fields whose underlying spatial structure is governed by those of emissions and meteorology, simple Kriging cannot be readily applied to interpolate concentrations. Concentrations estimated from dispersion models are directly associated with emissions and meteorology, and should represent the underlying trend of the concentration field. Thus model estimates can be used to substitute the

underlying structure in the concentration field (Venkatram, 1988). The residuals between model predictions and observations are then likely to meet the assumption required by simple Kriging. Isakov et al. (2012) presented a similar approach, where they used a hybrid regional-local air quality model to improve the *LUR* technique.

The specifics steps to combine model estimates and observations using Kriging interpolation are as follows:

(1) Estimate concentrations at the monitoring stations using *LBM**, and calculate the residuals between model estimates and observations

(2) Estimate concentrations at all grids in the study domain using *LBM*

(3) Use Kriging to interpolate the residuals at all grids using residuals calculated in step (1).

(4) Add the estimated residuals from step (3) to model estimates from step (2).

**The method described here is not limited to LBM, and should apply to other dispersion models as well.*

By adding the estimated residuals to model estimates, the resulting concentration maps should better reflect the 'true' concentration map since it is calibrated by observations.

2.4 Comparison of Simple and Residual Kriging

In this section, we compare the performance of simple (*Observation only*) and residual Kriging (*Model+Observation*). There are several techniques for evaluating the performance of interpolation, the details of which are in EPA (2004). Here we used the most common technique, known as leave-one-out cross validation (LOOCV): the observation at a selected location is left out in the interpolation, and the interpolated value at this location is then compared with the actual observation. Figure 2-18 and Figure 2-19 compare the cross-validation of simple Kriging and residual Kriging. We see that residual Kriging improves the correlation between observed NO_x and NO_2 concentrations over simple Kriging. In the *SoCA*B, the correlation coefficient (r^2) increases from 0.06 to 0.42 and from 0.17 to 0.29 for NO_x and NO_2, respectively. We find a similar result for the *SJVAB* data: r^2 increases from 0.17 to 0.57 for NO_x, and from 0.16 to 0.45 for NO_2. Scatter between the observed and estimated concentrations also decreases as indicated by the smaller s_g (except for NO_2 in the *SoCAB*). These results suggest that *LBM* can successfully remove the underlying trend in data, and thus enhance interpolation methods, such as Kriging.

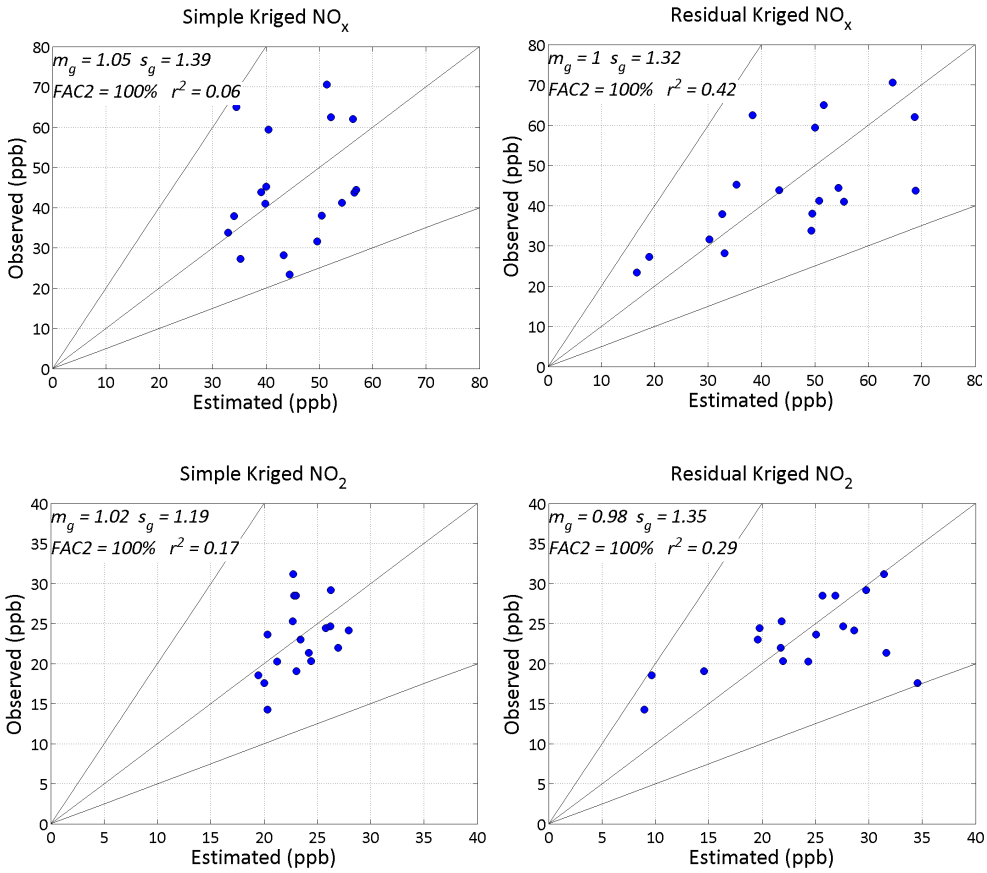

Figure 2-18: Cross-validation of Kriging interpolation in the *SoCAB*. Left panel: Simple Kriging of *NO_x* and *NO_2* concentrations. Right panel: Residual Kriging of *NO_x* and *NO_2* concentrations

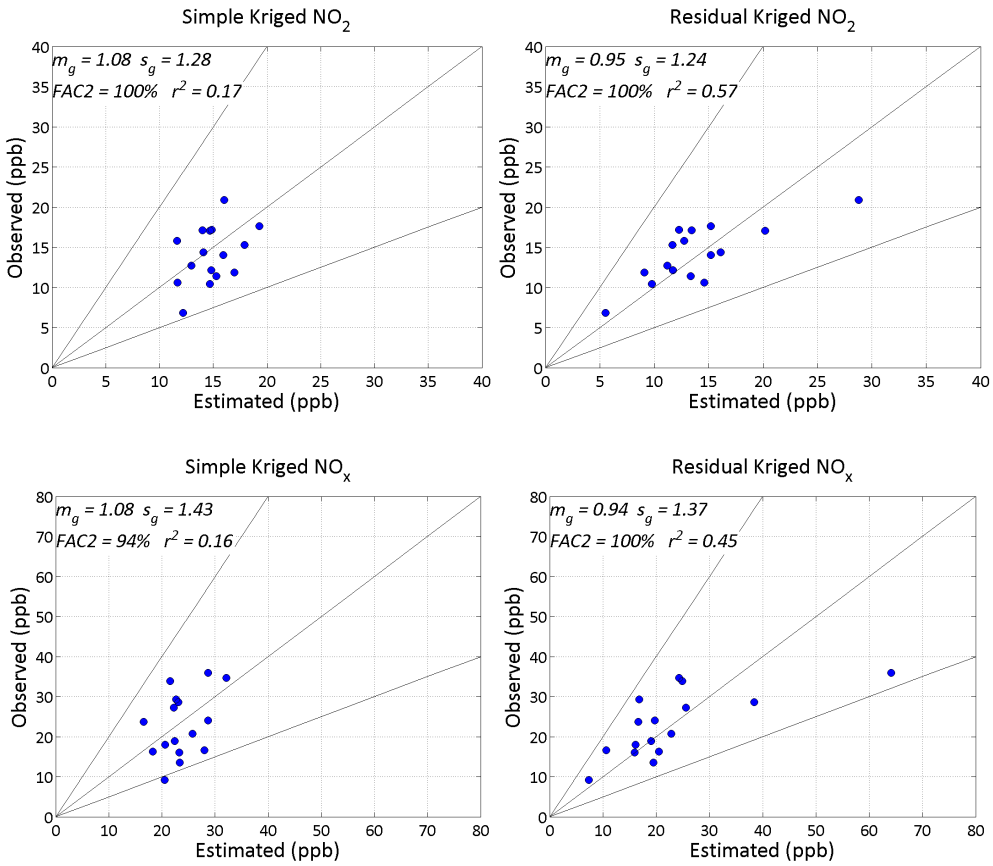

Figure 2-19: Cross-validation of Kriging interpolation in the *SJVAB*. Left panel: Simple Kriging of NO_x and NO_2 concentrations. Right panel: Residual Kriging of NO_x and NO_2 concentrations.

Figure 2-20 shows the 4-Day average NO_2 concentration map in the *SoCAB* using both simple (Observations only) and residual Kriging (Model+Observations) to interpolate the NO_2 concentrations at the 994 grid points. We see that residual Kriging predicts that the majority of the high NO_2 concentrations occur near major cities such as Los Angeles and Ontario, as well as the major roads. Simple Kriging shows reasonable spatial variations of NO_2 in the central region where most of the monitoring sites are located, but it fails to explain the spatial variation of NO_2 near the

major roads and in regions far from emission sources, such as the southeast corner and the central-north region, where limited numbers of observations are available. The results of residual Kriging are more reasonable because they show greater variation near emission sources such as major roads.

The difference in the *SJVAB* NO_2 concentration maps generated using simple Kriging and residual Kriging is even more pronounced, as shown in Figure 2-21. Residual Kriging produced a much more realistic concentration map than simple Kriging. In the Sierra-Nevada Mountain region, simple Kriging estimated a uniform 15 ppb of NO_2 concentrations when no emission sources are present. Residual Kriging suggests that high concentrations of NO_2 are all confined inside the valley, primarily in large cities and near major roads. In the mountain regions, residual Kriging suggests NO_2 concentrations are zero, as one would expect.

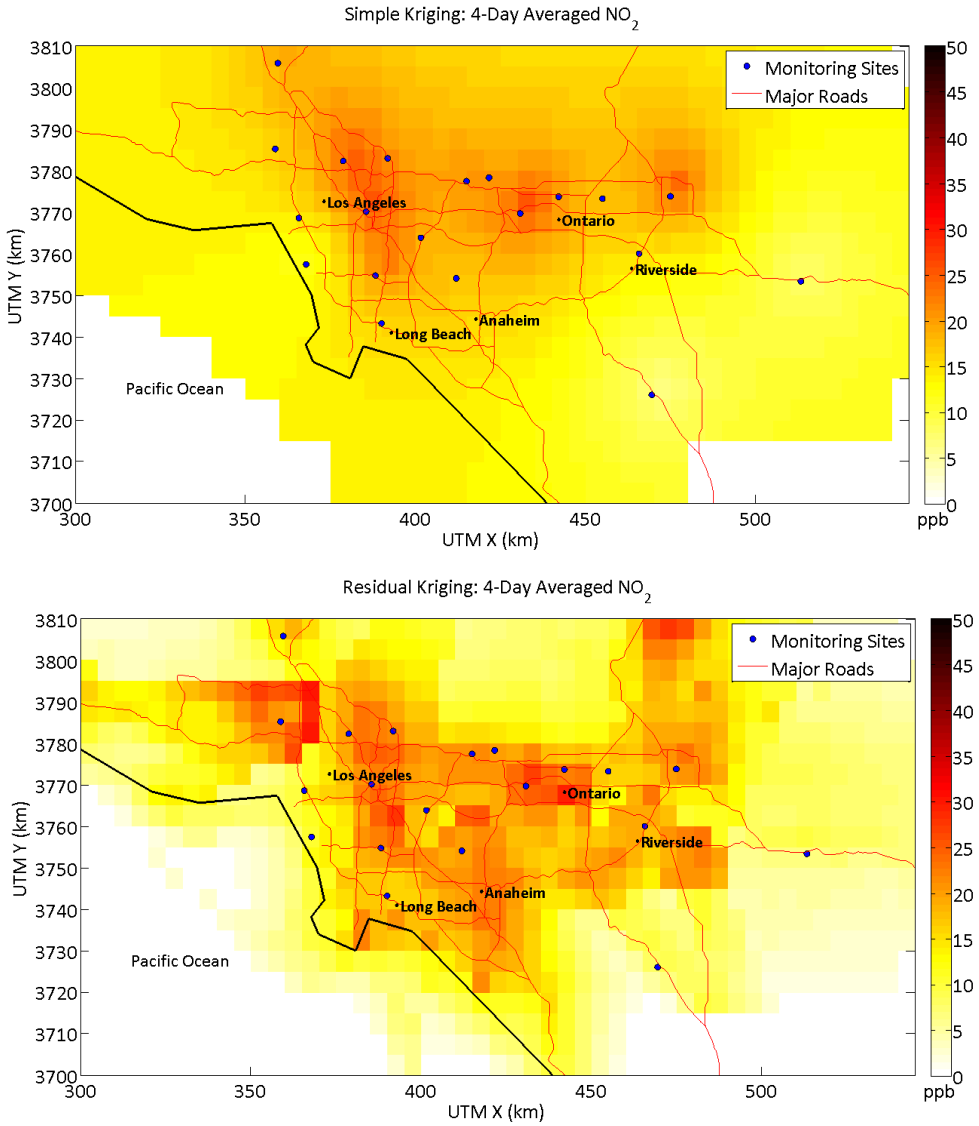

Figure 2-20: 4-Day average *NO_2* concentration map in the *SoCAB*. Upper panel: Interpolated using Simple Kriging (Observations Only). Lower panel: Interpolated using residual Kriging (Model+Observations). The blue dots indicate monitoring sites.

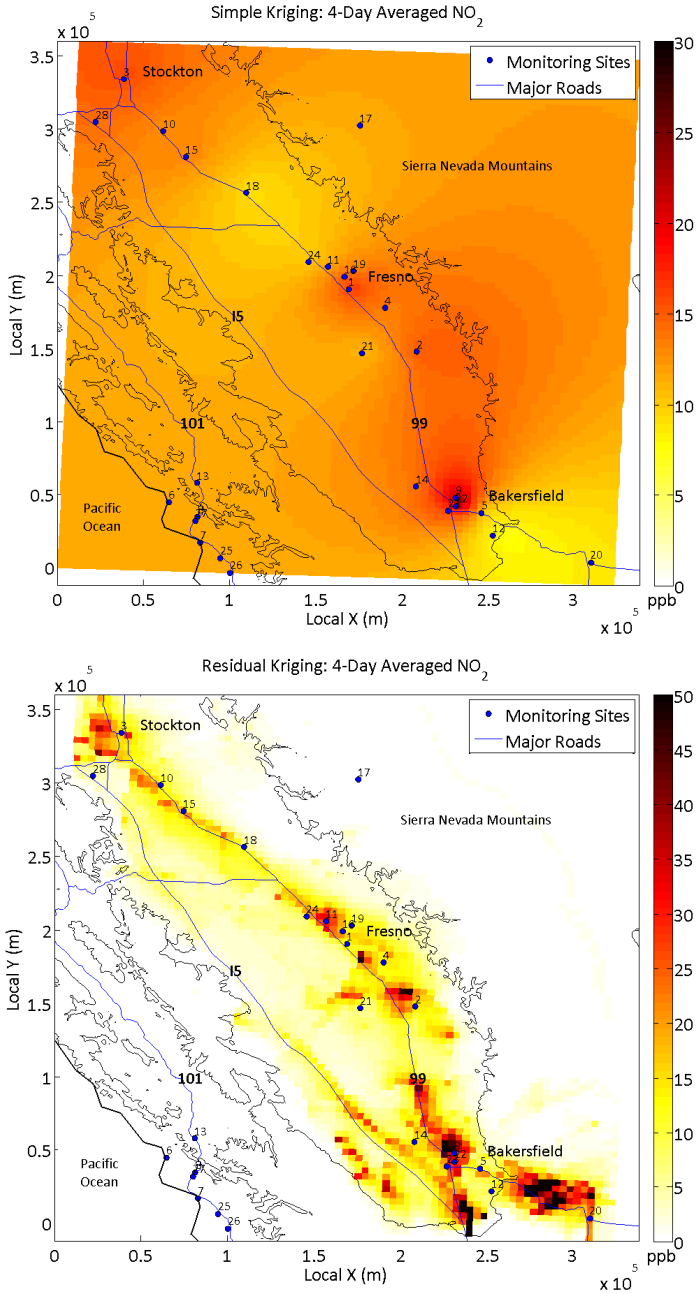

Figure 2-21: 4-Day average NO_2 concentration map in the *SJV*. Upper panel: Interpolated using Simple Kriging (Observations only). Lower panel: Interpolated using residual Kriging (Model+Observations). The blue dots indicate monitoring sites.

2.5 Summary and Conclusions

We have successfully used Kriging interpolation to combine model estimates and observation in both *SoCAB* and *SJVAB*; the resulting concentration maps provides more information than maps generated using only interpolated observations. The assumption of constant mean used in simple Kriging is satisfied by using dispersion models to remove the underlying trend. We have formulated a simple Lagrangian model that can be used to estimate "background" concentrations of NO_x, NO_2, and O_3 over spatial scales of a kilometer in a domain extending over hundreds of kilometers. The model achieves computational efficiency by separating transport and chemistry using the concept of species age. The model was also evaluated against measurements made in the *SJVAB* in 2005. Although the model shows slight under/overestimation of NO_x and NO_2 concentrations respectively, it provides a reasonable description of the temporal (daily and seasonal) as well as spatial variation of NO_2 and O_3 concentrations in the region.

LBM is computationally efficient and relatively easy to implement, which makes it an appropriate candidate for long-term exposure studies. We have also demonstrated the use of *LBM* to enhance interpolation of observations. Stein et al. (2007) and Isakov et al (2009) combined results from *CMAQ* with a short-range transport model such as *AERMOD* to assess personal exposure; similarly, results from *LBM* can also serve as inputs to a short-range dispersion model to estimate the impact of a source of

NO_x on NO_2 and ozone at a scale of tens of meters from the source. The model can provide hourly concentrations of these species over time periods of a year, which is required in human exposure studies.

3 ESTIMATING CONCENTRATIONS AT STREET SCALE

3.1 Introduction and Background

In chapter 2 we demonstrated how to construct more realistic concentration maps at urban scale by combining results from a long range transport model and observations at regional monitoring stations using Kriging interpolation. In this chapter we describe a street scale model that can be used to estimate concentration patterns within cities at scales of tens of meters. This model can be combined with the long range transport models, such as *LBM*, to construct high spatial resolution concentration maps in urban areas. The resulting concentration maps could be used to estimate exposure concentrations in Transit Oriented Developments (*TODs*). *TODs* are designed to promote walking, cycling, and public transportation to reduce motor vehicle emissions by increasing the density of people through the use of multi-story buildings. In principle, *TODs* should improve local air quality by reducing emissions associated with transportation, but the effect of these multi-story buildings on dispersion within the urban canopy is not yet known. It is very important to develop models to estimate exposure concentrations at street scale because high population density in *TODs* can result in a large population being exposed to high concentrations of traffic emissions.

To model dispersion in urban canopies, we first need to have a basic understanding of the flow field within an urban canopy, which is extremely complex.

Results of *CFD* simulations, such as shown in Figure 3-1, indicate that individual buildings have significant effects on the flow pattern. It is very difficult to model all the features of the flow that can affect dispersion, but we can develop simple semi-empirical models that capture the essential effect of the urban environment on concentrations.

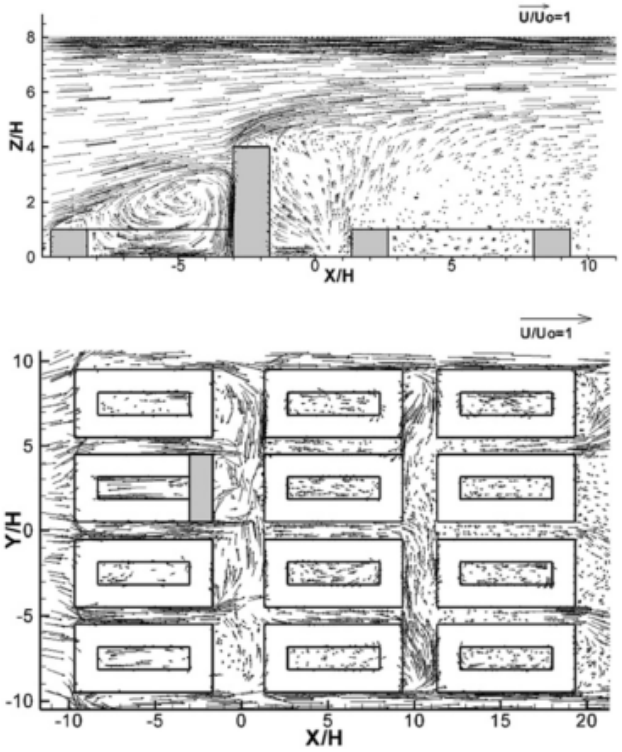

Figure 3-1*CFD* simulation of the flow field around an isolated tall building (adapted from Heist et al., 2009)

Oke (1988) characterized three flow regimes in street canyons depending on the street aspect ratio, defined as the ratio of average building height *H*, to street width *W*. The classes of flow, shown in Figure 3-2, are: (1) *Isolated roughness flow*: the space between buildings is large enough that the flow is readjusted before encountering the

next obstacle. (2) *Wake interference flow:* (*H*/*W*≈0.5) there is not sufficient space between each building for the flow to fully readjust before encountering the next obstacle. (3) *Skimming flow*: (*H/W≈1*) the space between the buildings is small enough that the synoptic flow skims over the street canyon, resulting in the formation of vortex flow within the street canyon (Oke, 1988). A field measurement conducted by DePaul and Sheih indicates formation of vortex flow within the canyon if the rooftop winds exceed 1.5~2 m/s (DePaul and Sheih, 1986).

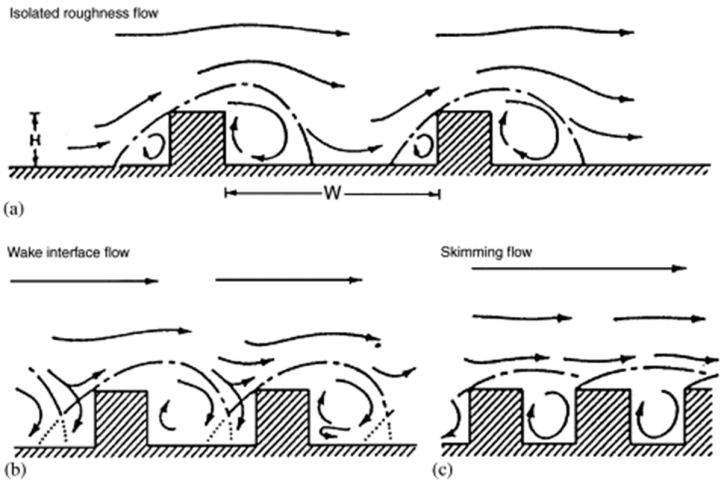

Figure 3-2 Flow regimes at different H/W ratios. (Adapted from Oke, 1988)

As shown in Figure 3-3, the vortex results in the street level wind being in opposite direction of the rooftop wind, thus causing higher concentrations in the leeward side of the street than on the windward side. This vortex flow forms the basis of many existing urban canopy dispersion models, such as the Canyon Plume-Box Model (*CPBM*) and the Operational Street Pollution Model (*OSPM*).

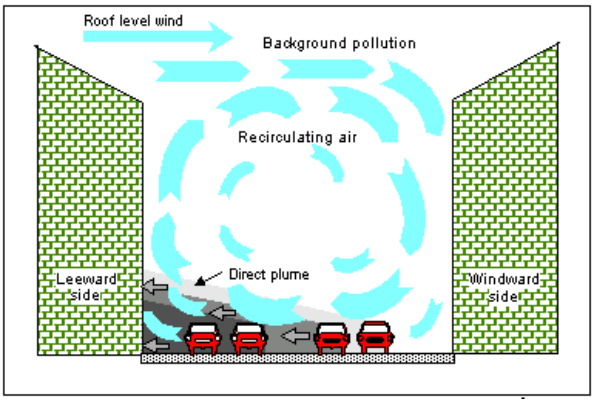

Figure 3-3 Vortex formation within the street canyon. (adapted from Hertel and Berkowicz, 1989)

The *STREET* model is one of the early approaches to modeling dispersion in street canyons (Johnson et al, 1973). This model assumes the total concentration at street level is the combination of a background concentration that is transported down to the street from roof level and the contribution from local traffic emissions. The concentration of local emissions is modeled using a box model, where the within canyon horizontal wind speed transports pollutants from the street. The limitations of the *STREET* model formulation include: (1) it cannot reflect the impact of changes in wind direction, and (2) it is not applicable under calm-wind conditions.

The Canyon Plume-Box Model (*CPBM*), developed by Yamartino and Wiegand (1986), is another approach to estimate concentration in a street canyon. *CPBM* calculates street level concentrations by considering a direct contribution from the local traffic and a recirculating contribution due to the vortex flow formed within the street canyon. The evaluation of *CPBM* against the Bonner Strasse experiment data show significant improvement over the *STREET* model.

The *CAR* (Calculation of Air pollution from Road traffic) model is developed primarily using wind tunnel experiment data. This model works by classifying the street based on several predetermined classes. Annual average concentrations are then estimated through an empirical model dependent on the street class and the distance between the receptor and street axis (Eerens et al, 1993).

The Operational Street Pollution Model (*OSPM*), developed by the National Environmental Research Institute of Denmark, is widely used to estimate concentrations due to traffic in street canyons (Hertel & Berkowicz, 1989). Similar to *CPBM*, the total street level concentration is divided into direct and recirculation contribution in *OSPM*. Due to the formation of vortex flow, wind direction at street level is opposite of the rooftop wind direction, causing the concentration at the leeward side to be higher that the concentration at the windward side.

The 'Street Box' model developed by Mensink & Lewyckyj (2001) is a 2-D box model based on the balance of vertical diffusion flux, horizontal convective flux, and emission due to local traffic. Different from *CPBM* and *OSPM*, the Street Box model does not specifically account for the effect of recirculation; rather, it treats the rooftop shear flow as the driving force (Mensink and Lewyckyj, 2001).

Computational Fluid Dynamics (*CFD*) (Hang et al., 2012a) has also been used to investigate dispersion in street canyons recently, and can provide insightful information on the mechanism governing dispersion in street canyons. Yuan and Ng

used the k-ε model to simulate the flow around buildings and study the effect of different building morphologies on natural ventilation in urban areas (Yuan and Ng, 2012). We don't discuss *CFD* because we focus on developing simple semi-empirical models to estimate concentrations.

Many field studies have been conducted to examine micrometeorology in urban canopies. Klein and Galvez conducted a yearlong measurement of micrometeorology in a street canyon between 2009 and 2010. Their measurements show that the street level wind speeds best scale with rooftop friction velocity, u_*, but there is no single velocity scale that allows us to scale both the mean flow and turbulence (Klein and Galvez, 2014). Hanna et al (Hanna et al, 2007) made micro-meteorology measurement in Oklahoma City and Manhattan's Madison Square Garden in 2003 and 2005 respectively. Their measurements show that the scalar wind speed measured at the urban rooftop (~100-200m above ground level) is similar to the surface wind speed measured at nearby airports. The urban street level wind speed is approximately 1/3 of the corresponding rooftop wind speed (Hanna et al., 2007).

As mentioned before, many of the existing models are based on the vortex flow formed in a street canyon configuration, and they have primarily been evaluated with data in European cities, where street canyons are common. The building height is inhomogeneous in most of the cities in the United States, which leads us to question the applicability of these models to US cities. Hang et al (2012b) have studied the

influence of building height variability on pollutant dispersion using *CFD*, but the analysis is limited to clusters of buildings with similar characteristics, which does not represent a real urban environment. No quantitative relationship between building height variability and pollutant concentrations within the urban canopy was provided. Thus, our objective is to formulate a dispersion model that can be applied to estimate pollutant concentrations in streets with non-uniform building height. Our objective is limited to capturing the essential features of dispersion in the presence of buildings through a semi-empirical dispersion model. This model cannot describe the variation of concentration across the street as *OSPM* does. Its output is concentration averaged over the area of a city block.

3.2 The Vertical Dispersion Model

This section describes a dispersion model that describes concentrations in urban areas with variable building height. The model is based on the results of analysis of data collected in Göttinger Straße. During 2003 to 2007, a 5-year measurement campaign of micrometeorology and NO_x concentrations on Göttinger Straße, Hannover, Germany was conducted by the Lower Saxony Ministry for Environment, Energy, and Climate. Göttinger Straße is approximately 25 m wide, with 20 m tall buildings on either side (Figure 3-4).

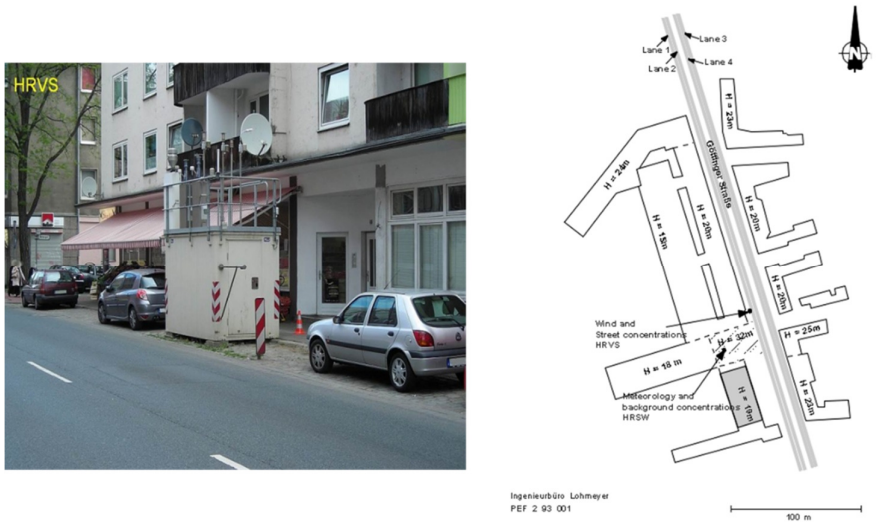

Figure 3-4 Göttinger Straße, Hanover, Germany (photo and schematic are provided by the Lower Saxony Ministry for Environment, Energy, and Climate)

NO and NO_2 concentrations were measured at 1.5 m above ground level and on a building rooftop 32 m above ground level. Micrometeorology measurements, including wind speed and turbulence, were made on a tower in the street at 10 m above ground level and above the nearby rooftops at 42 m above ground level. Traffic flow measurements were made with automatic counters, which were converted into emission rates using emission factors. Schulte (2014, *submitted*) has evaluated several models with the data collected from Göttinger Straße, and concluded that the model described by equation (3-1) provides the best description of the concentrations of NO_x as shown in Figure 3-5.

$$C_s = \alpha \frac{Q}{W\sigma_w} + C_r \qquad \textbf{(3-1)}$$

where C_s is the near surface concentration, C_r is the roof concentration, Q is the emission per unit length of the road, W is the width of the road, and σ_w is the standard deviation of the vertical velocity fluctuations at 10 m. The constant α is empirically determined to be 0.8.

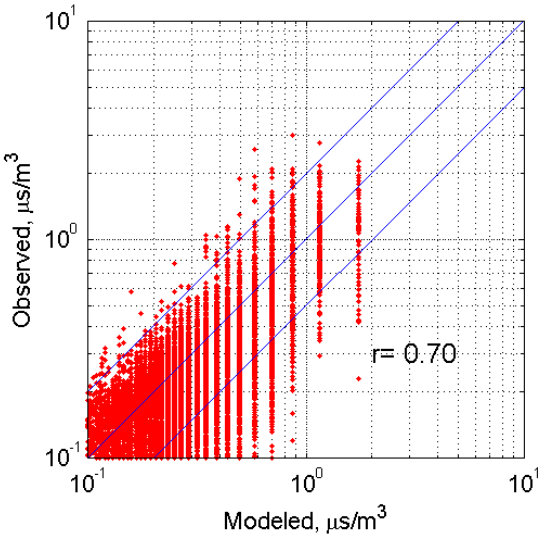

Figure 3-5 Model estimates compared with observations of NO_x/Q made during 2003 (Adapted from Schulte et al, 2014, *submitted*)

The good correlation between the vertical concentration differences and $1/\sigma_w$ served as the foundation for the development of the *Vertical Dispersion Model* (*VDM*), which assumes that the vertical transport is the dominate mechanism that governs dispersion in urban areas. A schematic of the *VDM* is shown in Figure 3-6.

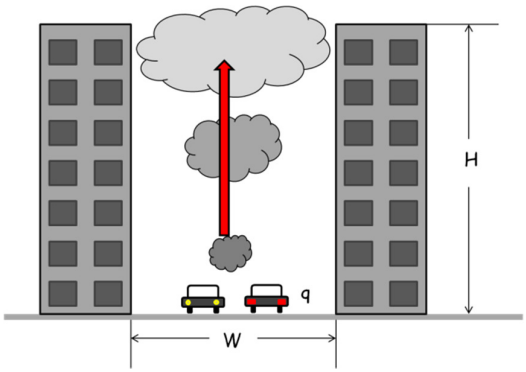

Figure 3-6 Schematic of the *VDM* formulation

Vertical diffusion can be described by the following equation,

$$\frac{Q}{W} = K\frac{dC}{dz} \tag{3-2}$$

where Q is emission rate per unit length of road, and K is the eddy diffusivity for momentum. Assuming the vertical concentration profile within the urban canopy is linear, and K can be expressed as $K=\sigma_w l$, where σ_w is the within-canyon average of the standard deviation of the vertical turbulent velocity fluctuations, and l is a mixing length, equation (3-2) can be rewritten as

$$\frac{Q}{W} = \sigma_w l\frac{C_s - C_r}{H} \tag{3-3}$$

The mixing length is calculated as

$$l = \beta\left(\frac{HW}{H+W} + h_o\right) \tag{3-4}$$

where β is an empirical constant, and h_o is the initial plume spread associated with the size of the source. Substituting equation (3-4) into equation (3-3) results in the

following expression for surface level concentrations

$$C_s = C_r + \frac{Q}{\beta W \sigma_w} \frac{H(1+a_r)}{H + h_o(1+a_r)} \quad \textbf{(3-5)}$$

where C_s is the surface level concentration, C_r is the rooftop concentration, σ_w is the vertical turbulent velocity fluctuation, a_r is the aspect ratio, *H/W*, where *H* is the equivalent building height, and *W* is the width of the street. The equivalent building height is defined as

$$H = \frac{1}{L}\sum_i H_i w_i \quad \textbf{(3-6)}$$

where *L* is the length of the street, and H_i and w_i are the height and width of building *i*.

Table 3-1 Equivalent building height at all the measurement locations. Only buildings on the same block as the receptor are included in the calculation.

Location	*Area Weighted Building Height*			*Street Width*	*Aspect Ratio*
	South/West	*North/East*	*Average*		
8th Parking Lot	*0*	*0*	*0*	*20*	*0*
8th Building II	*48.90*	*37.60*	*43.25*	*20.00*	*2.16*
8th Building I	*30.40*	*38.70*	*34.55*	*20.00*	*1.73*
Broadway	*36.80*	*35.00*	*35.90*	*26.00*	*1.38*
7th St	*38.60*	*53.00*	*45.80*	*25.00*	*1.83*
Temple City	*6.00*	*6.00*	*6.00*	*30.00*	*0.20*

*Note: Building morphology information was downloaded from the 'Los Angeles County GIS Data Portal' (*http://egis3.lacounty.gov/dataportal/2011/04/28/countywide-building-outlines/).

The *VDM* indicates the importance of aspect ratio in determining transport of pollutants in urban canopies, which is consistent with the finding by Barlow and

Belcher (2002). Barlow and Belcher used the naphthalene sublimation technique to study the ventilation characteristics of a street canyon and conclude that the aspect ratio is the most important dimensionless parameter controlling the ventilation efficiency of a street canyon.

3.3 Field Measurements

We designed field measurements to provide data to evaluate the vertical dispersion model (*VDM)*. The objectives of the field study are to: (1) identify the primary mechanism that governs surface concentrations at street scale in urban areas with inhomogeneous building heights, and (2) investigate how the built environment modifies the upwind rural flow so that we can develop models to estimate turbulence in urban areas. To do so, we made measurements of micrometeorology and particle number concentration of ultrafine particles at locations with different building morphologies. The study locations are: 1) 8th street of downtown Los Angeles, California, 2) on 7th street of downtown Los Angeles, and 3) Near the intersection of Temple City Blvd and Las Tunas Dr. in Temple City, California. Both the 7th St. and 8th St. sites have an average building height of roughly 40m, while the average building height of the Temple City site is 6m.

We measured particle number concentrations (*PNC*) of ultrafine particles (*UFP*), those particles with aerodynamic diameter smaller than 100 nm, because *UFP* causes negative health effects. When inhaled, larger particles with diameter greater than 10

μm (PM_{10}) are trapped in the hair in the lung, but smaller particles go deeper in the lung and into the bloodstream. People suffering from asthma and other cardiovascular diseases are especially sensitive to *UFP* (Health Effects Institute, 2013). We use TSI Model 3022A Condensation Particle Counters (*CPC*), which are capable of measuring *UFP* concentrations up to 10^7 particles/cm^3 at a sampling rate of 1 Hz. The *CPCs* have a 50% detection cutoff of 7 nm.

Measurements of micrometeorology at street level in an urban canopy are usually not available. Thus, in addition to a dispersion model that relates the urban micrometeorology with concentrations, we need models that allow us to estimate the urban micrometeorological parameters from micrometeorological data collected at an upwind rural location, such as that routinely collected at airports. Micrometeorology measurements were made using Campbell Scientific *CSAT3* 3-D sonic anemometers, which measure wind speed in 3 directions at 10Hz. We measured micrometeorology at an upwind rural location, on the rooftop of an urban area, and at urban surface level simultaneously to examine the evolution of turbulence and the effect of buildings on local micrometeorology. The sonic anemometer data was processed to yield turbulence and mean wind data as described in the appendix.

We estimated traffic emissions using the concept of Emission Factor: *Emission Rate = Traffic Count×Emission Factor*. Traffic data were obtained from the automatic traffic counter managed by LA County, and from manual traffic counts from video

recordings of local traffic. In the following sections, we give detailed descriptions of the field measurements.

3.3.1 Downtown Los Angeles -8th Street

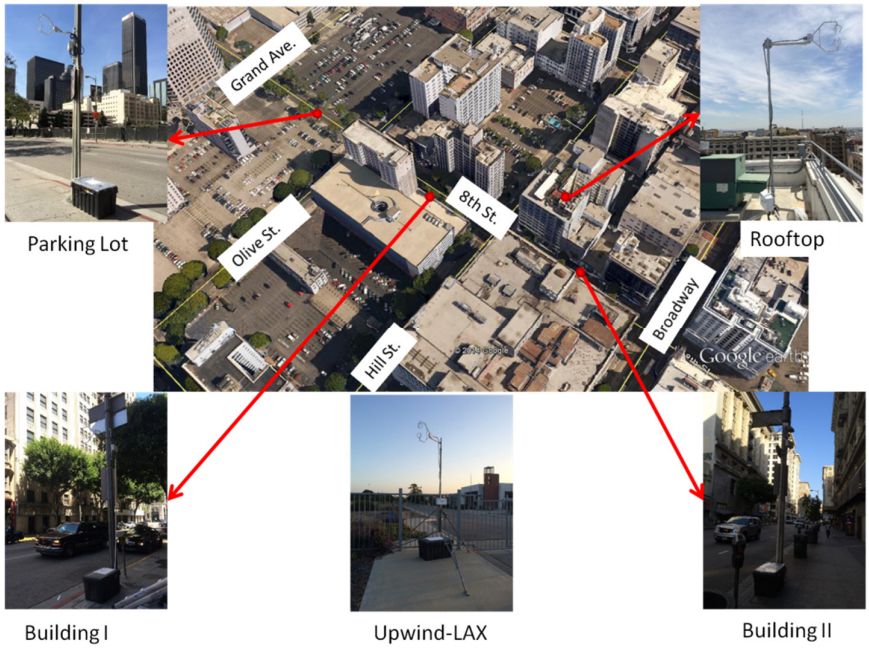

Figure 3-7 Locations of the sonic anemometers during the *DTLA* 8th St. measurements. Three sonic anemometers were placed on the street level, 1 sonic anemometer on the rooftop of a 55m tall building, and 1 sonic anemometer is placed at an upwind rural area near the Los Angeles International Airport (*LAX*).

Between May 7 and May 13th, 2014, five *CSAT3* 3-D sonic anomometers were installed to measure local micrometeorology at five different locations simultaneously. As shown in Figure 3-7, 3 sonic anemometers were installed at street level on 8th street of downtown Los Angeles (*DTLA*), California. This location was chosen because 3 sections of 8th St. have different average building height and different building height variability, thus allowing us to isolate the effect of building

height and height variability on the local micrometeorology since the three locations have the same upwind conditions.

The first street level sonic anemometer was placed between Olive St. and Grand Ave, where there is a large parking lot on both sides of 8th street; we refer to this region as the *Parking Lot* region. The second anemometer was placed between Olive St. and Hill St, where there are buildings with heights ranging from 20m to 50m on both side of 8th street; this section is refered as the *Building I* region. The third sonic anemometer is placed in the *Building II* region, between Hill st. and Broadway. Similar to the *Building I* region, there are buildings on both side of the street, but the building heights at this section of 8th st are relatively uniform.

In addition to the 3 street level sonic anemometers, one sonic anemometer was placed on the rooftop of a 50m tall building located in the *Building II* region. The 5th sonic anemometer was placed near the Los Angeles International Airport (*LAX*), which is about 10 miles (~17 km) upwind of *DTLA*. The upwind measurement serves as a reference, which allows us to examine the evoluation of turbulence from rural areas to urban areas.

Concentration measurements were made at the *Parking Lot* and *Building II* regions simultaneously. This design helps remove variability due to emissions because the traffic is roughly the same at both locations, allowing us to directly compare the surface concentrations.

Figure 3-8 Sonic anemometer setup at 8th St. The sonic transducer head and electronics box are mounted on the city post at a height of approximately 4 meters. The data logger and the battery used to power all the electronics are locked inside a box on the ground.

The surface level sonic anemometers are mounted on city light posts to allow long time measurements. The complete setup in shown in Figure 3-8; the sonic transducer head is mounted at approximately 4m above ground level (*AGL*) for safety considerations. The data logger and the car battery used to power all the instruments are locked inside a box on the ground. All wires connecting the sonic electronics box to the data logger are secured inside a *PVC* pipe. A sand bag is added in the box as weight to prevent the box from tipping over easily.

The rooftop and *LAX* sonic anemometers are mounted on a tripod of 2.4 and 3 meters, respectively. The measurement heights are listed in Table 3-2

Table 3-2 Micrometeorology measurement heights at the 5 locations

Location	*LAX*	*Rooftop*	*Parking Lot*	*Building I*	*Building II*
Measurement Height (m) (AGL)	*3*	*52.4**	*4*	*4*	*4*

*The sonic anemometer is mounted on a 2.4 m tripod that is placed on the rooftop of a 50m tall building.

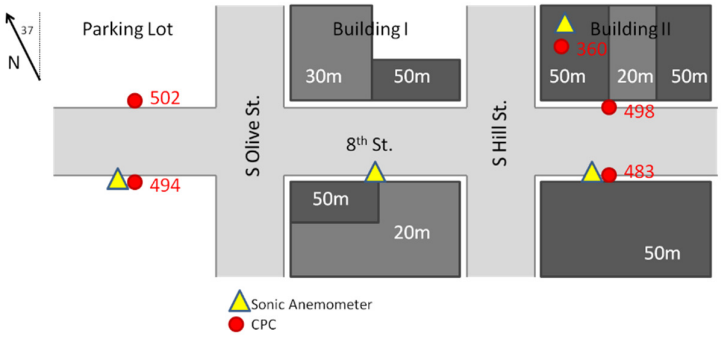

Figure 3-9: *CPC*s locations during the *DTLA*-8th St field measurements.

On May 7th and 9th, 2014, we made measurements of *UFP* concentrations at the locations shown in Figure 3-9. A pair of *CPCs* was placed in the *Parking Lot* and *Building II* regions, and one *CPC* was placed on the rooftop (Rooftop measurement was only made on the 9th).

The *CPCs* are designed for indoor use: they require 110V outlets and cannot be easily setup for our outdoor field measurements. Thus, we designed and constructed a cart that powers the *CPC* from a battery and allows the *CPC* to be more mobile and easier to setup outdoors. The complete *CPC* setup is shown in Figure 3-10. As shown, the *CPC* is secured on the top of the cart, and a car battery is housed in the lower

compartment of the cart. An inverter converts the 12 V DC battery voltage to 110 V AC. On a full charge, the car battery can power the *CPC* for approximately 10 hrs.

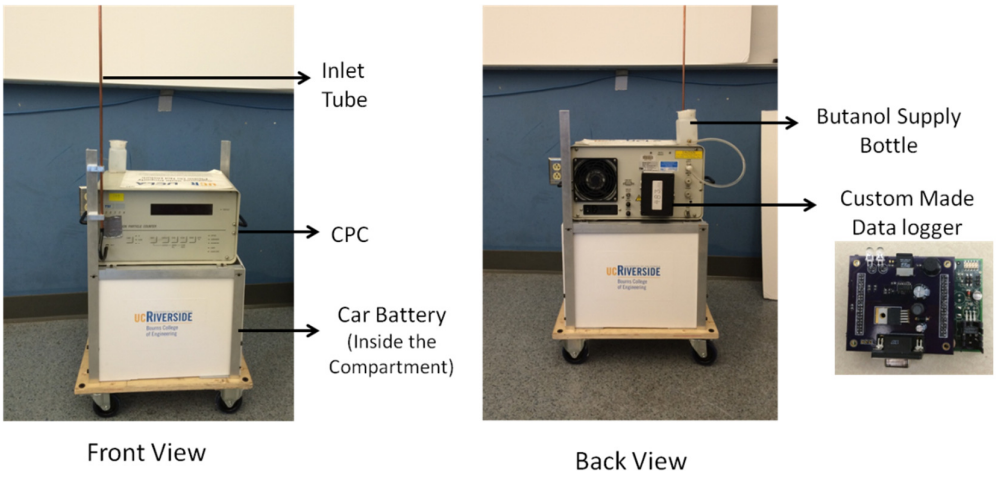

Figure 3-10: The complete *CPC* setup. The *CPC* is secured on top of the cart, while the car battery is housed inside the lower compartment.

3.3.2 Downtown Los Angeles-7th Street

On September 20th, 2013, we conducted a field measurement near the intersection of 7th St. and Broadway in downtown LA. Broadway is oriented approximately 37° from the north-south direction as shown in Figure 3-11. The average building height on 7th St and Broadway is 40m. Three *CSAT3* sonic anemometers and one Gill instruments R2 sonic anemometer were used to measure micrometeorology at various locations simultaneously: one on the rooftop of a 55m building next to 7th St, one on Broadway, one on 7th St, and one at the *Rancho Cienega Recreation Center*, which is approximately 14 km west of *DTLA*. The locations of the 3 urban area sonic anemometers are shown in Figure 3-11, and the measurement heights are listed in

Table 3-3. All surface level sonic anemometers were mounted on 2.4 m tall tripods. The locations of the concentration measurement are depicted in Figure 3-12. A pair of *CPCs* is placed on Broadway, one on each side of the street, one *CPC* is placed on the rooftop of the 55m tall building, and a pair of DiSCminis, portable sensors designed by *Matter Aerosol* capable of measuring particle number concentrations and average particle diameters, is placed on 7th St., one on each side of the street.

Traffic was recorded at the intersection using cameras and manually counted. Traffic data was also obtained from the city of LA automatic traffic monitoring system.

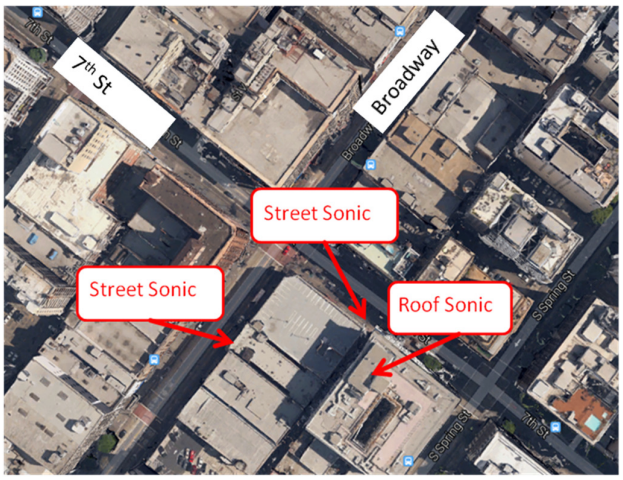

Figure 3-11 Location of the micrometeoroogial measurements

Table 3-3 Micrometeorology measurement height of the 7th/Broadway Study

Location	*Upwind*	*Rooftop*	*Broadway*	*7th St*
Measurement Height (m)	*3*	*57.4**	*2.4*	*2.4*

*The sonic anemometer is mounted on a 2.4 m tripod that is placed on the rooftop of a 55m tall building.

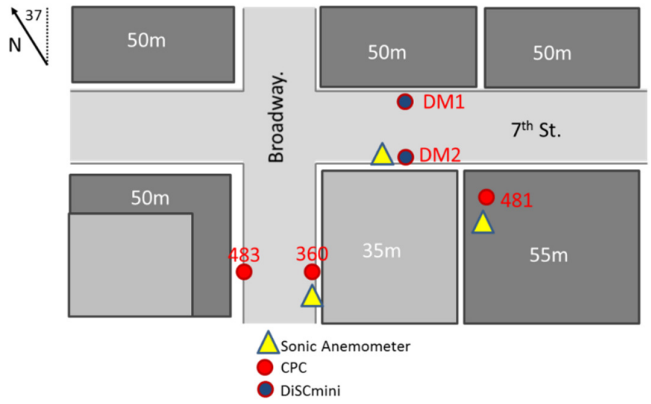

Figure 3-12: *CPCs* placements during the *DTLA*-7th St field measurement.

3.3.3 Temple City-Las Tunas Dr.

The Temple City field measurements were conducted near the intersection of Las Tunas Dr. and Temple City Blvd, in the City of Temple City between Jan 13th and Feb 13th, 2014. The Temple City site has very a different building morphology than the *DTLA* sites. All the buildings are 1-story (~6m tall) and the street is wide (Las Tunas Dr. is roughly 30m wide), resulting in an aspect ratio (*H/W*) of 0.2, whereas the aspect ratio of the *Building II* region of 8th St. is about 2. The upwind rural sonic anemometer was installed at Ascot Hills Park, which is located about 10 miles (16km) southwest of the Temple City site. Rooftop sonic anemometers were placed on the rooftop of the HSBC bank located at the intersection of Las Tunas Dr. and Temple City Blvd, as shown in Figure 3-13. The measurement heights of all three sonic anemometers are listed in Table 3-4. The street level sonic anemometer was mounted on a city light post at a height of 3m AGL. Unfortunately, the sonic anemometer installed at the upwind site malfunctioned during nighttime, causing all the nighttime measurements

to be invalid.

As shown in Figure 3-14, we have used 6 *CPCs* to measure surface concentrations, and 1 *CPC* to measure rooftop concentrations. Concentration measurements were made on January 15th. 16th, and 17th, 2014.

Figure 3-13 Sonic Anemometers location of the Temple City measurement; averaging building height is 6m. 1 sonic were placed on the street level, 1 sonic on the roof of a 6m tall building, and 1 sonic at an upwind park located roughly 10 miles southwest of the urban site.

Table 3-4 Micrometeorology measurement heights of the Temple City Study

Location	*Upwind*	*Rooftop*	*Las Tunas Dr.*
Measurement Height AGL (m)	*3*	*8.4**	*3*

*The sonic anemometer is mounted on a 2.4 m tripod that is placed on the rooftop of a 6m tall building.

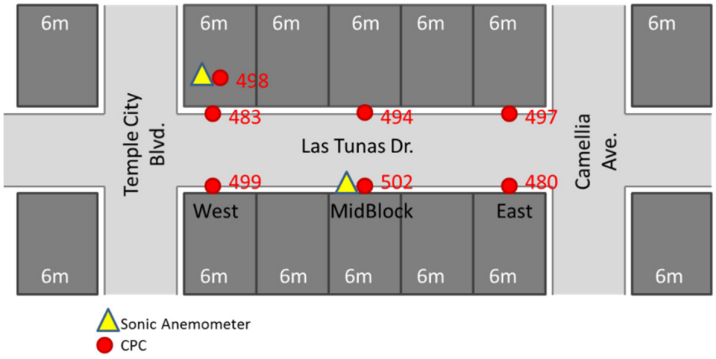

Figure 3-14: Locations of the *CPCs* on Las Tunas Dr., Temple City.

3.4 Observed Concentrations

This section provides an overview of the concentrations measured at all the field sites. All the following analyses were done with 30-minute averaged concentrations. Surface concentrations are the average of the concentrations on both sides of the street. The total concentrations measured at the surface and rooftop, and the vertical concentration differences, ΔPNC, at all sites are listed in Table 3-5.

Table 3-5 Daily average concentrations measured at all sites

Site	*Date*	*Location*	*Total PNC ($\times 10^4$ Particles/cm^3)*	*Rooftop PNC ($\times 10^4$ Particles/cm^3)*	*ΔPNC* ($\times 10^4$ Particles/cm^3)*	*ΔPNC/ Street PNC (%)*
8th St	*May 7th*	*Parking Lot*	*3.59*	*3.07*	*0.52*	*13.9*
		Building II	*4.15*	*3.07*	*1.08*	*26.2*
	May 9th	*Parking Lot*	*2.68*	--	--	--
		Building II	*3.81*	--	--	--
7th	*Sep 20th*	*7th St*	*3.5*	*1.6*	*1.9*	*54*
		Broadway	*3.2*	*1.6*	*1.6*	*49*
Temple City	*Jan 15th*	*Las Tunas*	*2.89*	*2.24*	*0.65*	*21.5*
	Jan 16th	*Las Tunas*	*5.18*	*5.05*	*0.13*	*1.3*
	Jan 17th	*Las Tunas*	*3.53*	*2.23*	*0.78*	*24.9*

*ΔPNC = *Street PNC-Rooftop PNC*

Figure 3-15 compares the concentrations measured at the *Building II*, *Parking Lot*, and Rooftop of 8th St. Concentrations are the lowest on the roof, and highest in the *Building II* region. Since *Parking Lot* and *Building II* are on the same street and only separated by one block, we assume the local traffic emission rates are the same (see section 3.3.1). Thus it is likely that the higher concentrations measured in the *Building II* region are due to the presence of buildings.

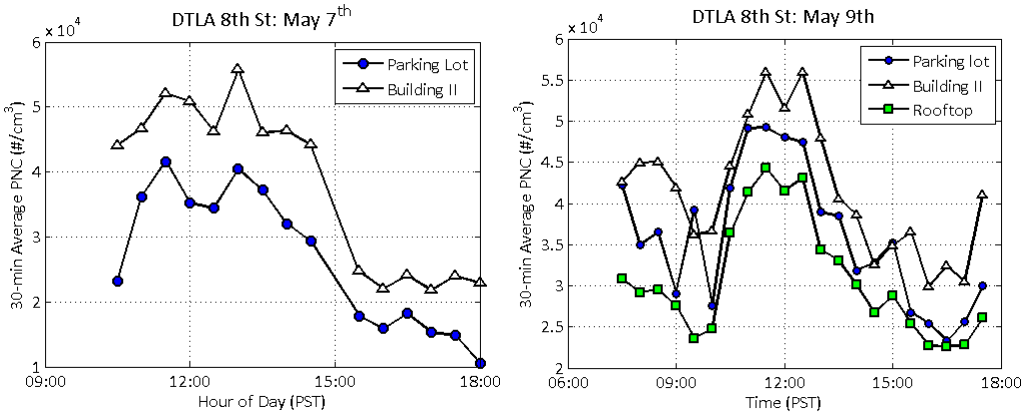

Figure 3-15 Daily variation of the 30-min average total *PNC*. Left Panel May 7th. Right Panel: May 9th. Concentrations at the two street levels are averaged over the 2 receptors that are placed across the street at each location.

Assuming the background concentrations on the rooftop and surface are the same, the vertical concentration difference represents the local contribution. As shown in Table 3-5, the average vertical concentration difference in the *Building II* region is double that in the *Parking Lot*, which suggests that buildings increase local surface concentrations. The local contribution is roughly 14% and 26% of the total concentration in the *Parking Lot* and *Building II* regions, respectively.

The temporal variation of the concentrations measured in Temple City is shown Figure 3-16. The total concentrations are much higher on the 16th and 17th than the 15th because a wild fire occurred on the 16th near Temple City, resulting in large background concentrations. On the 15th and 17th, ΔPNC is approximately 22% and 25% of the total surface level concentration, respectively, but on the 16th, ΔPNC is only 1.3% of the total concentration due to the large background; interestingly, ΔPNC is also smaller on the 16th than the 15th and 17th (0.13 versus 0.65 and 0.78 $\times 10^4$ Particles/cm^3). The smaller ΔPNC on the 16th is likely due to the fact that the vertical concentration difference decreases over the time of day, and the measurement on the 16th was conducted in the afternoon. The order of magnitude of the vertical concentration differences in Temple City is similar to that of the *Parking Lot* on 8th St, which suggests that the dispersion mechanism in streets with short buildings is similar to that of an open area.

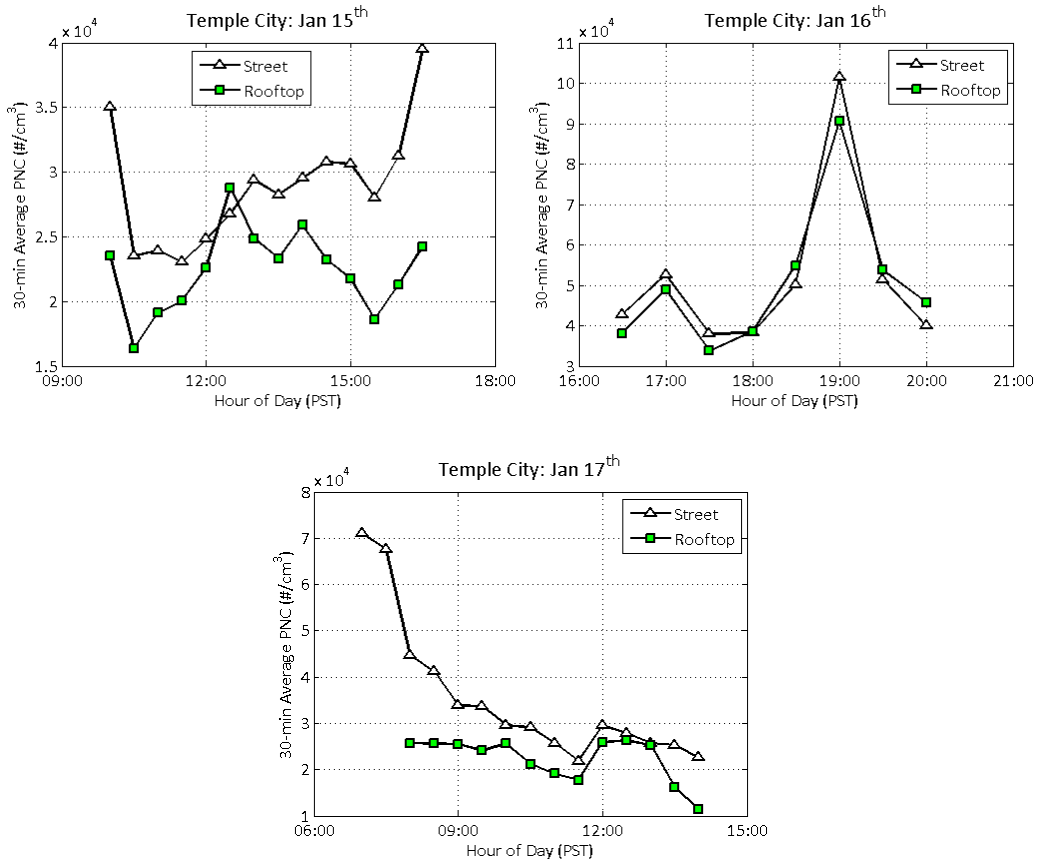

Figure 3-16 Daily variation of the 30-min average total *PNC*. Surface concentrations are averaged over all 6 street level *CPCs*.

The total concentration measured on 7th St. and Broadway of *DTLA* is shown in Figure 3-17 . The total *PNC* on the surface is much higher than the rooftop, and the local contribution is roughly 50% of the total concentrations on both 7th St and Broadway as indicated in Table 3-5.

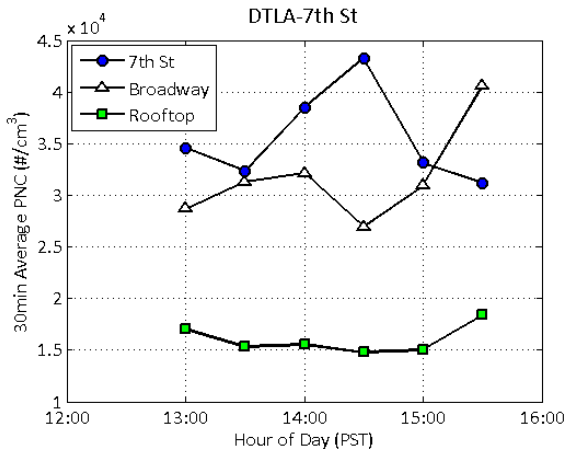

Figure 3-17 Daily variation of the 30-min average total PNC on 7th St and Broadway.

3.5 Evaluation of the Vertical Dispersion Model

We applied the *VDM* to concentration data collected on 8th Street of *DTLA*. Figure 3-18 shows the evaluation of the *VDM* against the observed vertical concentration differences. The background concentration can be assumed to be the same at the surface and roof, so the vertical concentration difference removes the background. In the left panel, emissions are estimated using the 30 minute average total traffic count and an emission factor of 10^{14} *Particles/km*/vehicle. As shown, *VDM* can only explain 27% of the variation in the observed ΔPNC. Interestingly, when we use the daily average traffic count to calculate the emissions, that is, when we remove the temporal variation of the emissions, the correlation between the model estimates and observation is improved (r^2 increased from 0.27 to 0.49) as shown in the right panel of Figure 3-18. In both cases, the model underestimated the vertical concentration difference, but this depends on the choice of emission factor, which is

highly uncertain. The better correlation obtained without the traffic variation is an indication of the uncertainties in relating particle emissions to traffic count through a constant emission factor.

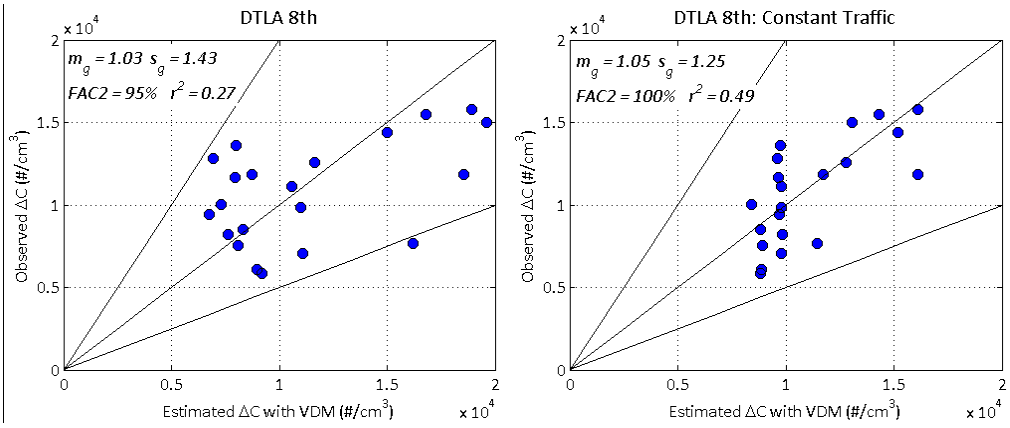

Figure 3-18 Observed vertical concentration difference, Δ*PNC*, versus *VDM* estimated Δ*PNC*. Left Panel: Emissions are estimated using 30min total traffic count: Right Panel: Emission is estimated using the daily average 30min traffic count.

Evaluation of *VDM* using data collected in Temple City is less satisfactory, as shown in Figure 3-19. There is no correlation between the *VDM* estimated and observed vertical concentration difference. *VDM* overestimated the vertical concentration difference by more than factor of 2 with the assumed emission factor of 10^{14} *particles/km/vehicle*, which again is related to the large variability in the emission factor of *UFP*.

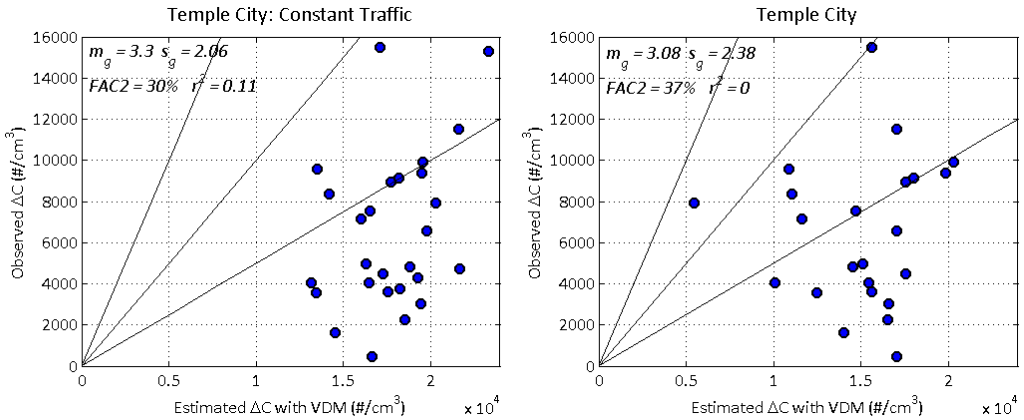

Figure 3-19 Observed vertical concentration difference, Δ*PNC*, versus *VDM* estimated Δ*PNC*. Left Panel: Emissions are estimated using 30min total traffic count: Right Panel: Emission is estimated using the daily average 30min traffic count.

3.5.1 Isolating Local Contributions

Application of the *VDM* requires knowledge of rooftop concentrations to estimate surface concentrations, but rooftop concentrations are not available at all locations. We can develop a model to estimate rooftop concentration by assuming the effect of local traffic emissions on rooftop concentrations is matched by the vertical transport on the rooftop,

$$Q = \gamma C_r \sigma_{wr} W \tag{3-7}$$

where C_r is the rooftop concentration due to local traffic emissions, σ_{wr} is the standard deviation of the vertical turbulent velocity fluctuation at the rooftop, and γ is a constant. Substituting equation (3-7) into equation (3-5) yields,

$$C_s = \frac{Q}{\gamma W \sigma_{wr}} \left[1 + \frac{\gamma \sigma_{wr}}{\beta \sigma_w} \frac{H(1+a_r)}{H + h_o(1+a_r)} \right] \tag{3-8}$$

where C_s is the surface concentrations due to local traffic emissions.

With the new formulation, it is now possible to evaluate *VDM* using surface concentrations that are due to local traffic emissions. However, we must remove the background concentration from the surface concentration measurements to compare observations with equation (3-8). An advantage of high resolution concentration measurements is the possibility of isolating the concentration signals due to local traffic emissions. As shown in the top left panel of Figure 3-20, the 1-second *PNC* data indicates that the total concentration consists of high frequency spikes superimposed on top of a slowly varying baseline concentration. We suspect the high frequency spikes result from local traffic emissions, while the slow varying baseline represents the regional background concentration. We developed a method to isolate the local contributions from the total concentrations: the minimum concentration within a specified time window (5min) is taken to be the baseline concentration as shown in the top panels of Figure 3-20. The window size is arbitrary, but it should be larger than the average peak duration (which is typically around 1min), and small enough to capture the underlying baseline trend. The resulting baseline concentrations estimated using this method for all 5 *CPCs* used on May 9th on 8th St. are shown in Figure 3-21; as one can see, the baseline at all locations has a similar trend, which indicates the baseline we calculated could very likely be the regional background. We assume the differences between the total concentrations and the baseline

concentrations are the local traffic contributions.

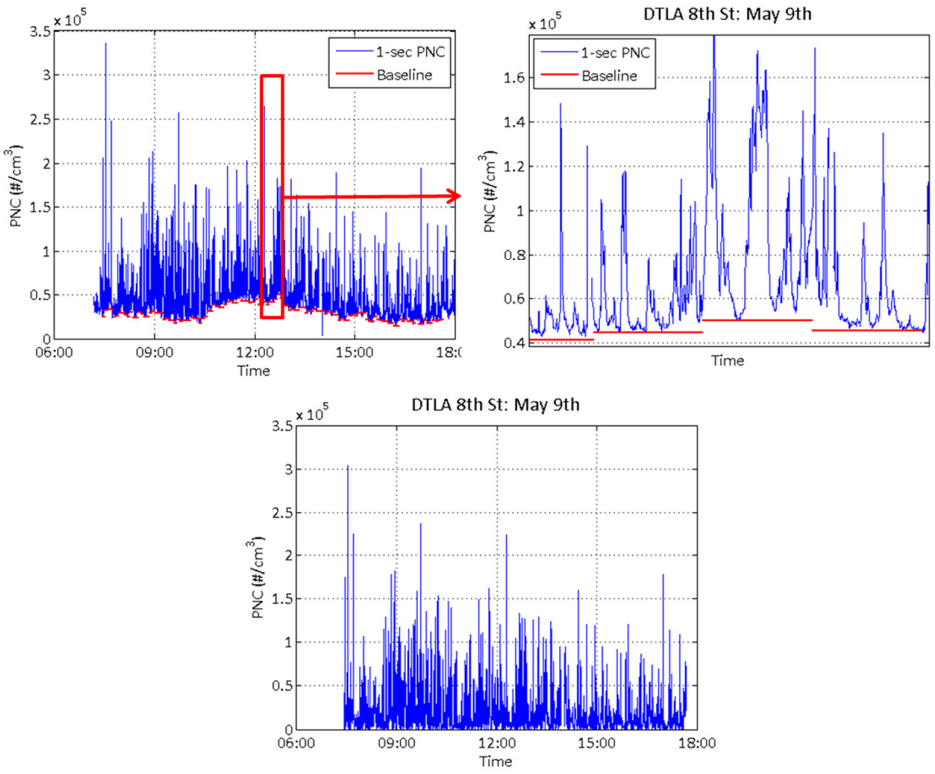

Figure 3-20 Separating local signals from the total concentrations: the minimum concentration within each 5-min interval is taken to be the baseline concentration for that particular interval. Top panels: total *PNC* (blue solid line) and the estimated baseline *PNC* (red solid line). Bottom panel: time series of the local *PNC*, which is taken to be the differences between the total *PNC* an the baseline *PNC*

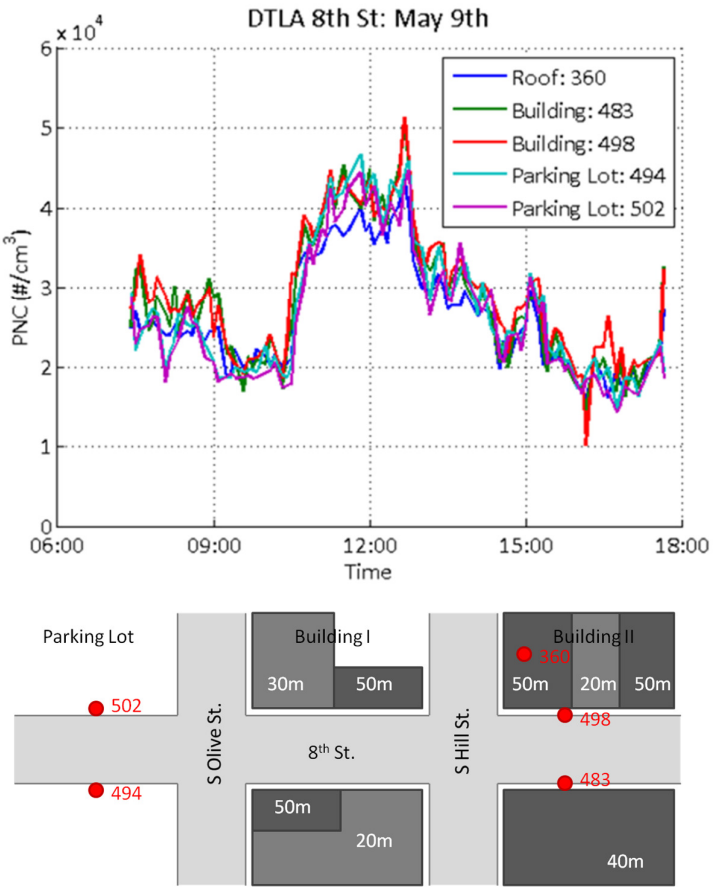

Figure 3-21 Top Panel: Estimated baseline concentrations at the 5 locations on 8th St. As shown, the baselines at the 5 locations are almost identical, which suggests that the baseline can be treated as background concentrations. Lower Panel: *CPC* locations

How will the selected window size affect the resulting baseline and local concentrations? As shown Figure 3-22, the window size mainly affects the magnitude of the baseline and local *PNC*; larger window size results in smaller baseline concentrations and larger local concentrations. The temporal variation of both the baseline and local *PNC* remain the same, and are relatively insensitive to the window size. Thus the choice of window size should not significantly alter the outcome of the model evaluation.

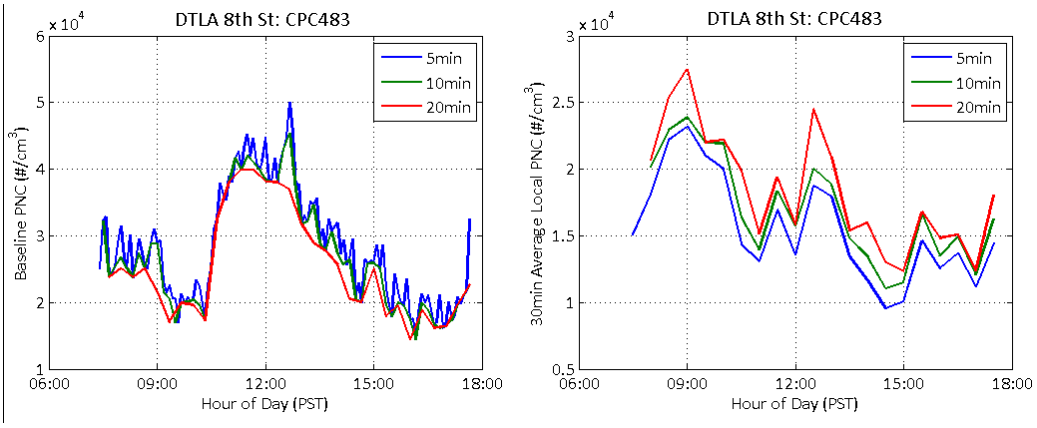

Figure 3-22 Sensitivity of baseline and local *PNC* to the window size. Left Panel: Baseline concentrations calculated with 3 difference window sizes, 5 minute, 10 minute, and 20 minute. Right Panel: 30min average local *PNC* calculated with the 3 window sizes.

The time series of the local contributions on 8th St. on both May 7th and May 9th are shown in Figure 3-23. The surface local contributions are the average of the local contributions on both sides of 8th St. On May 9th, the rooftop local *PNC* stays relatively constant throughout the entire day, while both the *Parking Lot* and *Building II* region local *PNC* decrease over time. It is important to note that the local PNC in the *Building II* region is roughly 50% higher than that at the *Parking Lot* on May 9th. On May 7th, the local PNC in the *Building II* region is almost twice that of the *Parking Lot*. The higher concentration in the *Building II* region on both days seems to indicate that buildings magnify concentrations due to local emissions.

Next, we plot the *PNC* at surface level against the local surface $1/\sigma_w$. The total *PNC* versus $1/\sigma_w$ is shown in the left panel of Figure 3-24. As shown, there is no correlation between the measured total *PNC* and $1/\sigma_w$. The right panel of Figure 3-24

shows the local concentrations (*Total PNC-Baseline PNC*) versus the local surface $1/\sigma_w$. It is clear that the correlation improved substantially, with r^2 increasing from 0.04 to 0.58. This good correlation again seems to indicate that the emission rate is constant over selected periods of time, similar to what we found previously. This illustrates the uncertainty in relating *UFP* emissions to the traffic flow rate and a constant emission factor, since variation in vehicle speed and acceleration can significantly affect the emission factor (Kittelson et al., 2004).

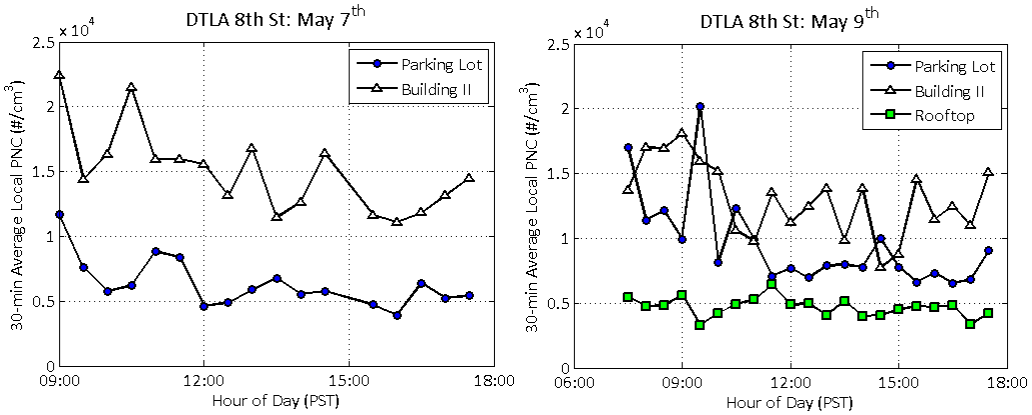

Figure 3-23 Time series of local *PNC* measured on 8th street on May 7th (Left Panel) and May 9th (Right Panel)

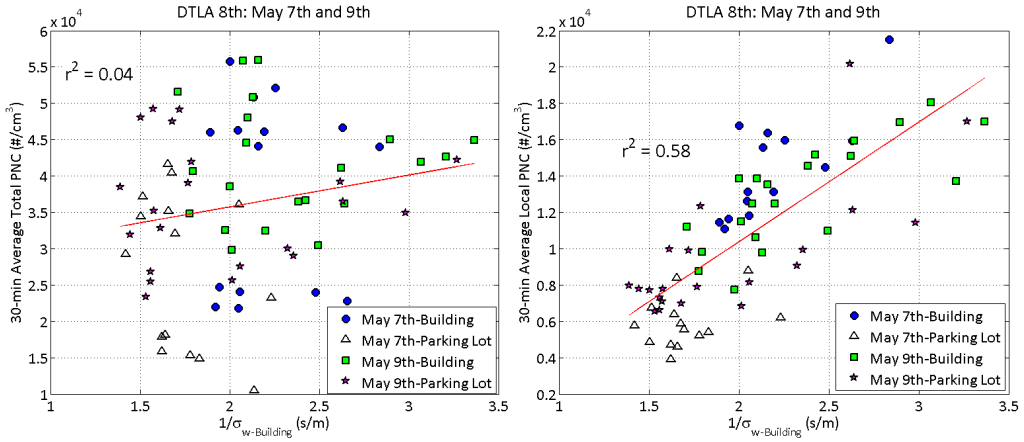

Figure 3-24 *DTLA* 8th street Left panel: Total *PNC* versus local surface $1/\sigma_w$. Right panel: Local *PNC* versus local surface $1/\sigma_w$.

The same method is applied to isolate local contributions in Temple City. The temporal variation of the local *PNC* on Jan 15th, 16th, and 17th are shown in Figure 3-25. There is correlation between the local *PNC* on the rooftop and street level as expected since the two locations are only 6m apart. The local *PNC* is not correlated with local $1/\sigma_w$ as shown in Figure 3-26.

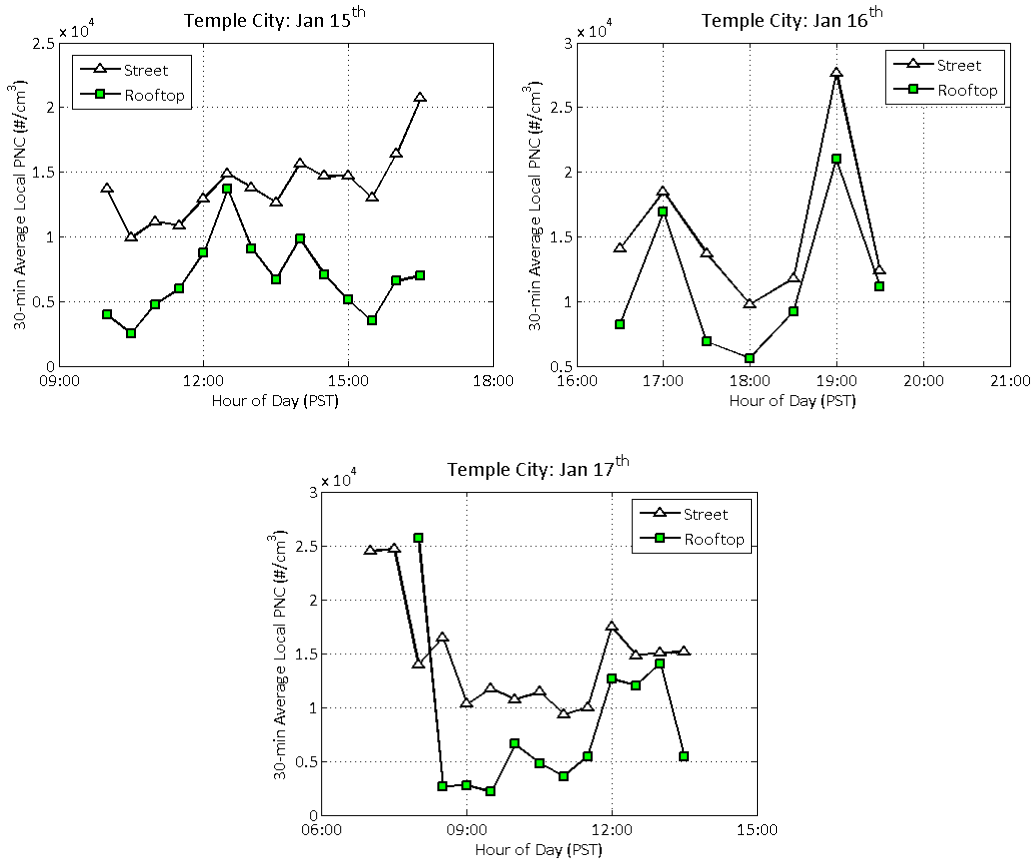

Figure 3-25 Time variation of the local contribution measured in Temple City.

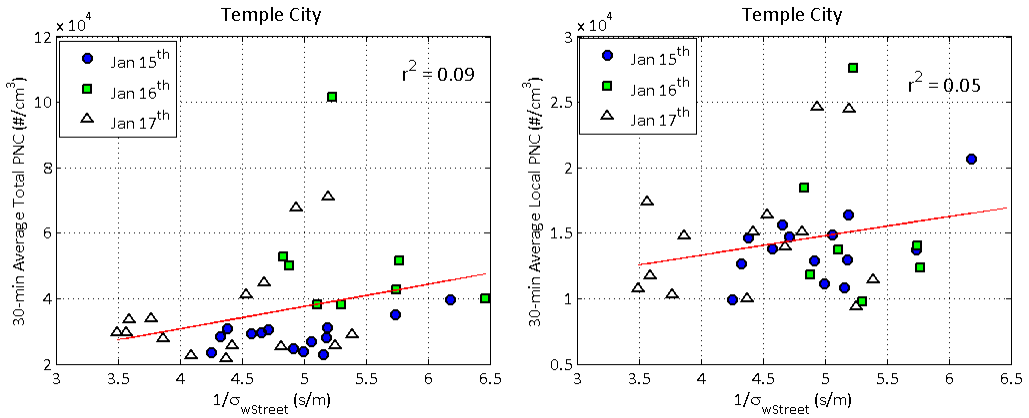

Figure 3-26 Concentration versus $1/\sigma_w$ in Temple City. Left panel: Total *PNC* versus local surface $1/\sigma_w$. Right panel: Local *PNC* versus local surface $1/\sigma_w$.

Schulte et al (2014, *submitted*) has applied *VDM* to the data from the field studies conducted in 8th St, 7th St, and Temple City, and also at a site on Wilshire Blvd in Beverly Hills, using $h_0 = 2m$, $\gamma = 1.25$ and $\beta = 0.4$. Figure 3-27 indicates that the model provides a good description of the measured local contributions of *UFP* at most of the sites. This implies that local contributions are primarily governed by the equivalent aspect ratio of the building area and the standard deviation of the vertical turbulent velocity fluctuations. The temporal variation of the local *PNC* at a site is controlled by the vertical turbulent velocity fluctuation, while the spatial variation of the *PNC* at different sites is mainly determined by the aspect ratio.

VDM underestimated the local *PNC* at the *Parking Lot/Open* region of 8th St substantially when an aspect ratio of zero is used. However, the definition of effective building height is somewhat arbitrary and it is not clear how the building height should be defined for the open area. When the aspect ratio is manually increased from

0 to 1, the model estimates become unbiased (Schulte et al., 2014, *submitted*).

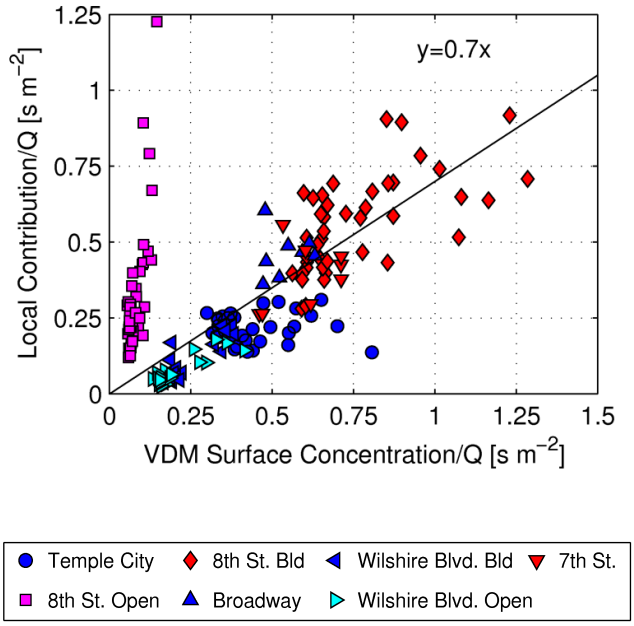

Figure 3-27: Comparison of *VDM* estimates of surface concentrations with half hour averaged local contributions at different sites. Concentrations are normalized by daily average emission rate, assuming an emission factor of 10^{14} particles/km/vehicle (adapted from Schulte et al., 2014, *submitted*).

3.6 Models to Estimate Urban Micrometeorology from Upwind Rural Measurements

In the previous chapter, we showed that disperion in urban areas is described by the vertical dispersion model, which relates concentrations to the street aspect ratio and the vertical turbulent velocity fluctuations, σ_w. Aspect ratio can be obtained from a *GIS* database, but obtaining mircometeorology data such as σ_w is difficult. Routine measurements of micrometorology are usually made in rural areas, such as in the nearby airports, and not in urban areas. Thus, we formulate models that allow us to estimate urban surface variables using upwind rural measurements. The models are

evaluated with micrometeorologual data collected on 8th St of Downtown Los Angeles, and on Las Tunas Dr. of Temple City.

We model the evolution of turbulence from rural to urban street level in two steps: (1) using an Internal Boundary Layer (*IBL*) model to estimate urban rooftop micrometeorological variables from upwind rural variables, described in section 3.6.1, and (2) using an Urban Canopy model to estimate urban surface level turbulence using the corresponding rooftop values, described in section 3.6.5.

All the following analyses are based on 1-hour averaged data collected with the 3-D sonic anemometers. The formulations used to calculate the various micrometeorology parameters are described in the Appendix. The 10Hz raw sonic anemometer data was processed with a custom program written in MatLab®.

3.6.1 Internal Boundary Layer (IBL) Model Formulation

The relationship between the rooftop σ_w and the upwind σ_w can be estimated using an internal boundary layer model (Luhar et al, 2006). As shown in Figure 3-28, as the flow travels from rural area to the urban area, an internal boundary layer (*IBL*) develops as a result of the flow adjustment to the changes in surface roughness. Within the *IBL*, flow is adjusted to the urban surface roughness; above the *IBL*, the upwind rural flow is undisturbed. We assume the wind speed retains its upwind rural value at the top of the *IBL*. By enforcing the condition that the upwind rural wind speed and the wind speed adjusted to the surface roughness must match at the top of

the *IBL*, we can estimate the micrometeorological variables in the urban area using the corresponding upwind values.

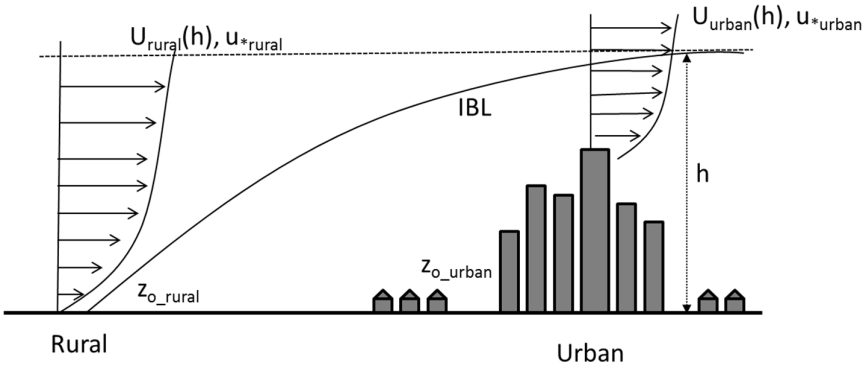

Figure 3-28 Schematic of the *IBL* model

The vertical profile of the horizontal wind speed in flat terrain can be described using the similarity velocity profile (Van Ulden and Holtslag, 1985),

$$U_{(z)} = \frac{u_*}{k}\left[ln\left(\frac{z-d}{z_o}\right) - \psi_m\left(\frac{z-d}{L}\right) + \psi_m\left(\frac{z_{o\_}}{L}\right)\right] \quad \textbf{(3-9)}$$

where ψ_M is the stability function defined as,

$$\psi_M = -4.7\frac{z-d}{L}, \qquad when\ L > 0 \quad \textbf{(3-10)}$$

$$\psi_M = 2\frac{z-d}{L}ln\left(\frac{1+x}{2}\right) + ln\left(\frac{1+x^2}{2}\right) - 2tan^{-1}(x) + \frac{\pi}{2}, \quad when\ L < 0 \quad \textbf{(3-11)}$$

$$x = \left(1 - 15\frac{z}{L}\right)^{1/4} \quad \textbf{(3-12)}$$

where z is the height above ground, z_o is the roughness length, d is the displacement height and can be estimated as $5z_o$ (Britter and Hanna, 2003) , L is the Monin-

Obukhov length (see Appendix for definition), and u_* is the surface friction velocity. The logarithmic velocity profile for the rural area results in the following wind speed at the top of the *IBL*,

$$U_{(IBL)} = \frac{u_{*rural}}{k}\left[ln\left(\frac{h - d_{rural}}{z_{o\_rural}}\right) - \psi_m\left(\frac{h - d_{rural}}{L_{rural}}\right) + \psi_m\left(\frac{z_{o\_rural}}{L_{rural}}\right)\right] \quad \textbf{(3-13)}$$

where h is the *IBL* height. The wind speed below the *IBL* height is adjusted to the urban surface roughness, resulting in the following expression for the wind speed at the top of the *IBL,*

$$U_{(IBL)} = \frac{u_{*urban}}{k}\left[ln\left(\frac{h - d_{urban}}{z_{o\_urban}}\right) - \psi_m\left(\frac{h - d_{urban}}{L_{urban}}\right) + \psi_m\left(\frac{z_{o\_urban}}{L_{urban}}\right)\right] \quad \textbf{(3-14)}$$

Equating the two equations, we obtain the following expression to relate urban surface friction velocity u_{*urban} to the upwind rural friction velocity u_{*rural},

$$\frac{u_{*urban}}{u_{*rural}} = \frac{\left[ln\left(\frac{h - d_{rural}}{z_{o\_rural}}\right) - \psi_m\left(\frac{h - d_{rural}}{L_{rural}}\right) + \psi_m\left(\frac{z_{o\_rural}}{L_{rural}}\right)\right]}{\left[ln\left(\frac{h - d_{urban}}{z_{o\_urban}}\right) - \psi_m\left(\frac{h - d_{urban}}{L_{urban}}\right) + \psi_m\left(\frac{z_{o\_urban}}{L_{urban}}\right)\right]} \quad \textbf{(3-15)}$$

As shown in the equation, the computation of urban $u_*$from rural u_* requires the height of *IBL*. The formulation we used to estimate the *IBL* height is described in Section 3.6.2. With the estimated u_*, the rooftop σ_w can, in principle, be estimated using the Monin-Obukhov similarity theory (MO theory). In section 3.6.4, we will examine the applicability of MO theory in urban areas.

3.6.2 Estimating Internal Boundary Layer (IBL) Height

To estimate the *IBL* height in urban areas, we used the 2-dimensional formulation described by Savelyev and Taylor (2005). The model assumes that *IBL* growth rate is proportional to the vertical turbulent velocity fluctuation.

$$U(h)\frac{dh}{dx} = A\sigma_w \tag{3-16}$$

where $U(h)$ is the wind speed at the *IBL* height, h is the IBL height, σ_w is the vertical turbulent velocity fluctuation in the urban area, and A is a constant that can be calculated using the following empirical formula (Savelyev and Taylor, 2001),

$$A = 1 + 0.1 \cdot ln\left(\frac{z_{o\_urban}}{z_{o\_rural}}\right) \tag{3-17}$$

Assuming the MO-theory holds within the urban canopy layer, we can relate σ_w to the surface friction velocity through equation (3-18). Combining equation (3-8), (3-16), and (3-18) and solving numerically, we obtain the *IBL* height.

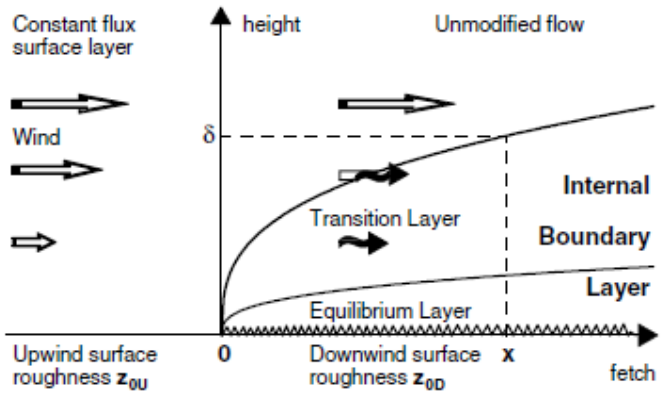

Figure 3-29 Development of 2-D internal boundary layer (adapted from Savelyev and Taylor, 2005)

3.6.3 IBL Model Evaluation

The *IBL* model has previously been evaluated with data collected in Riverside, California by Qian (2010). Stability information in urban areas is not usually available. Thus, when the upwind rural atmospheric condition is stable (*Lr>0*), Qian set both the rural and urban MO-length to infinity, corresponding to neutral conditions. When the upwind rural area is unstable (*Lr<0*), the MO-Length of the urban area, L_u, is set to equal to L_r (Qian, 2010). The observed u_* versus *IBL* model estimated u_* in the urban area is plotted in Figure 3-30. As shown, the model overestimates urban u_* for both the stable and unstable upwind conditions.

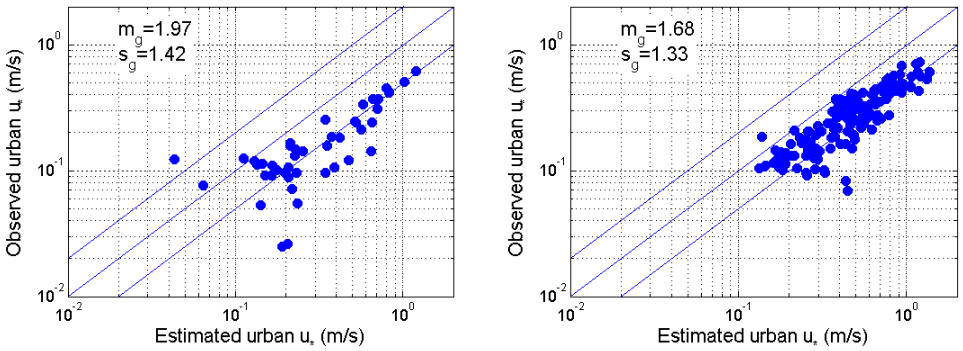

Figure 3-30: Scatter plot of u_* estimated from the IBL model versus observed values over the urban areas. Left Panel: when observed $L_R > 0$, L_U and L_R are set to infinity. Right Panel: when observed $L_R < 0$, L_U is set equal to L_R (Figure adapted from Qian, 2010)

We evaluated the *IBL* model with data collected during the 8th St. and Temple City measurements. The surface roughness length used in the *IBL* model is estimated using measured wind speed and u_* through the method described in appendix A.3. For the *DTLA* 8th St. measurements, we found that assuming neutral conditions

(Lr=Lu=∞) at all occasions yields the best result. As shown in the left panel of Figure 3-31. The model shows no bias in estimating the urban rooftop u_* (m_g=1.05), and 81% of the data is within factor 2 of the observed value. The model result is less satisfactory when applied to the Temple City data as shown in the right panel of Figure 3-31. There is large scattering between the model estimates and observations.

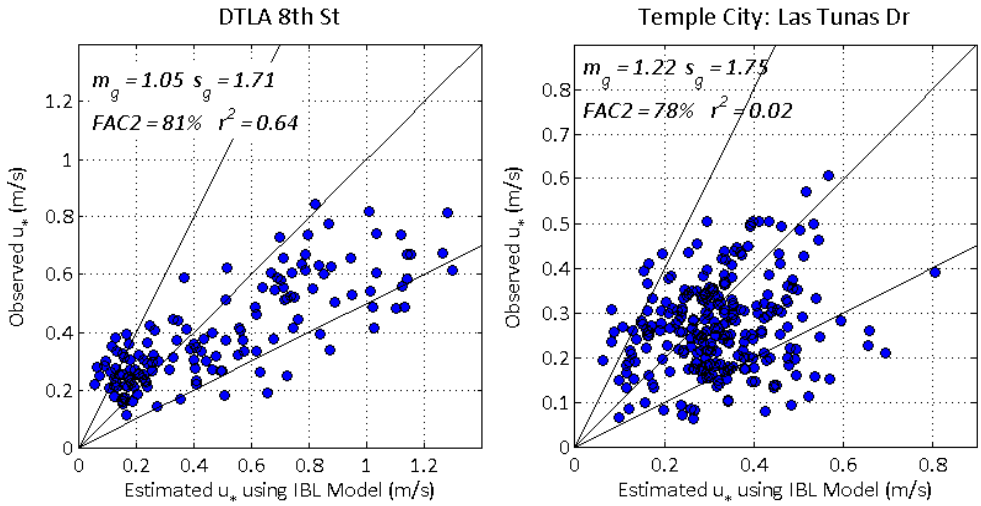

Figure 3-31 Observed u_* versus estimated u_* using the *IBL* model assuming neutral conditions at both the rural and urban sites, that is, $Lr = Lu = \infty$. Left Panel: Downtown LA. Right Panel: Temple City

As shown in Figure 3-31, the *IBL* model overestimates the urban u_* by 16%, and the model shows fairly large scattering (s_g = *1.71*). The model estimates correlate well with the observed values (r^2 = *0.64*). The correlation is good because of the good correlation between observed u_* in the rural area and in urban area. The observed upwind rural u_* and urban rooftop u_* in Temple City are not correlated, thus the model is not able to produce satisfactory correlation between the model estimates and

observations. When u_* is small in the upwind rural area (<0.2 m/s), urban u_* could still range from 0.2 to 0.4 m/s. This phenomenon is not captured by the *IBL* model.

As mentioned in section 3.6.2, the *IBL* model relies on the Monin-Obukhov (MO) similarity theory to relate σ_w and u_*. However, the MO similarity theory is only valid within the inertial sublayer of a horizontally homogeneous boundary layer, and may not be valid within the urban roughness sublayer (Monin and Obukhov, 1954). The next section evaluates the applicability of MO similarity theory to estimating the urban σ_w.

3.6.4 Application of the Monin-Obukhov Similarity Theory (MO Theory)

In this section, we examine the applicability of MO similarity theory for estimating σ_w within the urban roughness sublayer. The formulation for estimating σ_w using MO theory is presented in equation (3-18a) and equation (3-18a) (Panofsky, et al, 1977).

$$\sigma_w = 1.3u_* \left(1 - \frac{z-d}{kL}\right)^{1/3}, \qquad for\ L < 0 \tag{3-18a}$$

$$\sigma_w = 1.3u_*, \qquad for\ L \geq 0 \tag{3-18b}$$

where L is the MO length, z is the measurement height, d is the displacement height, which is assumed to be $5z_o$ (Britter and Hanna, 2003), and k (~0.4) is the von Karman constant. The urban surface level clearly does not satisfy the condition of spatial homogeneity required by the theory, but there are suggestions that the MO theory

could be applied if local fluxes are used in the formulations (Beljaars et al, 1983; Rotach, 1995).

We compared the observed σ_w with the σ_w estimated using MO similarity theory. The comparison for the data measured on the urban rooftop is shown in Figure 3-32. When using measured MO length, the model overestimates the rooftop σ_w by 16%. Assuming neutral conditions, the model provides unbiased estimations.

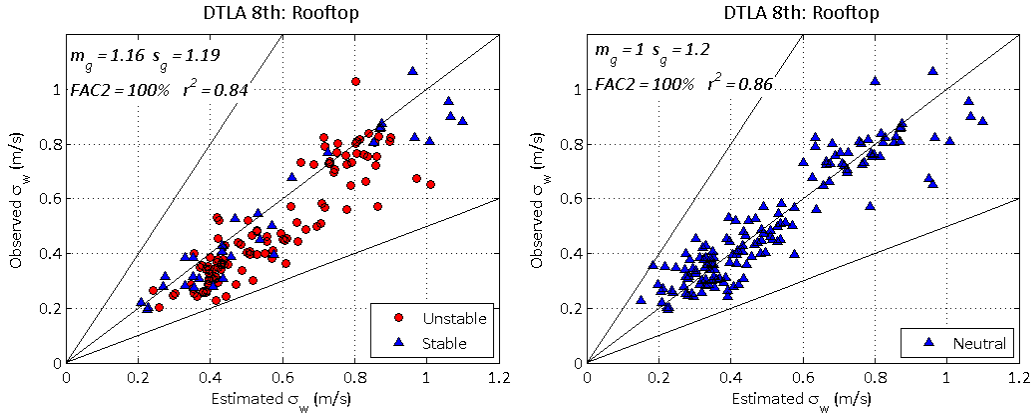

Figure 3-32 Comparison of the vertical turbulent velocity fluctuation (σ_w) estimated using MO theory versus the corresponding observed value at the urban rooftop of *DTLA* 8th St. Left Panel: using measured MO length. Right Panel: Assuming neutral conditions ($|L|=\infty$)

The performance of the MO theory in estimating rooftop σ_w in Temple City is similar to that in *DTLA* 8th St. As shown in Figure 3-33, the model overestimates the rooftop σ_w by 50% when the stability effects are included; assuming neutral conditions yields more satisfactory results.

The estimation of the urban surface σ_w within a street from upwind rural values is accomplished in two steps: 1) using the Internal Boundary Layer (*IBL*) model to

estimate the urban rooftop value, and (2) using an Urban Canopy model to estimate urban surface level σ_w using the corresponding rooftop values. The previous model evaluation shows that the *IBL* model provides an adequate estimate of the rooftop σ_w. The next section describes an Urban Canopy model to accomplish the second step.

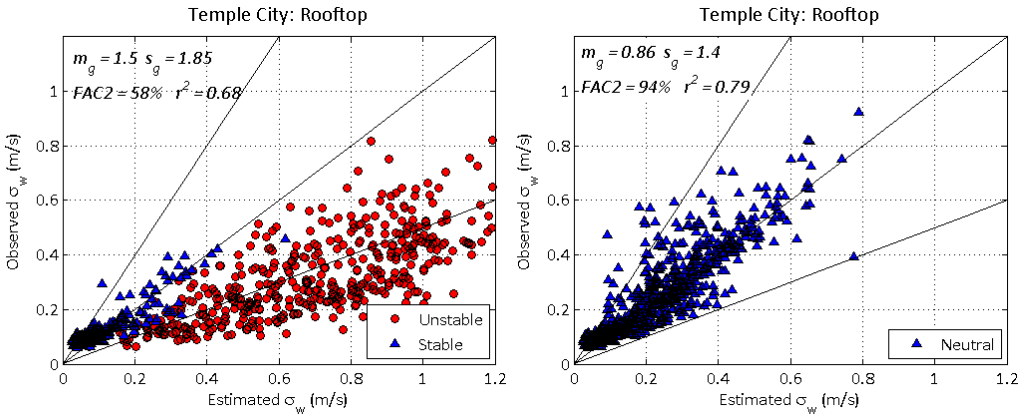

Figure 3-33 Comparison of the vertical turbulent velocity fluctuation (σ_w) estimated using MO theory versus the corresponding observed value at the urban rooftop of Temple City. Left Panel: using measured MO length. Right Panel: Assuming neutral conditions ($|L|=\infty$)

3.6.5 A Model to Estimate Vertical Turbulent Velocity in the Urban Canopy

The above models relate rooftop surface friction velocity u_* and vertical turbulent velocity σ_w with upwind data. However, the vertical dispersion model requires estimates of the turbulence in the urban canopy. One method to estimate the turbulence within the street is to convert the wind speed to a vertical turbulent velocity by assuming a constant turbulent intensity. This method is described in section 3.7. Alternatively, we can relate rooftop and within-canopy turbulence through a semi-empirical model, described next.

If we assume the energy production at the rooftop is equal to dissipation within the urban canopy, that is,

$$\overline{u'w'}\frac{du}{dz}\sim\varepsilon \tag{3-19}$$

where ε is the turbulent dissipation rate, and $\overline{u'w'}$ is the vertical momentum flux which can, by definition, be expressed as u_*^2. Through the MO similarity theory we can write $u_*^2\sim\sigma_{wr}^2$. The vertical gradient of horizontal velocity can be estimated from the similarity wind profile (equation (3-9)) as: $\frac{du}{dz}=\frac{u_*}{kz}$, which can be estimated as $\frac{u_*}{kz}\sim\frac{\sigma_{wr}}{H}$. The turbulent dissipation rate is estimated as $\varepsilon\sim\frac{\overline{\sigma_w}^3}{l}$. Thus, we can rewrite equation (3-19) as,

$$\sigma_{wr}^2\frac{\sigma_{wr}}{H}\sim\frac{\bar{\sigma}_w^3}{l} \tag{3-20}$$

where l is the mixing length,

$$l=\frac{HW}{H+W} \tag{3-21}$$

Rearranging, we get the following equation that relates rooftop σ_{wr} to the canopy average $\bar{\sigma}_w$,

$$\frac{\sigma_{wr}}{\bar{\sigma}_w}=\left(1+\alpha\frac{H}{W}\right)^{1/3} \tag{3-22}$$

where σ_{wr} is the rooftop vertical turbulent velocity fluctuation, $\overline{\sigma_w}$ is the average vertical turbulent velocity fluctuation within the urban canopy, and α is an empirical

constant (~ 0.4). The vertical average turbulent velocity fluctuation can be related to rooftop and surface values as,

$$\frac{1}{\bar{\sigma}_w} = \frac{1}{2}\left(\frac{1}{\sigma_{wr}} + \frac{1}{\sigma_{ws}}\right) \tag{3-23}$$

Figure 3-34 shows the site average $\sigma_{wr}/\bar{\sigma}_w$ versus the quantity within parenthesis in equation (3-22), where α is taken to be 0.4. The figure shows that higher aspect ratios correspond to higher $\frac{\sigma_{wr}}{\bar{\sigma}_w}$ ratios, and the data roughly follow the 1/3 power as estimated by equation (3-22). More data is needed to fully evaluate equation (3-22), especially at sites with small to mid-range aspect ratios.

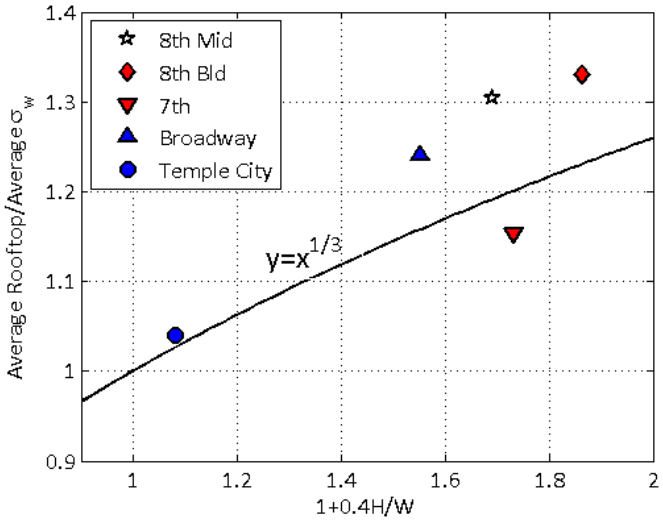

Figure 3-34 Ratio of roof level σ_w to surface σ_w versus the aspect ratio, *H/W*, of each site.

If we substitute equations (3-23) into equation (3-22), we obtain the following relation between the urban rooftop and urban surface σ_w,

$$\frac{\sigma_{wr}}{\sigma_{ws}} = 2\left(1 + \alpha\frac{H}{W}\right)^{1/3} - 1 \qquad \textbf{(3-24)}$$

The estimated surface σ_w compares well with the measured value at several locations in *DTLA* as shown in Figure 3-35. In Temple City, the model overestimated the surface σ_w by a factor of 2. We suspect this could be because the street level sonic anemometer was placed too close to the buildings, so the measured turbulence is too small, and is not representative of the average surface turbulence.

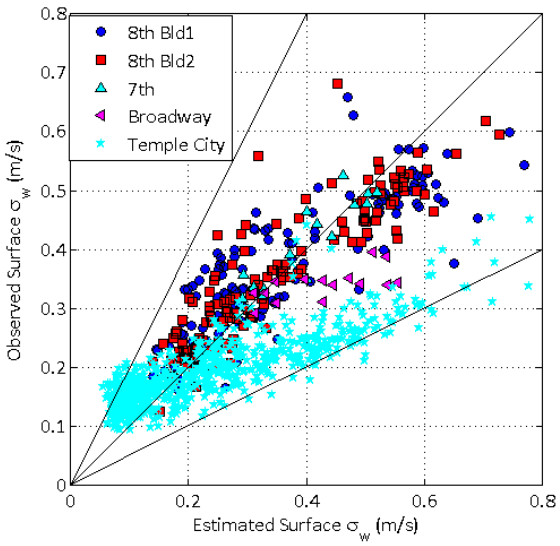

Figure 3-35 Comparison of estimated surface σ_w (equation (3-24)) with measured surface σ_w.

Figure 3-36 shows the result of the complete upwind to urban surface micrometeorology model. As shown, the model provides reasonable estimates of the urban surface σ_w, using upwind variables. The model overestimates the upper range (σ_w = 0.2~0.6 m/s) of urban surface turbulence by about a factor of two, and underestimates the lower range (σ_w = 0.1~0.2 m/s). The model bias mainly results

from the limitations in the *IBL* model: when rural turbulence is very small, the *IBL* model suggests small turbulence in the urban area, but our measurements show relatively large turbulence in urban areas even when turbulence in the upwind rural area is small. The higher turbulence in urban areas during night might result from the urban heat island effect, which the *IBL* model failed to capture. The urban canopy model provides unbiased estimates of urban surface turbulence using urban rooftop turbulence.

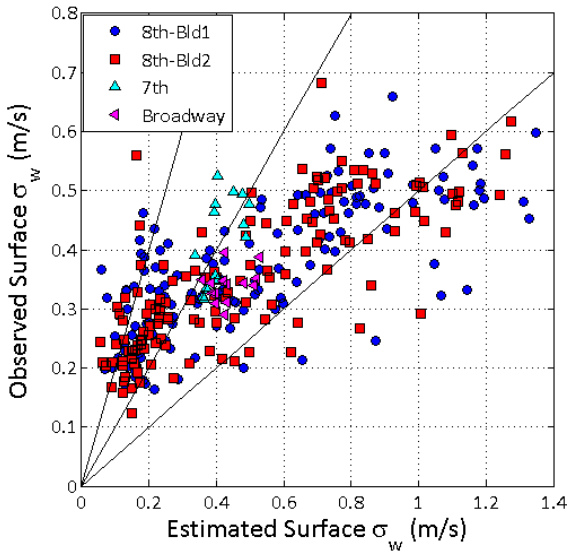

Figure 3-36 Observed versus estimated surface σ_w using *IBL* and urban canopy models.

3.7 Empirical Models to Estimate Wind Speed and Turbulence in the Urban Canopy

To estimate urban rooftop turbulence using the internal boundary layer (*IBL*) model, variables such the surface friction velocity, u_*, and the surface roughness, z_o,

at the upwind rural areas are required, but they are often not readily available. Another approach to estimate urban micrometeorology is to develop empirical models to relate micrometeorology within the urban canopy with upwind rural values. This section describes empirical relationships between urban rooftop and surface wind speed and turbulence with upwind values.

3.7.1 Turbulent Intensity in the Urban Canopy

Previous studies indicate that the turbulent intensity within the urban canopy may be assumed to be a constant value independent of building morphology (Hanna et al., 2007). *OSPM* for example assumes a turbulent intensity of 0.1 to calculate surface vertical turbulent velocity from the surface wind speed. It would be useful to translate observed wind speeds within the urban canopy to vertical turbulent velocities through a constant turbulent intensity. This motivates a comparison of the turbulent intensities within the different built environments where we have made micrometeorological measurements.

At 8th St., the vertical turbulent velocity fluctuations, σ_w, are well correlated with the corresponding wind speeds at all five locations, as shown in Figure 3-37, but as indicated by the slope, the turbulence intensities ($i_z = \sigma_w /U$) at the urban street level (*Parking Lot, Building I, and Building II*) are much higher than the rural turbulent intensity. Turbulent intensity i_z is 0.15 and 0.38 at the upwind and *Building II* region, respectively. This measured turbulence intensity is much higher than what is used in

the *OSPM*, in which the surface σ_w is assumed to be 0.1 of the surface wind speed (Hertel and Berkowicz, 2001).

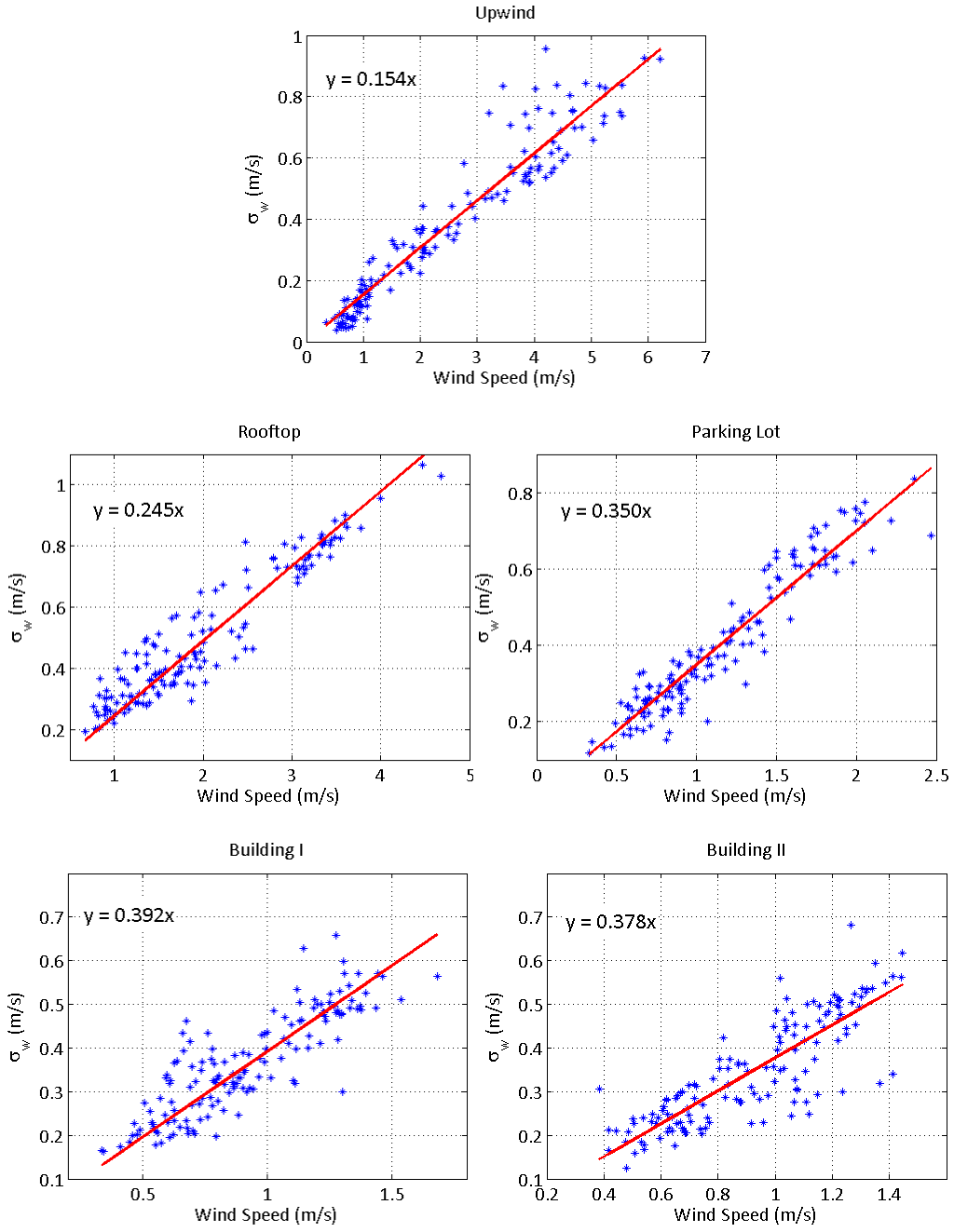

Figure 3-37 Vertical turbulent velocity fluctuation σ_w versus the corresponding wind speed on 8th St.

Similar plots are generated with the Temple City data as shown in Figure 3-38. The figure shows that the surface turbulent intensity measured in Temple City is similar to that of 8th St. (I_z=0.36).

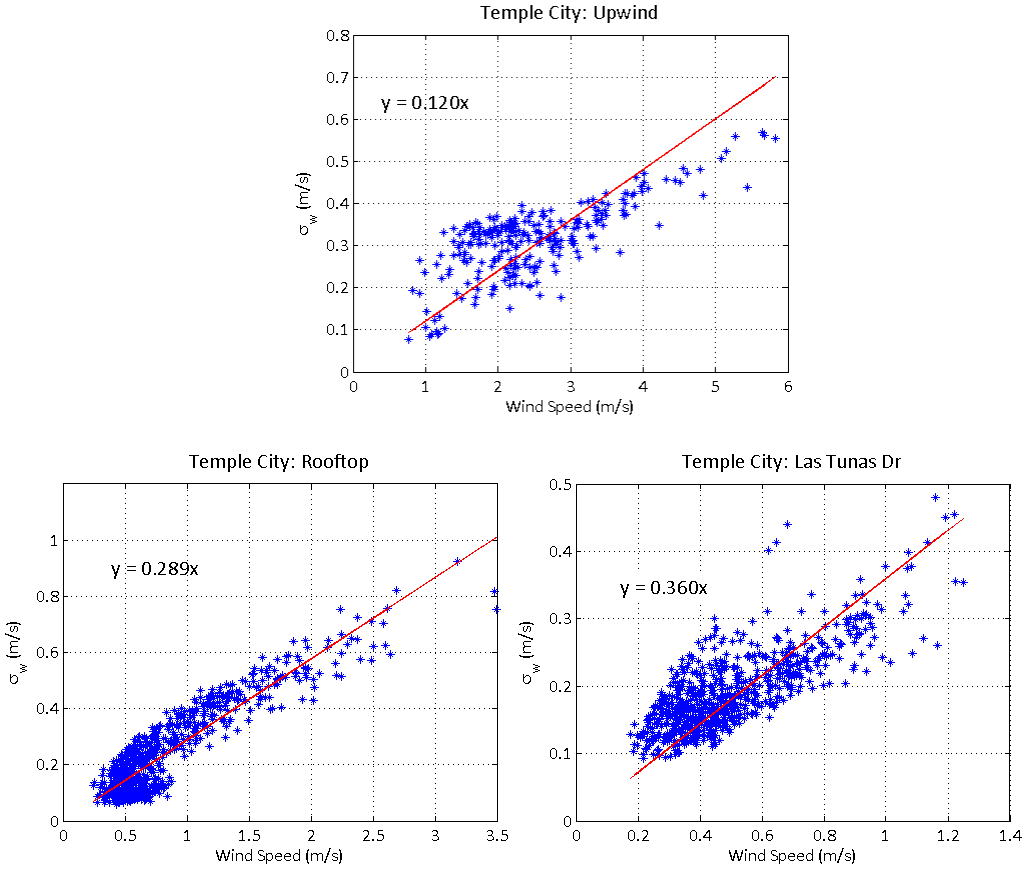

Figure 3-38 Vertical turbulent velocity fluctuation σ_w versus the corresponding wind speed in Temple City. Note: upwind only includes daytime measurements.

These results indicate that we can take a constant turbulent intensity of about 0.35-0.40 to estimate surface vertical turbulent velocity from wind speed in the urban canopy. This would be useful if measurements of wind speed are available within the urban area. Such observations are not commonly made, but we can relate the upwind rural and urban wind speeds. The next section shows the results of an empirical

comparison of the wind speed and turbulence at the urban surface level with upwind rural measurements.

3.7.2 Evolution of Wind Speed and Turbulence from Rural to Urban Surface

The ratios of wind speed, surface friction velocity, u_*, vertical turbulent velocity fluctuation, σ_w, and the cross wind turbulent velocity fluctuation, σ_v at the urban surface level to the corresponding upwind rural values are shown in Figure 3-39. As shown in the plots, wind speed in the urban area is always smaller than the upwind rural value. Urban surface friction velocity, u_*, and the vertical turbulence velocity fluctuation, σ_w, is smaller than the rural value during daytime, but could be 2.5 times larger than the upwind rural value during nighttime. This is likely due to the urban heat island effect: the atmosphere in urban areas does not stabilize after sunset, indicated by the positive heat flux, whereas the rural atmosphere stabilizes, resulting in much smaller σ_w values during the night. Interestingly, the cross wind velocity fluctuation, σ_v, is always higher in the upwind rural area than the urban areas, especially in the two building sections. This suggests that buildings reduce cross-wind meandering.

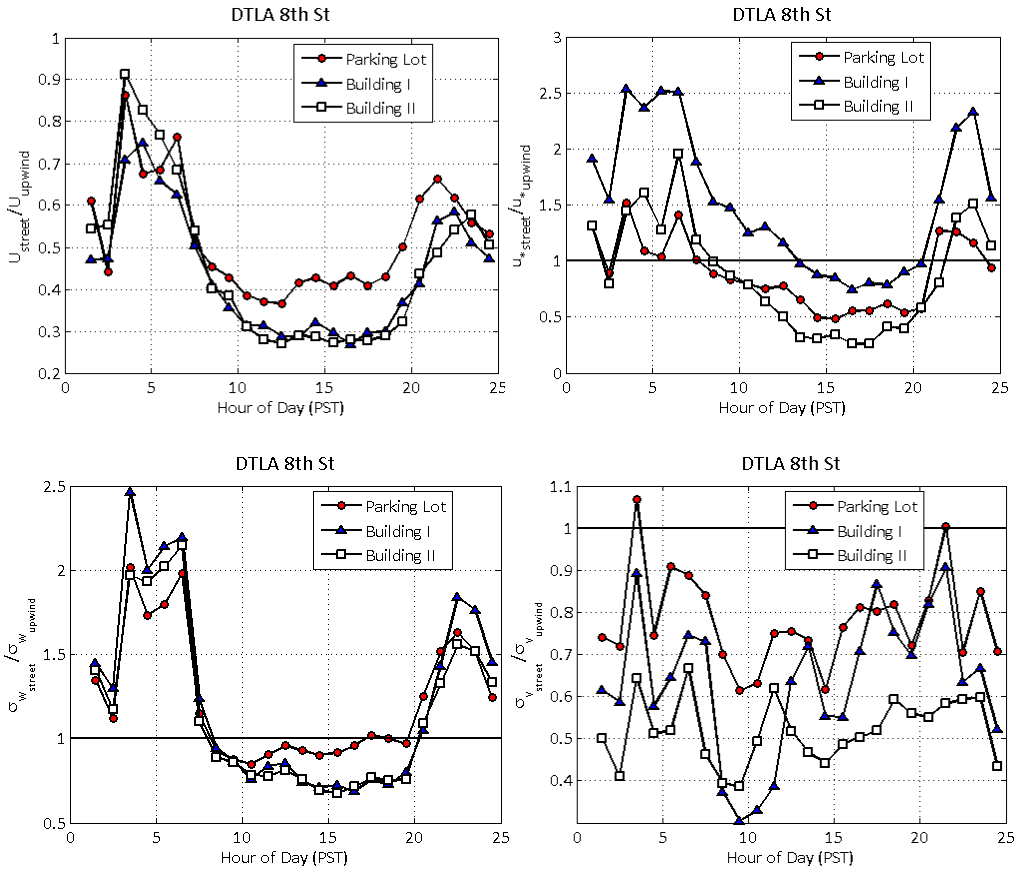

Figure 3-39 Ratio of urban surface micrometeorological variables to the corresponding upwind values as function of hour of day.

The evolution of turbulence from upwind to the urban surface can be divided into two steps: 1) increased turbulence from upwind to rooftop due to increased surface roughness 2) reduced turbulence from rooftop to surface caused by reduction in wind speed due to the buildings within the urban canopy. We first examine the correlation between the rooftop friction velocity u_* and vertical turbulent velocity fluctuation σ_w and their corresponding upwind values. As shown in Figure 3-40, u_* and σ_w at the urban rooftop are well correlated with the corresponding upwind values, and are about 24% and 13% higher than the upwind values, respectively. Next we compare the u_*

and σ_w measured at the 3 urban surface regions against the corresponding rooftop and upwind values. The plots are show in Figure 3-41 and Figure 3-42, respectively. From the plots, it is shown that σ_w measured at the 3 surface levels (*Parking Lot, Building I, & Building II*) are all very well correlated with the rooftop σ_w. The surface u_* are less well correlated with the rooftop u_*. The scattering is larger when comparing the 3 surface u_* and σ_w to the corresponding upwind values. Surface level σ_w and $u*$ are almost 70% of the rooftop value even though the rooftop measurements were made 50m above the surface level measurements; the large ratio suggests rapid vertical mixing, which is consistent with measurements made by Hanna and Chang (2014).

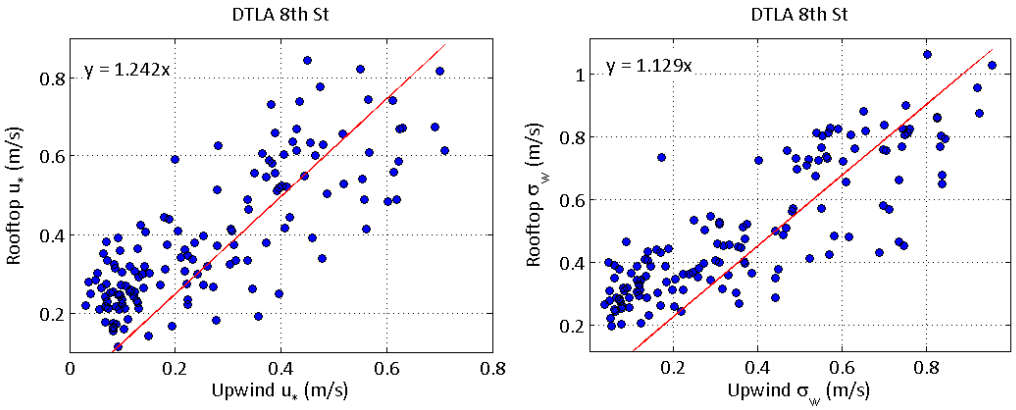

Figure 3-40 Rooftop friction velocity, u_*, and vertical turbulent velocity fluctuation σ_w versus the corresponding upwind values

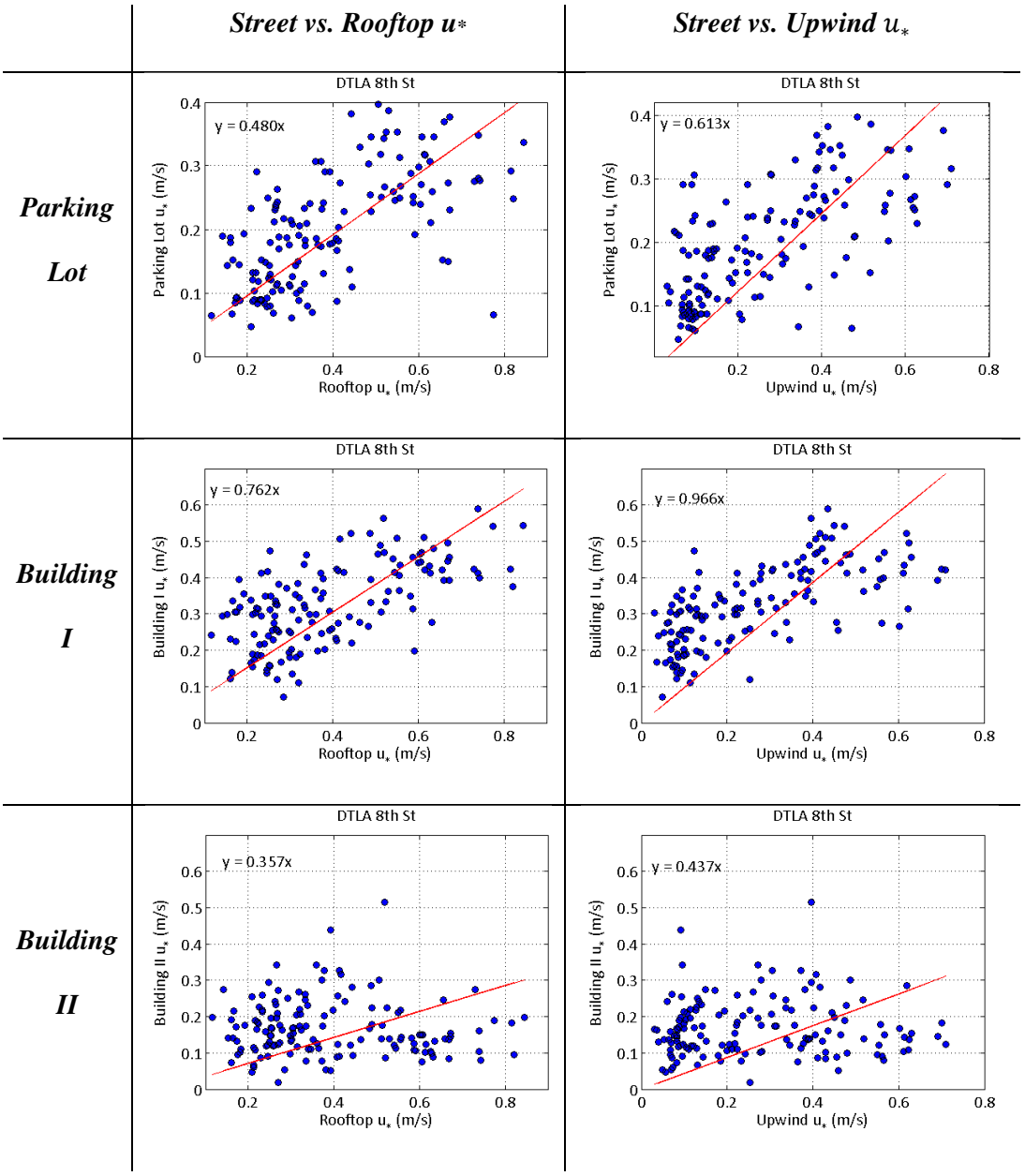

Figure 3-41 Left column: u_* measured at urban surface versus the corresponding rooftop value. Right Column: u_* measured at urban surface versus upwind value.

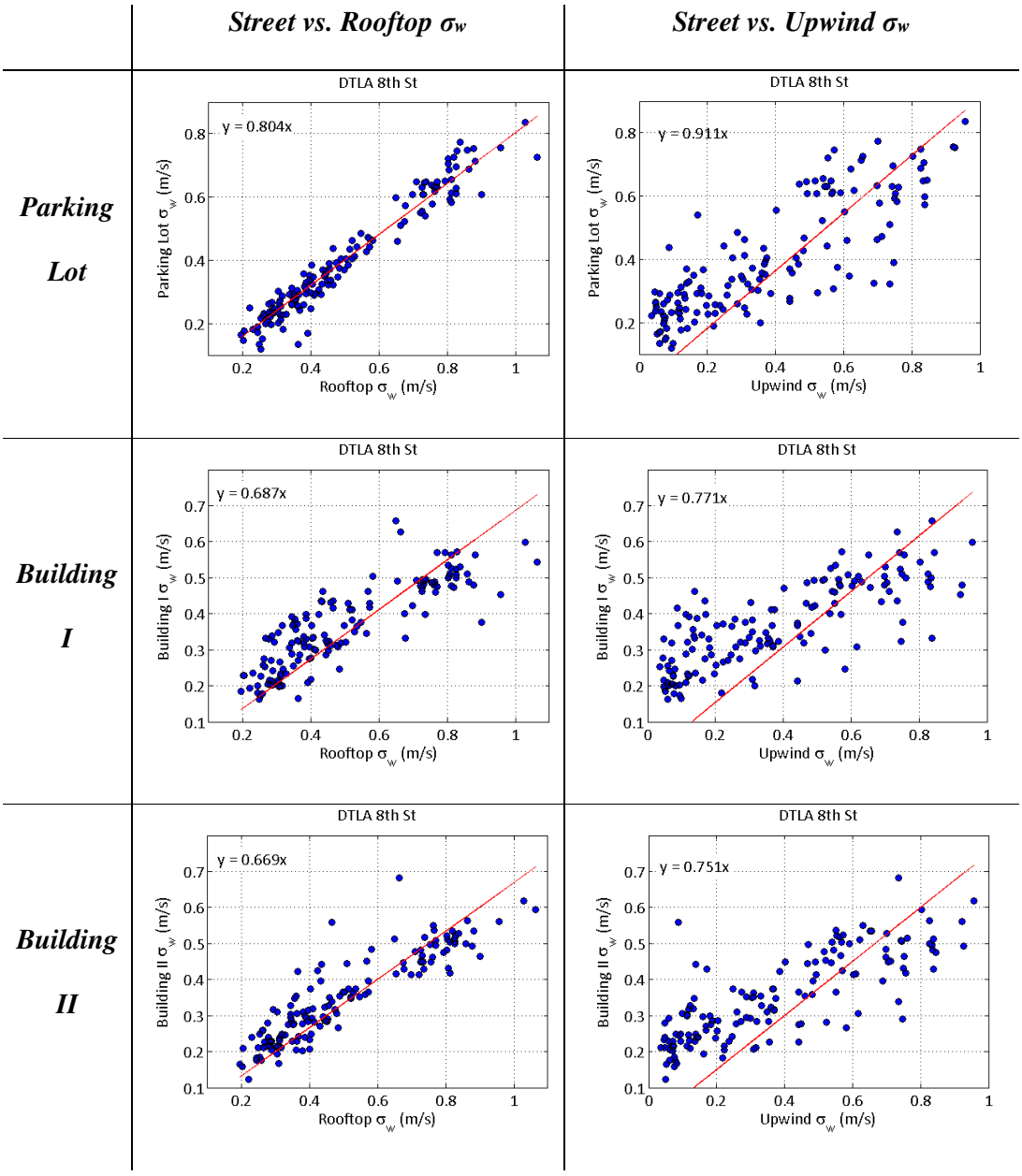

Figure 3-42 Left column: σ_w measured at urban surface versus the corresponding rooftop value. Right Column: σ_w measured at urban surface versus upwind value.

Plots of the time variation of the surface to rooftop, and surface to upwind $\boldsymbol{\sigma_w}$ ratios are depicted in Figure 3-43. As shown in the figures, there are large variations present in the urban surface to rooftop σ_w ratio, especially during nighttime. There are even larger variations in the urban surface to upwind σ_w ratio. The urban surface level σ_w, including *Parking Lot*, *Building I*, and *Building II*, could be 7 times higher than the corresponding upwind rural value during nighttime. Interestingly, the σ_w ratio in the *Parking Lot* stays relatively constant over time (roughly 80% of the rooftop value), while the ratio in the *Building I* and *Building II* regions shows a diurnal variation.

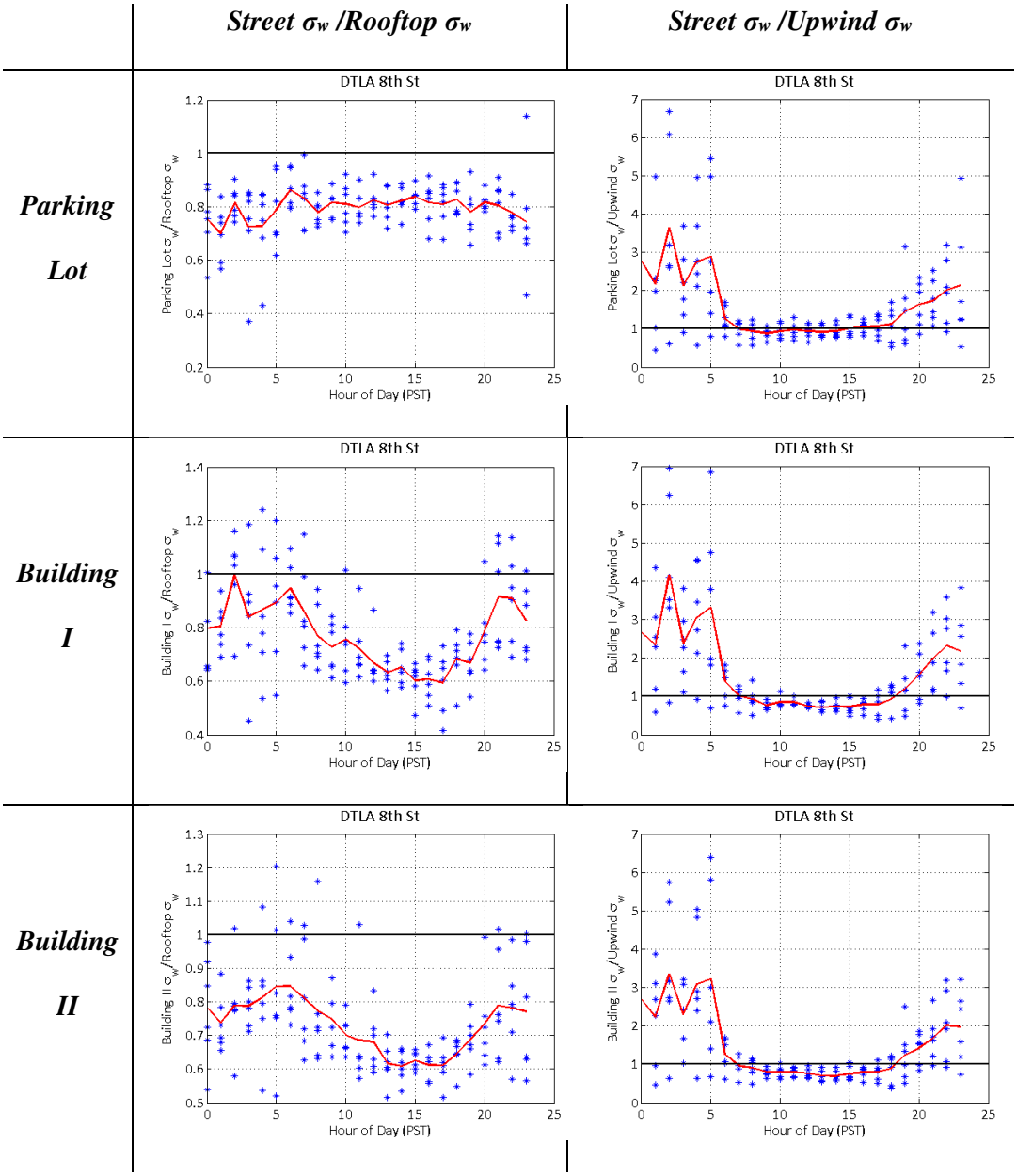

Figure 3-43 Ratios of surface to rooftop σ_w,, and surface to upwind σ_w.

Next we examined the ratio of surface wind speed, u_* , and σ_w to the corresponding rooftop values observed in Temple City. As shown in Figure 3-44, wind speed at street level is always smaller than the corresponding rooftop value;

even though both street and rooftop wind speed increase during daytime, the ratio of rooftop wind speed to street wind speed decreases slightly during daytime since street level wind speed does not increases as much as the corresponding rooftop wind speed. Similar to 8th St., the ratios are the lowest during late afternoon, and there is more variation in u_* and σ_w ratios during nighttime. An interesting observation one can make is that the street level σ_w is greater than the roof value during nighttime, while the ratios are almost always smaller than one on 8th St.

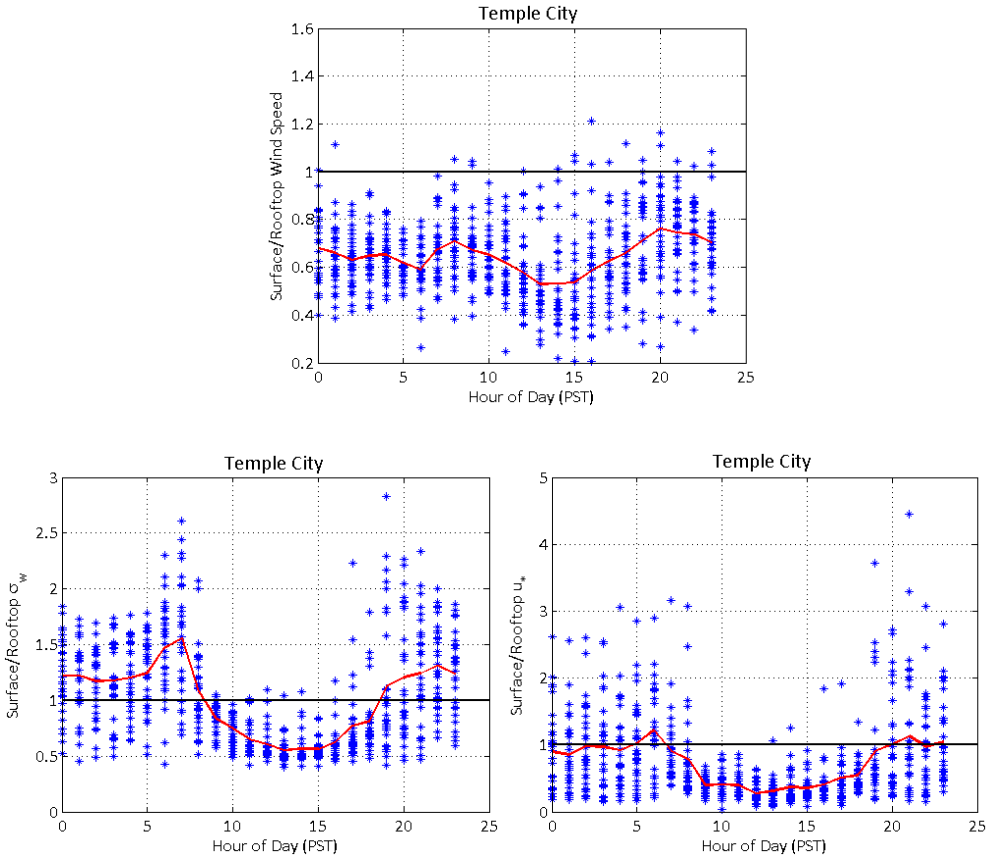

Figure 3-44 Ratio of surface to rooftop wind speed, u_*, and σ_w in Temple City. The red solid line indicates the average value.

3.7.3 Summary of Micrometeorology Measurements

In this section, we summarize the micrometeorological measurements we made in DTLA and Temple City and compare the results to other field studies.

Table 3-6 summarizes the micrometeorological parameters from various studies. It is shown from all the listed studies that wind speeds in the urban areas are always smaller than the upwind rural values. As shown in the table, σ_w *and* u_* are higher in the urban area than the upwind area during nighttime due to the urban heat island effect. Wind speed is always higher in the upwind rural location.

Table 3-7 shows the ratio of wind speed, u_*, and σ_w measured at urban surface level to the corresponding urban rooftop As shown in the table, our measurement on 8th St is consistent with the data collected in the MSG05: the surface level wind speeds are roughly 40% of the rooftop wind speed, and σ_w at the surface is about 60% of the rooftop value. The ratio of surface to rooftop wind speed is much smaller on Göttinger Straße than our DTLA 7th St and 8th measurement. This is possibly because our rooftop measurement is made at 3 meters above the roof, while the Göttinger Straße rooftop measurement was made at 10 meters above the roof.

The ratios given in Table 3-7 can be used to estimate the wind speed and turbulence within the urban canopy from measurements at an upwind rural area. During daytime, wind speed at the urban surface level is about 30~40% of the upwind rural wind speed. The vertical turbulent velocity fluctuation, σ_w, at the urban surface

level can be estimated from the urban surface wind speeds using a turbulent intensity of 0.35. Wind speeds are greatly reduced during nighttime, and urban surface wind speeds can be 60% of the upwind rural wind speeds.

Table 3-6 Summary of the measured micrometeorological parameters at all locations.

**Daytime is defined as between 7am to 7pm*

Dataset	Year	Roof Height (m)	Location	Height (AGL)	Wind Speed (m/s)		u_* (m/s)		σ_u (m/s)		σ_v (m/s)		σ_w (m/s)		Heat Flux (W/m^2)	
					Day	Night	Day	Night	Day	Night	Day	Night	Day	Night	Day	Night
Los Angeles: 8th St	2014	50	Upwind	3	3.64	1.29	0.40	0.14	1.24	0.57	1.18	0.57	0.57	0.18	231.9	-1.5
			Rooftop	52.4	2.56	1.44	0.51	0.27	1.27	0.79	1.26	0.68	0.66	0.34	64.6	13.4
			Parking Lot	4	1.57	0.79	0.25	0.14	1.07	0.55	0.86	047	0.54	0.26	158.7	20.6
			Building I	4	1.12	0.70	0.39	0.26	0.97	0.51	0.68	0.39	0.44	0.29	59.7	19.2
			Building II	4	1.07	0.77	0.18	0.16	0.76	0.57	0.59	0.30	0.43	0.26	69.2	18.2
Los Angeles: 7th St [a]	2013	55	Upwind	3	2.02	--	0.22	--	0.68	--	0.78	--	0.3	--	5.57	--
			Rooftop	57.4	1.67	--	0.51	--	1.03	--	0.93	--	0.57	--	68.0	--
			7th Street	2.4	1.15	--	0.20	--	0.71	--	0.73	--	0.41	--	24.2	--
			Broadway	2.4	1.05	--	0.19	--	0.82	--	0.41	--	0.34	--	67.9	--
Temple City: Las Tunas Dr	2014	6	Upwind[c]	3	2.43	--	0.26	--	0.89	--	0.95	--	0.31	--	133.3	--
			Rooftop	8.4	1.08	0.61	0.24	0.11	0.68	0.32	0.54	0.30	034	0.15	98.3	1.24
			Las Tunas Dr	3	0.60	0.40	0.09	0.07	0.35	0.24	0.25	0.2	0.23	0.16	15.5	4.43
Hannover [b] (Germany)	2003	34	Rooftop	44	3.74	3.19	--	--	--	--	--	--	--	--	--	--
			Göttinger Straße	10	0.77	0.67	--	--	--	--	--	--	0.19	0.14	--	--
New York City	2005	153-223	JFK Airport	3.4	6.2	--	--	--	--	--	--	--	--	--	--	--
			Rooftop	153-223	5.74	--	0.65	--	2.53	--	2.46	--	1.17	--	--	--
			Madison Square Garden	3	2.53	--	0.55	--	1.11	--	1.51	--	0.74	--	--	--
Oklahoma City	2003	--	Surface	8	2.13	2.08	0.45	0.43	1.03	1.06	1.09	0.99	0.7	0.68	--	--

a: Calculation is based on 30min average data collected on Sep. 20th, 2013 from 11am to 6pm

b: Based on 30min average data collected in 2003

c: Daytime is taken between 10am to 6pm

Table 3-7 Ratios of surface to roof and surface to upwind wind speed, u_*, and σ_w.

City	Year	Roof Height (m)	Location	Wind Speed				u_*				σ_w			
				Street/Roof		Street/Upwind		Street/Roof		Street/Upwind		Street/Roof		Street/Upwind	
				Day	Night	Day	Night	Day	Night	Day	Night	Day	Night	Day	Night
Los Angeles-8th St	2014	50	8th St-Parking Lot	0.59	0.55	0.42	0.61	0.48	0.58	0.63	1.16	0.81	0.77	0.94	1.49
			8th St-Building	0.43	0.51	0.31	0.56	0.76	1.00	0.98	2.02	0.67	0.87	0.78	1.67
			8th St-Building II	0.42	0.55	0.30	0.61	0.34	0.63	0.45	1.26	0.66	0.79	0.77	1.52
Los Angeles-7th St [a]	2013	50	7th Street	0.69	--	0.57	--	0.39	--	0.9	--	0.73	--	1.38	--
			Broadway	0.63	--	0.52	--	0.37	--	0.85	--	0.6	--	1.13	--
Temple City	2014	6	Las Tunas Dr	0.55	0.66	0.25	--	0.36	0.66	0.34	--	0.66	1.06	0.75	--
Hannover [b] (Germany)	2003	34	Göttinger Straße	0.20	0.20	--	--	--	--	--	--	0.25	0.23	--	--
New York City	2005	153-223	Madison Square Garden	0.44	--	0.41	--	0.85	--	--	--	0.63	--	--	--

**Daytime is defined as between 7am to 7pm*

a: Calculation is based on 30min average data collected on Sep. 20th, 2013 from 11am to 6pm

b: Based on 1-year of 30min average data

3.8 Magnification of Concentrations in Urban Areas

Sections 3.5, 3.6, and 3.7 show that we can estimate the concentration due to traffic emissions in urban areas using the vertical dispersion model. To quantify the effect of buildings on dispersion we use the magnification factor, defined as the ratio of surface level concentrations due to local traffic emissions in urban areas to the surface concentrations in upwind rural areas with the same emissions.

Concentrations in the upwind open area due to local traffic emissions can be estimated using the following equation.

$$C_{Rural} = \frac{Q}{\gamma \sigma_{w-rural} W} \tag{3-25}$$

where $\sigma_{w-rural}$ is the vertical turbulent velocity fluctuation in the upwind rural area, Q is the emission rate of local traffic, and γ is a constant.

Surface concentrations in an urban area due to local traffic emissions can be calculated using *VDM*,

$$C_{Building} = \frac{Q}{\gamma W \sigma_{w-roof}} \left[1 + \frac{\gamma \sigma_{w-roof}}{\beta \overline{\sigma_w}} \frac{H(1+a_r)}{H + h_o(1+a_r)} \right] \tag{3-26}$$

where σ_{w-roof} is vertical turbulent velocity fluctuation at the rooftop in the urban area and $\overline{\sigma_w}$ is the vertical average of the vertical turbulent velocity fluctuation.

Thus, the magnification factor can be expressed as,

$$M = \frac{C_{Building}}{C_{Rural}} = \frac{\sigma_{w-rural}}{\sigma_{w-roof}} \left[1 + \frac{\gamma \sigma_{w\_roof}}{\beta \overline{\sigma_w}} \frac{H(1+a_r)}{H + h_o(1+a_r)} \right] \tag{3-27}$$

The daily variation of the magnification factor calculated using micrometeorological data collected on 8th St. is plotted in Figure 3-45. As shown, concentrations resulting from local traffic emissions in the urban area could be 10 times higher than those of upwind rural areas. The large magnification is primarily due to the large aspect ratio on 8th St.

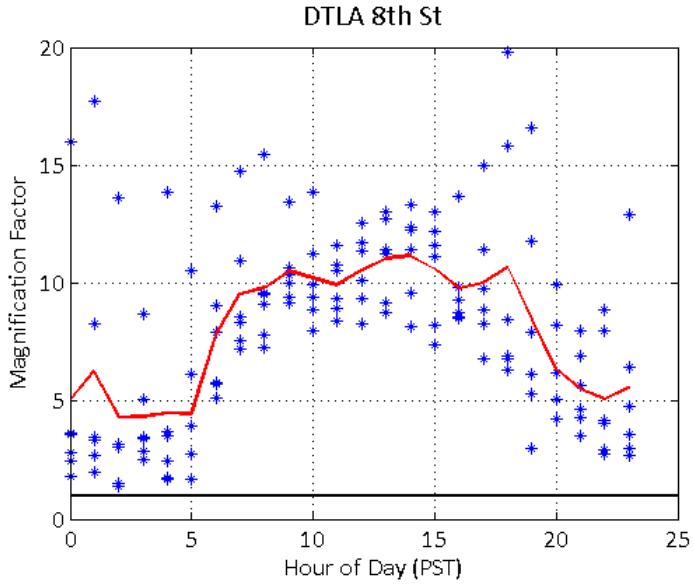

Figure 3-45 Magnification factor: The ratio of urban building region concentration to the upwind rural area concentration.

3.9 Conclusions

We formulated a dispersion model that provides adequate descriptions of concentrations due to local vehicle emissions in streets with non-uniform building heights. The model assumes that vertical transport is the primary mechanism for dispersion. Concentrations are controlled by the street aspect ratio, *H/W*, and the vertical turbulent velocity fluctuations σ_w. The model was evaluated with measurements made on 8th St, and 7th St of downtown LA, and in Temple City. The evaluation shows that the model adequately describes concentrations of traffic emissions in urban areas. We developed a method to isolate the local concentration signals from the total concentrations. We found that buildings in general increase concentrations due to local traffic emissions by up to 2 times when compared to the concentrations measured at an open site in close proximity to the building site. The local contributions also show excellent correlation with the local σ_w.

The measured micrometeorology in Temple City, 7th St, and 8th St. all show that the wind speed is highest in the upwind rural area, and the turbulence is the highest on the rooftop. On all occasions, wind speed is reduced as the flow travels from the open rural area to the urban area. The turbulence level increases from rural area to the urban rooftop, but decreases from urban rooftop to urban street. As a result, the turbulence level in the urban street is slightly smaller than that at the rural area during daytime. Similar to the measurements made by Hanna et al in Manhattan (2005), our measurements suggest that there is high penetration of turbulence into the canyon; the measured surface level σ_w is roughly 60% of the rooftop value. Our measured turbulence intensity at the surface level

ranges from 0.25 to 0.39, which is much higher than the turbulence intensity of 0.1 used in *OSPM*. During nighttime the urban atmosphere does not stabilize, due to the urban heat island effect, resulting in higher turbulence in the urban area than the upwind rural area. The turbulence data we collected suggests that larger aspect ratio (*H/W*) results in a smaller ratio of surface to rooftop turbulence. Clearly, more data is needed to better correlate changes in turbulence and building morphology.

In theory, the *VDM* results can be combined with measurements from urban monitors to generate concentration maps with spatial resolution of meters and time resolution of minutes.

4 CONCLUSIONS

The research project reported in this dissertation is motivated by the need to improve methods to construct concentration maps at the urban/regional scale and street scales for exposure studies. The first part of my research is to construct concentration maps at the urban/regional scale (*grid size ~few kilometers, and domain size ~100km*). We have demonstrated a technique that combines model estimates with observations to produce spatial concentration maps that provide more information than maps generated using interpolated observations.

We formulated a long range transport model that can provide estimates of NOx, NO_2 and O_3 concentrations that compare well with observations at the urban/regional scale. The model achieves the required computational efficiency for exposure studies by separating transport and chemistry using the concept of species age. Sensitivity studies show that our formulation of species age is useful for predicting the chemical processes separately from the transport

In the second part of my research, my focus is on developing models that can be used to estimate concentrations from local vehicle emissions at the street scale (*grid size ~10m, and domain size ~few km*). Existing models such as *OSPM* are primarily designed for street canyons, which might not be applicable to US cities with inhomogeneous building heights. Based on the 5-year concentrations and micrometeorology data collected on Gottinger Street in Hanover, Germany, we formulate the Vertical Diffusion Model (*VDM*) to estimate surface concentrations that are averaged over a city block. The model assumes that vertical diffusion is the primary mechanism governing dispersion in

urban areas. The aspect ratio, defined as the ratio of the equivalent building height to the street width, and the vertical turbulent velocity fluctuations, σ_w, are the controlling parameters for vertical dispersion. To evaluate *VDM*, we have conduct several field measurements of ultrafine particle number concentrations and micrometeorology at various locations with different building morphologies in Los Angeles (LA) County, California. It is shown that *VDM* can adequately describe surface concentrations due to local traffic emissions at streets with non-uniform building heights. Our measurements also indicate that buildings in general increase concentrations due to local traffic.

Since routine measurements of urban surface micrometeorological variables are usually not available, we formulated models that allow us to estimate urban surface turbulence using upwind rural variables. Even though evaluation of the models with our micrometeorological data collected in LA County indicates that the models overestimate urban surface turbulence by about factor of two, the models provide insightful information on how building morphology modifies local micrometeorology. The ratio of surface to roof vertical turbulent velocity, σ_w, is proportional to the 1/3 power of the street aspect ratio. Based on our simultaneous micrometeorology measurements at upwind rural and urban areas, we also formulated empirical models that allow us to calculate urban surface turbulence. Urban surface wind speed is roughly 30~40% of the upwind wind speed, and the urban surface turbulence is roughly 0.35 of the surface wind speed

5 REFERENCES

Azzi, 1992. An Introduction to the generic reaction set photochemical smog mechanism.pdf. Proc. 11th Int. Clean Air Conf. 451–462.

Barlow, J.F., Belcher, S.E., 2002. A Wind Tunnel Model for Quantifyng Fluxes in the Urban Boundary Layer 131–150.

Barnes, M.G., 1980. The use of Kriging for estimating the spatial distribution of radionuclides and other spatial phenomena. Richland, WA.

Beljaars, A.C.M., Schotanus, P., Nieuwstadt, F.T.M., 1983. Surface layer Similarity under Nonuniform Fetch Conditions. J. Clim. Appl. Meteorol. 22, 1800–1810. doi:10.1175/1520-0450(1983)022<1800:SLSUNF>2.0.CO;2

Berkowicz, R., 2000. A Simple Model For Urban Background Pollution. Environ. Monit. Assess. 65, 259–267.

Brandt, J., Christensen, J.H., Frohn, L.M., 2001a. Traffic Scenarios for the City of Aalborg Using the DMU-ATMI THOR Model System. Roskilde, Denmark.

Brandt, J., Christensen, J.H., Frohn, L.M., Berkowicz, R., 2001b. Operational air pollution forecasts from regional scale to urban street scale. Part 2: performance evaluation. Phys. Chem. Earth, Part B Hydrol. Ocean. Atmos. 26, 825–830. doi:10.1016/S1464-1909(01)00092-2

Brandt, J., Christensen, J.H., Frohn, L.M., Berkowicz, R., 2001c. Operational air pollution forecasts from regional scale to urban street scale. Part 1: system description. Phys. Chem. Earth, Part B Hydrol. Ocean. Atmos. 26, 781–786. doi:10.1016/S1464-1909(01)00086-7

Brandt, J., Christensen, J.H., Frohn, L.M., Berkowicz, R., 2003. Air pollution forecasting from regional to urban street scale—implementation and validation for two cities in Denmark. Phys. Chem. Earth, Parts A/B/C 28, 335–344. doi:10.1016/S1474-7065(03)00054-8

Brandt, J., Christensen, J.H., Frohn, L.M., Palmgren, F., Berkowicz, R., Zlatev, Z., 2001d. Operational air pollution forecasts from European to local scale. Atmos. Environ. 35, S91–S98.

Brandt, J., Christensen, J.H., Frohn, L.M., Zlatev, Z., 2001e. Operational Air Pollution Forecast Modelling Using the THOR System. Phys. Chem, Earth 26, 117–122.

Briggs, D.J., Collins, S., Elliott, P., Fischer, P., Kingham, S., Lebret, E., Pryl, K., Van Reeuwijk, H., Smallbone, K., Van Der Veen, A., 1997. Mapping urban air pollution using GIS: a regression-based approach. Int. J. Geogr. Inf. Sci. 11, 699–718. doi:10.1080/136588197242158

Britter, R.E., Hanna, S.R., 2003. Flow and Dispersion in Urban Areas. Annu. Rev. Fluid Mech. 35, 469–496. doi:10.1146/annurev.fluid.35.101101.161147

Byun, D., Schere, K.L., 2006. Review of the Governing Equations, Computational Algorithms, and Other Components of the Models-3 Community Multiscale Air Quality (CMAQ) Modeling System. Appl. Mech. Rev. 59, 51. doi:10.1115/1.2128636

CARB, 2007. 2007 San Joaquin Valley 8-hour Ozone Plan [WWW Document]. URL (http://www.arb.ca.gov/planning/sip/2007sip/sjv8hr/sjvozone.htm)

CARB, 2012. California air quality data for the years 1980-2009. [WWW Document]. URL (http://www.arb.ca.gov/aqd/aqdcd/aqdcddld.htm).

Carreras-Sospedra, M., Vutukuru, S., Brouwer, J., Dabdub, D., 2010. Central power generation versus distributed generation – An air quality assessment in the South Coast Air Basin of California. Atmos. Environ. 44, 3215–3223. doi:10.1016/j.atmosenv.2010.05.017

Carson, D.J., 1973. The development of a dry inversion-capped convectively unstable boundary layer. Q. J. R. Meteorol. Soc. 421, 450–467.

Cimorelli, A.J., Perry, S.G., Venkatram, A., Weil, J.C., Paine, R.J., Wilson, R.B., Lee, R.F., Peters, W.D., Brode, R.W., 2005. AERMOD : A Dispersion Model for Industrial Source Applications . Part I : General Model Formulation and Boundary Layer Characterization. J. Appl. Meteorol. 44, 682–693.

Cohan, a, Chang, W., Carrerassospedra, M., Dabdub, D., 2008. Influence of sea-salt activated chlorine and surface-mediated renoxification on the weekend effect in the South Coast Air Basin of California. Atmos. Environ. 42, 3115–3129. doi:10.1016/j.atmosenv.2007.11.046

Dabdub, D., Carreras-Sospedra, M., Chang, W., Cohan, A., 2008. How new chemistry findings affect our understanding of the weekend effect --- A modeling study.

DePaul, F.T., Sheih, C.M., 1986. Measurements of wind velocities in a street canyon. Atmos. Environ. 20, 455–459. doi:10.1016/0004-6981(86)90085-5

Dockery, D., III, A.P., Xu, X., Spengler, J., Ware, J., Fay, A., Ferris, B., Speizer, F., 1993. An Association Between Air Pollution and Mortality in Six U.S. Cities. N. Engl. J. Med. 329, 1753–1759.

Eder, B., Yu, S., 2006. A performance evaluation of the 2004 release of Models-3 CMAQ. Atmos. Environ. 40, 4811–4824. doi:10.1016/j.atmosenv.2005.08.045

Eeftens, M., Beekhuizen, J., Beelen, R., Wang, M., Vermeulen, R., Brunekreef, B., Huss, A., Hoek, G., 2013. Quantifying urban street configuration for improvements in air pollution models. Atmos. Environ. 72, 1–9. doi:10.1016/j.atmosenv.2013.02.007

Eerens, H.C., Sliggers, C.J., van den Hout, K.D., 1993. The CAR model: The Dutch method to determine city street air quality. Atmos. Environ. Part B. Urban Atmos. 27, 389–399. doi:10.1016/0957-1272(93)90016-Y

Eliassen, A., Saltbones, J., 1983. Modelling of Long-Range Transport of Sulfur Over Europe: A Two-year Model Run and Some Model Experiments. Atmos. Environ. 17, 1457–1473.

Ensberg, J.J., Dabdub, D., 2010. and Physics Impacts of electronically photo-excited NO 2 on air pollution in the South Coast Air Basin of California 1171–1181.

EPA, 2004. Developing Spatially Interpolated Surfaces and Estimating Uncertainty. Research Triangle Park, NC.

Fischer, P.H., Hoek, G., Reeuwijk, H. Van, Briggs, D.J., Lebret, E., Wijnen, J.H. Van, Kingham, S., Elliott, P.E., 2000. Traffic-related differences in outdoor and indoor concentrations of particles and volatile organic compounds in Amsterdam. Atmos. Environ. 34, 3713–3722.

Fujita, E.M., Stockwell, W.R., Campbell, D.E., Keislar, R.E., Lawson, D.R., 2003. Evolution of the Magnitude and Spatial Extent of the Weekend Ozone Effect in California's South Coast Air Basin, 1981–2000. J. Air Waste Manage. Assoc. 53, 802–815. doi:10.1080/10473289.2003.10466225

Hang, J., Li, Y., Buccolieri, R., Sandberg, M., Di Sabatino, S., 2012a. On the contribution of mean flow and turbulence to city breathability: the case of long streets with tall buildings. Sci. Total Environ. 416, 362–73. doi:10.1016/j.scitotenv.2011.12.016

Hang, J., Li, Y., Sandberg, M., Buccolieri, R., Di Sabatino, S., 2012b. The influence of building height variability on pollutant dispersion and pedestrian ventilation in idealized high-rise urban areas. Build. Environ. 56, 346–360. doi:10.1016/j.buildenv.2012.03.023

Hanna, S., White, J., Zhou, Y., 2007. Observed winds, turbulence, and dispersion in built-up downtown areas of Oklahoma City and Manhattan. Boundary-Layer Meteorol. 125, 441–468. doi:10.1007/s10546-007-9197-2

Health Effects Institute, 2013. HEI Perspectives 3: Understanding the Health Effects of Ambient Ultrafine Particles.

Heist, D.K., Brixey, L. a, Richmond-Bryant, J., Bowker, G.E., Perry, S.G., Wiener, R.W., 2009. The effect of a tall tower on flow and dispersion through a model urban neighborhood: part 1. Flow characteristics. J. Environ. Monit. 11, 2163–70. doi:10.1039/b907135k

Hertel, O., Berkowicz, R., 1989. Modeling pollution from traffic in a street canyon. Evaluation of data and model development, DMU Luft.

Hertel, O., Berkowicz, R., 2001. The Operational Street Pollution Model (OSPM), 741–750.

Hoek, G., Beelen, R., de Hoogh, K., Vienneau, D., Gulliver, J., Fischer, P., Briggs, D., 2008. A review of land-use regression models to assess spatial variation of outdoor air pollution. Atmos. Environ. 42, 7561–7578. doi:10.1016/j.atmosenv.2008.05.057

Hurley, P., Manins, P., Lee, S., Boyle, R., Ng, Y.L., Dewundege, P., 2003. Year-long, high-resolution, urban airshed modelling: verification of TAPM predictions of smog and particles in Melbourne, Australia. Atmos. Environ. 37, 1899–1910. doi:10.1016/S1352-2310(03)00047-5

Isakov, V., Johnson, M., Touma, J., 2012. Development and Evaluation of Land-Use Regression Models Using Modeled Air Quality Concentrations. Air Pollut. Model. its Appl. XXI, NATO Science for Peace and Security Series C: Environmental Security 717–722. doi:10.1007/978-94-007-1359-8

Isakov, V., Touma, J.S., Burke, J., Lobdell, D.T., Palma, T., Rosenbaum, A., Ozkaynak, H., 2009. Combining Regional- and Local-Scale Air Quality Models with Exposure Models for Use in Environmental Health Studies. J. Air Waste Manage. Assoc. 59, 461–472. doi:10.3155/1047-3289.59.4.461

Jerrett, M., Arain, A., Kanaroglou, P., Beckerman, B., Potoglou, D., Sahsuvaroglu, T., Morrison, J., Giovis, C., 2005. A review and evaluation of intraurban air pollution exposure models. J. Expo. Anal. Environ. Epidemiol. 15, 185–204. doi:10.1038/sj.jea.7500388

Jin, L., Harley, R. a., Brown, N.J., 2011. Ozone pollution regimes modeled for a summer season in California's San Joaquin Valley: A cluster analysis. Atmos. Environ. 45, 4707–4718. doi:10.1016/j.atmosenv.2011.04.064

Jing, Q., 2011. Air Quality Impact of Distributed Generation of Electricity. University of Caifornia, Riverside.

Johnson, G.M., 1984. A simple model for predicting the ozone concentration of ambient air. Proc. Eighth Int. Clean Air Environ. Conf. Clean Air Soc. Aust. New Zealand, New Zeal.

Johnson, W.B., Ludwig, F.L., Dabberdt, W.F., Allen, R.J., 1973. An Urban Diffusion Simulation Model For Carbon Monoxide. J. Air Pollut. Control Assoc. 23, 490–498. doi:10.1080/00022470.1973.10469794

Kanaroglou, P.S., Jerrett, M., Morrison, J., Beckerman, B., Arain, M.A., Gilbert, N.L., Brook, J.R., 2005. Establishing an air pollution monitoring network for intra-urban population exposure assessment: A location-allocation approach. Atmos. Environ. 39, 2399–2409. doi:10.1016/j.atmosenv.2004.06.049

Kittelson, D.B., Watts, W.F., Johnson, J.P., 2004. Nanoparticle emissions on Minnesota highways. Atmos. Environ. 38, 9–19. doi:10.1016/j.atmosenv.2003.09.037

Klein, P.M., Galvez, J.M., 2014. Flow and turbulence characteristics in a suburban street canyon. Environ. Fluid Mech. doi:10.1007/s10652-014-9352-5

Lebret, E., Briggs, D., van Reeuwijk, H., Fischer, P., Smallbone, K., Harssema, H., Kriz, B., Gorynski, P., Elliott, P., 2000. Small area variations in ambient NO2 concentrations in four European areas. Atmos. Environ. 34, 177–185. doi:10.1016/S1352-2310(99)00292-7

Li, S.-M., 2004. A concerted effort to understand the ambient particulate matter in the Lower Fraser Valley: the Pacific 2001 Air Quality Study. Atmos. Environ. 38, 5719–5731. doi:10.1016/j.atmosenv.2004.04.038

Luhar, A.K., Venkatram, A., Lee, S.-M., 2006. On relationships between urban and rural near-surface meteorology for diffusion applications. Atmos. Environ. 40, 6541–6553. doi:10.1016/j.atmosenv.2006.05.067

Matthias, V., Aulinger, a., Quante, M., 2008. Adapting CMAQ to investigate air pollution in North Sea coastal regions. Environ. Model. Softw. 23, 356–368. doi:10.1016/j.envsoft.2007.04.010

McNair, L.A., Harley, R.A., Russell, A.G., 1996. Spatial Inhomogenenity in Pollutant Concentrations, and Their Implications for Air Quality Model Evaluation. Atmos. Environ. 30, 4291–4301.

Mensink, C., Lewyckyj, N., 2001. Mensink-2001-A simple model for the assessment of air quality in streets.pdf. Int. J. Veh. Des. 27.

Miller, K.A., Siscovick, D., Sheppard, L., Shapherd, K., Sullivan, J.H., Anderson, G.L., Ph, D., Kaufman, J.D., 2007. Long-term Exposure to Air Pollution and Incidence of Cardiovascular Events in Women. N. Engl. J. Med. 356, 447–458.

Monin, A.S., Obukhov, A.M., 1954. Basic laws of turbulent mixing in the surface layer of the atmosphere. Tr. Akad. Nauk SSSR Geophiz. Inst 24, 163–187.

Nakamura, Y., Oke, T.R., 1988. Wind, temperature and stability conditions in an east-west oriented urban canyon. Atmos. Environ. 22, 2691–2700. doi:10.1016/0004-6981(88)90437-4

Neupane, B., Jerrett, M., Burnett, R.T., Marrie, T., Arain, A., Loeb, M., 2010. Long-term exposure to ambient air pollution and risk of hospitalization with community-acquired pneumonia in older adults. Am. J. Respir. Crit. Care Med. 181, 47–53. doi:10.1164/rccm.200901-0160OC

Oke, T.R., 1988. Street design and urban canopy layer climate. Energy Build. 11, 103–113. doi:10.1016/0378-7788(88)90026-6

Panofsky, H.A., Tennekes, H., Lenschow, D.H., Wyngaard, J.C., 1977. The characteristics of turbulent velocity components in the surface layer under convective conditions. Boundary-Layer Meteorol. 11, 355–361. doi:10.1007/BF02186086

Pope, C.A., Burnett, R.T., Thun, M.J., Calle, E.E., Krewski, D., Thurston, G.D., 2002. Lung cancer, cardiopulmonary mortality, and long-term exposure to fine particulate air pollution. J. Am. Med. Assoc. 287, 1132–1141.

Pope, C.A., Dockery, D.W., 2006. Health Effects of Fine Particulate Air Pollution: Lines that Connect. J. Air Waste Manage. Assoc. 56, 709–742. doi:10.1080/10473289.2006.10464485

Pournazeri, S., Tan, S., Schulte, N., Jing, Q., Venkatram, A., 2014. A computationally efficient model for estimating background concentrations of NOx, NO2, and O3. Environ. Model. Softw. 52, 19–37. doi:10.1016/j.envsoft.2013.10.018

Pournazeri, S., Venkatram, A., Princevac, M., Tan, S., Schulte, N., 2012. Estimating the height of the nocturnal urban boundary layer for dispersion applications. Atmos. Environ. 54, 611–623. doi:10.1016/j.atmosenv.2012.02.024

Qian, W., 2010. Investigation of Dispersion and Micrometeorology Under Spatially Inhomogeneous Conditions.

Ross, Z., English, P.B., Scalf, R., Gunier, R., Smorodinsky, S., Wall, S., Jerrett, M., 2006. Nitrogen dioxide prediction in Southern California using land use regression modeling: potential for environmental health analyses. J. Expo. Sci. Environ. Epidemiol. 16, 106–14. doi:10.1038/sj.jea.7500442

Rotach, M., 1995. Profiles of turbulence statistics in and above an urban street canyon. Atmos. Environ. 29, 1473–1486. doi:10.1016/1352-2310(95)00084-C

Samuelsen, S., Dabdub, D., Brouwer, J., Carreras-Sospedra, M., Vutukuru, S., 2010. Air quality impacts of distributed generation in the South Coast air basin and the San Joaquin Valley.

Savelyev, S. a., Taylor, P. a., 2005. Internal Boundary Layers: I. Height Formulae for Neutral and Diabatic Flows. Boundary-Layer Meteorol. 115, 1–25. doi:10.1007/s10546-004-2122-z

Schulte, N., Tan, S., Venkatram, A., 2014. Effective Building Height to Width Ratio of Street Controls Exposure to Vehicle Emissions. Atmos. Environ.

Smith, L., Mukerjee, S., Gonzales, M., Stallings, C., Neas, L., Norris, G., Özkaynak, H., 2006. Use of GIS and ancillary variables to predict volatile organic compound and nitrogen dioxide levels at unmonitored locations. Atmos. Environ. 40, 3773–3787. doi:10.1016/j.atmosenv.2006.02.036

Smyth, S.C., Jiang, W., Yin, D., Roth, H., Giroux, É., 2006. Evaluation of CMAQ O3 and PM2.5 performance using Pacific 2001 measurement data. Atmos. Environ. 40, 2735–2749. doi:10.1016/j.atmosenv.2005.10.068

Stein, A.F., Isakov, V., Godowitch, J., Draxler, R.R., 2007. A hybrid modeling approach to resolve pollutant concentrations in an urban area. Atmos. Environ. 41, 9410–9426. doi:10.1016/j.atmosenv.2007.09.004

Taylor, P., Lawson, D.R., 2014. The Southern California Air Quality Study 37–41. doi:10.1080/10473289.1990.10466671

Ulden, A.P. Van, Holtslag, A.A.M., 1985. Estimation of Atmospheric Boundary Layer Parameters for Diffusion Applications. J. Appl. Meteorol. 24, 1196–1207.

USEPA, 1992. Guidelines for Exposure Assessment.

Venkatram, A., 1980. Estimating the Monin-Obukhov Length in the Stable Boundaty Layer for Dispersion Calculations. Boundary 19, 481–485.

Venkatram, A., 1988. On the use of kriging in the spatial analysis of acid precipitation data. Atmos. Environ. 22, 1963–1975.

Venkatram, A., Cimorelli, A.J., 2007. On the role of nighttime meteorology in modeling dispersion of near surface emissions in urban areas. Atmos. Environ. 41, 692–704. doi:10.1016/j.atmosenv.2006.09.028

Venkatram, A., Du, S., Hariharan, R., Carter, W., Goldstein, R., 1998. The concept of species age in photochemical modeling. Atmos. Environ. 32, 3403–3413. doi:10.1016/S1352-2310(98)00032-6

Venkatram, A., Karamchandani, P., Pai, P., Goldstein, R., 1994. The development and application of a simplified ozone modeling system (SOMS). Atmos. Environ. 28, 3665–3678. doi:10.1016/1352-2310(94)00190-V

Venkatram, A., Kashanian, K., Karamchandani, P.K., Avitzur, T., 1990. Probing the Acid Deposition System with a Semi-empircal Model: The Role of oxidant Limitation. Atmos. Environ. 24.

Vijayaraghavan, K., Karamchandani, P., Seigneur, C., 2006. Plume-in-grid modeling of summer air pollution in Central California. Atmos. Environ. 40, 5097–5109. doi:10.1016/j.atmosenv.2005.12.050

Wilton, D., Szpiro, A., Gould, T., Larson, T., 2010. Improving spatial concentration estimates for nitrogen oxides using a hybrid meteorological dispersion/land use regression model in Los Angeles, CA and Seattle, WA. Sci. Total Environ. 408, 1120–30. doi:10.1016/j.scitotenv.2009.11.033

Yamartino, R.J., Wiegand, G., 1986. Development and evaluation of simple models for the flow, turbulence and pollutant concentration fields within an urban street canyon. Atmos. Environ. 20, 2137–2156. doi:10.1016/0004-6981(86)90307-0

Yuan, C., Ng, E., 2012. Building porosity for better urban ventilation in high-density cities – A computational parametric study. Build. Environ. 50, 176–189. doi:10.1016/j.buildenv.2011.10.023

Zhang, Y., Vijayaraghavan, K., Wen, X.-Y., Snell, H.E., Jacobson, M.Z., 2009. Probing into regional ozone and particulate matter pollution in the United States: 1. A 1 year CMAQ simulation and evaluation using surface and satellite data. J. Geophys. Res. 114, D22304. doi:10.1029/2009JD011898

APPENDIX

A.1 Processing of Sonic Anemometer Data

All CSAT3 raw 10Hz data were processed using a program written in MatLab. The equations used to compute the turbulent fluxes, turbulent velocities, and Monin-Obukhov length are described in this section.

We separate the signal into the time average component and turbulent fluctuations:

$$u = \overline{u} + u' \tag{A-1}$$

$$v = \overline{v} + v' \tag{A-2}$$

$$w = \overline{w} + w' \tag{A-3}$$

$$T = \overline{T} + T' \tag{A-4}$$

where u, v, and w are the along-wind, cross-wind, and vertical velocities, respectively, T is the temperature, ($\overline{\ }$) is the time average, and ( )' is the fluctuation.

Standard Deviation of Vertical Turbulent Velocity Fluctuation:

$$\sigma_w = \overline{w'} \tag{A-5}$$

Standard Deviation of Crosswind Turbulent Velocity Fluctuation:

$$\sigma_v = \overline{v'} \tag{A-6}$$

Standard Deviation of Along-wind Turbulent Velocity Fluctuation:

$$\sigma_u = \overline{u'} \tag{A-7}$$

Surface Friction Velocity:

$$u_* = \left(\overline{u'w'}^2 + \overline{v'w'}^2\right)^{1/4} \tag{A-8}$$

Kinematic Heat Flux:

$$H = \overline{w'T'} \tag{A-9}$$

Monin-Obukhov Length:

$$L = -\frac{T_o u_*^3}{gkH} \tag{A-10}$$

where T_o is the surface temperature, g is the gravitational acceleration, and k is the von Karman constant

A.2 Observed Flow Patterns

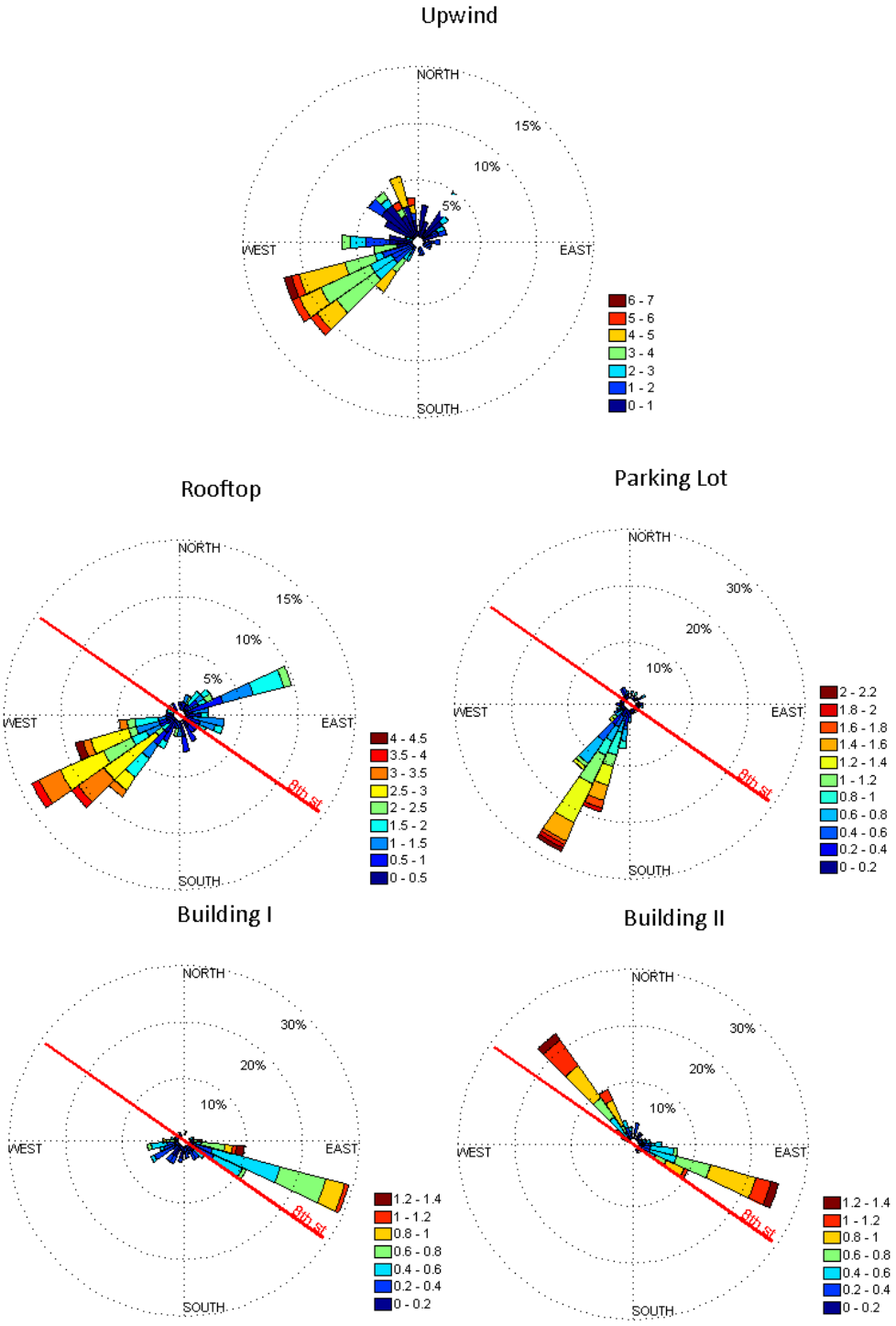

Figure A-1 Wind roses at the 5 locations, the red line indicates the orientation of 8th street.

Figure A-1 shows the wind roses at the 5 locations measured during the 8th St. study. As shown, the rooftop wind directions are the same as the upwind rural wind directions, which are primarily southwesterly. The wind directions measured at the 3 surface locations are quite different despite the fact that all three section are in close proximity. Wind direction measured at the relatively open *Parking Lot* is similar to the rooftop wind direction, which is also southwesterly and perpendicular to 8th street. In the *Building I* and *Building II* regions, winds are almost always parallel to 8th St. If a vortex forms within the street canyon the surface wind direction should be opposite to the roof wind direction. Thus, many of the existing models that are based on vortex flow might not be applicable to 8th St. From this measurement, we can see that buildings have a strong influence on the surface wind direction. In a field measurement conducted by Nakamura and Oke in Kyoto, Japan, it was found that when the roof wind direction is at an angle relative to the street canyon orientation, a spiral-vortex forms in the street canyon (Nakamura and Oke, 1988). The wind direction data collected on 8th St. is consistent with the formation of a helical vortex.

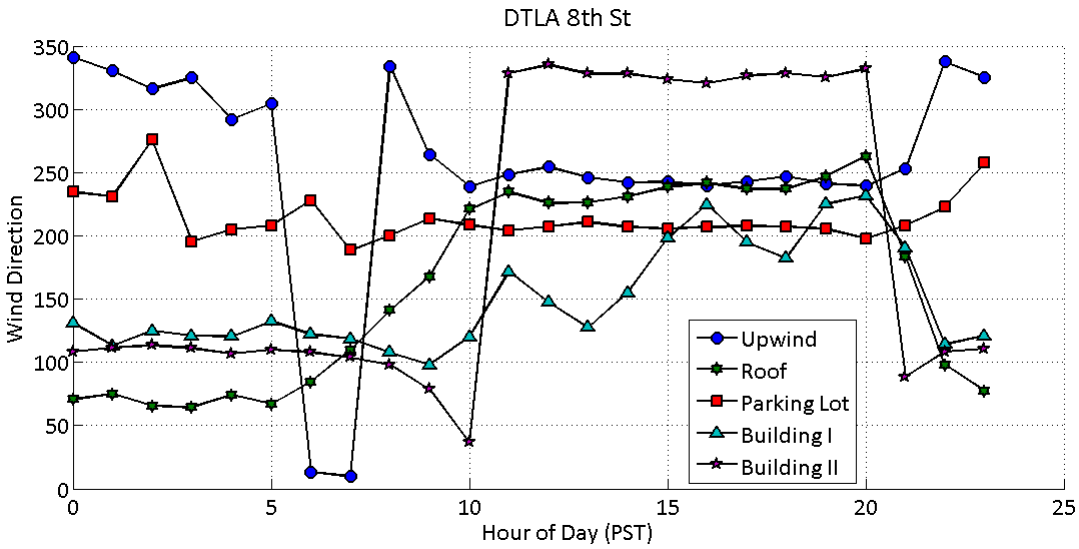

Figure A-2 Diurnal variation of wind directions measured at the 5 locations. Data at each hour are averaged over 6 days. Wind directions are measured in the meteorological convention, i.e. 0^{o} is northerly wind.

The diurnal variation of the measured wind directions at the upwind, rooftop, *Parking Lot*, *Building I*, and *Building II* regions is plotted in Figure A-2. The corresponding 6-day averaged wind speeds are also listed in Table A-1. As shown, surface level wind directions are determined by both the rooftop wind direction and the street orientation. During nighttime, rooftop wind is mainly northeasterly, and the surface wind direction in the *Building II* region is southeasterly, parallel to 8th St. When the rooftop wind changed from easterly to southwesterly around 10 am, wind direction in the *Building II* region changed from southeasterly to northwesterly accordingly, again parallel to 8th St. Interestingly, wind measured at the *Parking Lot* stays southwesterly all day independent of the changes in rooftop wind direction.

Table A-1 Summary of observed wind direction and wind speed during the DTLA-8th St field measurement. Data of each hour are averaged over 6 days. Note: the time stamp is at the end of the averaging period, e.g, hour 1 data is averaged between 12 am and 1 am.

	Upwind		*Rooftop*		*Parking Lot*		*Building I*		*Building II*	
Hour	***WS (m/s)***	***WD (º)***	***WS (m/s)***	***WD (º)***	***WS (m/s)***	***WD (º)***	***WS (m/s)***	***WD (º)***	***WS (m/s)***	***WD (º)***
1	*1.10*	*342*	*0.61*	*72*	*0.33*	*242*	*0.71*	*136*	*0.65*	*106*
2	*1.52*	*329*	*0.92*	*72*	*0.29*	*233*	*0.53*	*114*	*0.71*	*111*
3	*0.75*	*324*	*1.16*	*66*	*0.08*	*291*	*0.81*	*126.*	*0.69*	*113*
4	*0.55*	*329*	*0.83*	*66*	*0.15*	*189*	*0.62*	*120*	*0.63*	*113*
5	*0.49*	*300*	*0.78*	*77*	*0.40*	*191*	*0.82*	*117*	*0.72*	*107*
6	*0.36*	*314*	*0.36*	*72*	*0.29*	*198*	*0.98*	*135*	*0.69*	*107*
7	*1.12*	*14*	*0.90*	*83*	*0.48*	*236*	*0.40*	*123*	*0.69*	*107*
8	*0.97*	*11*	*0.57*	*117*	*0.53*	*203*	*0.29*	*117*	*0.75*	*100*
9	*0.73*	*336*	*0.65*	*137*	*0.77*	*200*	*0.57*	*104*	*0.90*	*94*
10	*1.58*	*262*	*0.66*	*167*	*1.21*	*216.*	*0.75*	*96*	*1.18*	*69*
11	*2.15*	*241*	*1.37*	*225*	*0.94*	*205*	*0.64*	*107*	*0.93*	*40*
12	*3.3*	*248*	*1.84*	*234*	*1.48*	*208*	*0.69*	*158*	*1.28*	*331*
13	*3.18*	*254*	*2.42*	*224*	*1.58*	*212*	*1.08*	*143*	*1.21*	*335*
14	*4.23*	*246*	*3.03*	*224*	*1.83*	*210*	*0.59*	*145*	*0.99*	*330*
15	*4.45*	*241*	*3.13*	*230*	*1.84*	*206*	*0.46*	*143*	*0.73*	*332*
16	*4.42*	*242*	*3.60*	*238*	*1.97*	*205*	*0.51*	*211*	*0.55*	*322*
17	*4.27*	*239*	*3.45*	*241*	*1.78*	*206*	*0.51*	*228*	*0.28*	*320*
18	*3.54*	*242*	*2.95*	*237*	*1.54*	*207*	*0.31*	*177*	*0.28*	*329*
19	*2.30*	*246*	*2.07*	*236*	*1.21*	*207*	*0.54*	*190*	*0.64*	*332*
20	*1.12*	*241*	*1.89*	*245*	*1.01*	*205*	*0.46*	*217*	*0.68*	*329*
21	*0.61*	*239*	*1.01*	*259*	*0.55*	*195*	*0.71*	*227*	*0.65*	*336*
22	*0.72*	*247*	*0.21*	*206*	*0.34*	*206*	*0.53*	*194*	*0.71*	*58*
23	*0.50*	*337*	*0.58*	*98*	*0.37*	*230*	*0.81*	*116*	*0.69*	*103*
24	*0.86*	*324*	*0.79*	*81*	*0.46*	*256*	*0.62*	*119*	*0.63*	*111*

Wind roses of measured wind speed at the four locations for the 7th St. measurements (*Upwind. Rooftop, Broadway, and 7th St*) are shown in Figure A-3. Rooftop wind is mainly southerly, which is slightly different than the upwind wind direction. Wind is mainly parallel to Broadway. It is clear that there is vortex formation in 7th St, which is not seen in 8th St. This is likely due to the presence of the short parking structure at the

intersection of 7th and Broadway, which results in a step-up canyon structure.

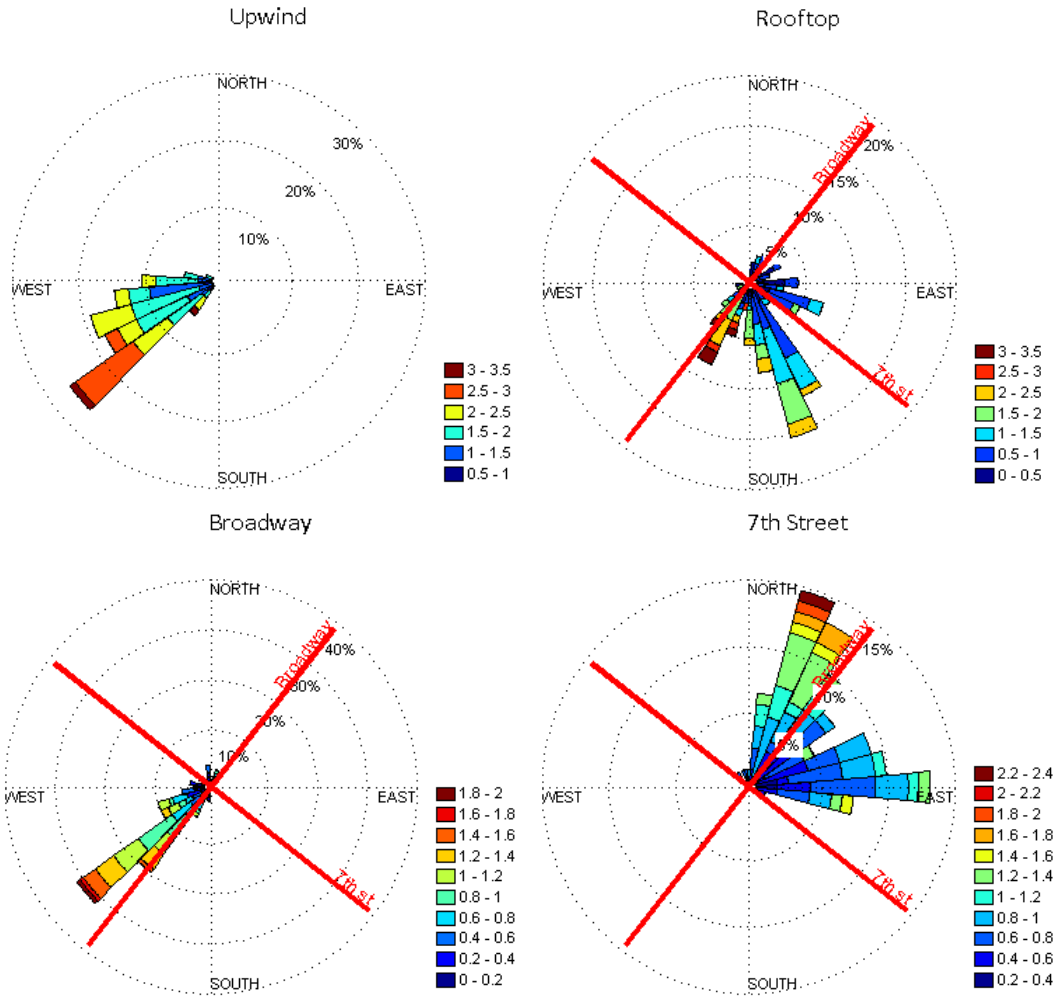

Figure A-3 Wind roses at upwind, rooftop, Broadway, and 7th St.

Wind roses of measured upwind, rooftop, and street level winds in Temple City are shown in Figure A-4. As shown, wind at the rooftop is mostly northerly (nighttime) and southwesterly (daytime), but street level wind speed is mostly northwesterly despite that the street level wind speed is measured only 6 m below the rooftop measurements.

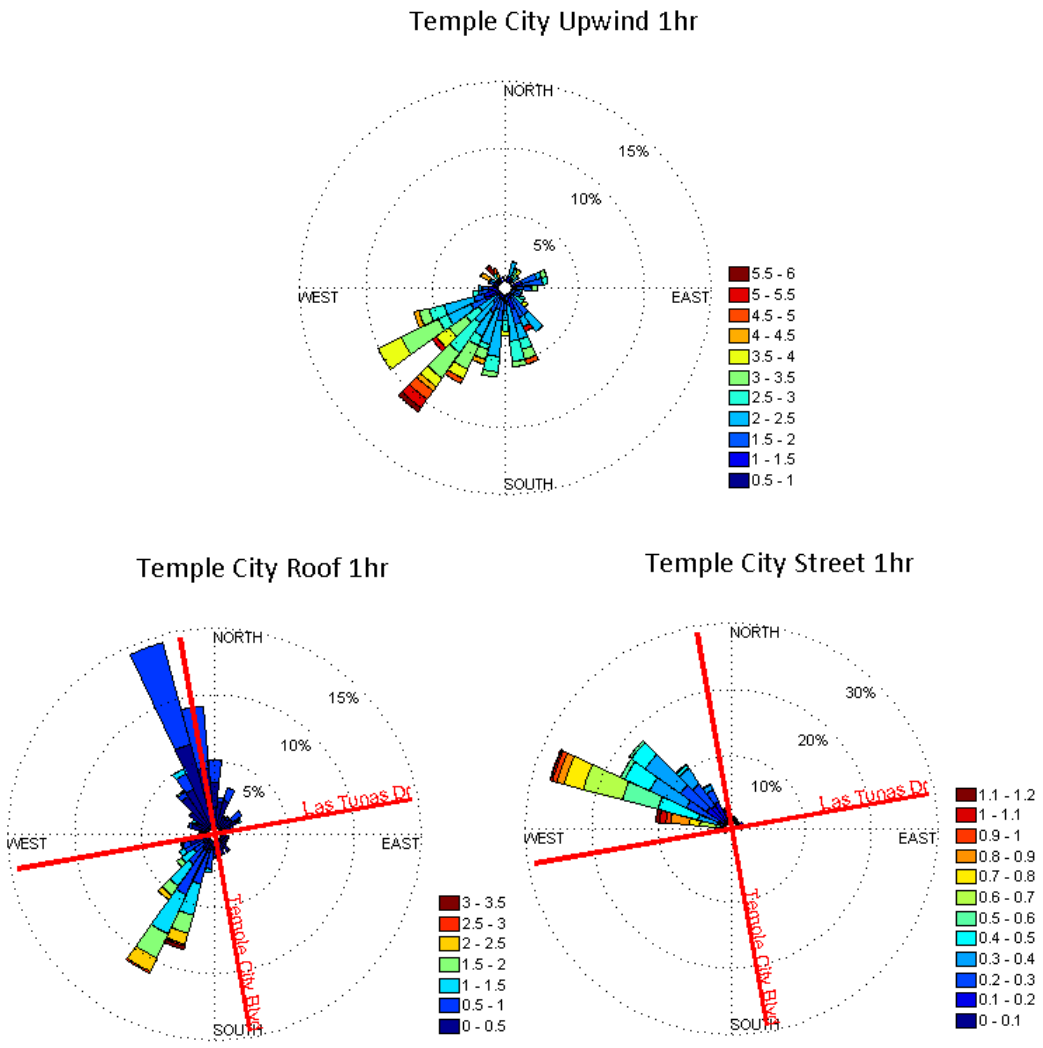

Figure A-4 Wind Roses at upwind, rooftop, and on Las Tunas Dr. Note: upwind only includes daytime measurements.

The diurnal variation of wind directions is shown in Figure A-5; rooftop wind is northerly during nighttime, and it changes to southeasterly around 10 am, and then stays southerly during the rest of the day until sunset, and then back to northerly during nighttime. Wind direction at the upwind rural area is the same as the rooftop during daytime. Interestingly, the street wind stays as northwesterly the entire day, possibly due to the presences of buildings. Thus, an important effect of buildings is modulating the

wind direction at street level. Also, as can be seen from the wind roses, the wind speed measured at the surface level is much smaller than the rooftop wind speed even though the rooftop measurement is made only 6 m above the surface measurement. This is probably because the surface sonic anemometer was placed too close to the building, and thus measured much smaller wind speeds and turbulence.

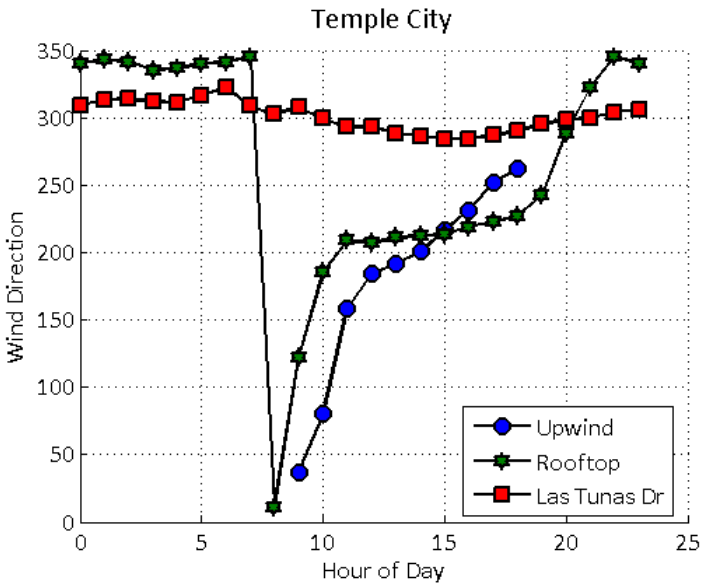

Figure A-5 Diurnal variation of wind directions: hourly wind direction, averaged over the entire measurement period, versus hour of day.

A.3 Estimating Surface Roughness Length, z_o

We estimate the surface roughness length using the logarithmic wind profile under neutral conditions, which is described as follows,

$$u(H) = \frac{u_*}{k} ln\left(\frac{H-d}{z_o}\right) \quad \textbf{(A-11)}$$

where u is the wind speed, u_* is the friction velocity, H is the measurement height, d is the displacement height, and k is the von Karman constant.

Assuming $d = 5z_o$ and neutral stability, we get,

$$z_o = \frac{H}{exp\left(\frac{u}{u_*}k\right) + 5} \quad \textbf{(A-12)}$$

The estimated z_o at all measurement locations are listed in Table A-2

Table A-2 Estimated roughness length, z_o, at all the measurement locations

Dataset	*Year*	*Measurement Height (m)*	*Location*	*Measured Roughness Length, zo (m)*
Los Angeles: 8th St	***2014***	*3*	*Upwind(LAX)*	*0.08*
		52.4	*Rooftop*	*6.62*
		4	*Parking Lot*	*0.33*
		4	*Building I*	*0.58*
		4	*Building II*	*0.29*
Los Angeles: 7th St [a]	***2013***	*3*	*Upwind*	*0.05*
		57.4	*Rooftop*	*6.5*
		2.4	*7th Street*	*0.17*
		2.4	*Broadway*	*0.16*
Temple City: Las Tunas Dr	***2014***	*3*	*Upwind*	*0.06*
		8.4	*Rooftop*	*0.65*
		2.4	*Las Tunas Dr*	*0.18*